

The Extrinsic Spin Hall Effect

Dissertation

zur Erlangung des akademischen Grades
doctor rerum naturalium (Dr. rer. nat.)

vorgelegt von

Martin Gradhand

geboren am 14.04.1982 in Halle

Institut für Physik
der Naturwissenschaftlichen Fakultät II
der Martin-Luther-Universität Halle-Wittenberg



Halle, den 25. Juni 2010

Gutachter

1. Gutachter: Prof. I. Mertig
2. Gutachter: PD. Dr. A. Ernst
3. Gutachter: Prof. T. Kimura

Tag der Verteidigung: 26.10.2010

Contents

1	Introduction	5
1.1	Motivation	5
1.2	Experimental observation of the spin Hall effect	8
1.3	Origin of the spin Hall effect	12
2	Theoretical background	19
2.1	Electronic structure	20
2.1.1	Density functional theory	20
2.1.2	Dirac equation	22
2.1.3	Green function method	22
2.1.4	Relativistic KKR method	24
2.1.5	Impurity problem within the KKR method	28
2.2	Band structure and Fermi surface	30
2.2.1	Evaluation of the eigenvalues and eigenfunctions	30
2.2.2	Evaluation of the Fermi surface	32
2.2.3	Evaluation of the Fermi velocity	33
2.2.4	Expectation value of the spin operator	35
2.3	Spin relaxation	37
2.4	Electronic transport	39
2.4.1	Linearized Boltzmann equation	39
2.4.2	Charge conductivity and spin transport	40
3	Results	43
3.1	First-principles calculations of spin relaxation times of conduction electrons in Cu with nonmagnetic impurities	51
3.2	Spin polarization on the Fermi surfaces of metals by the KKR method	59
3.3	Fully relativistic <i>ab initio</i> treatment of spin-flip scattering caused by impurities	69
3.4	Extrinsic Spin Hall Effect from First Principles	75
3.5	Spin Hall angle versus spin diffusion length: Tailored by impurities	81
4	Summary	89
Appendices		
A	Dependence of ρ_{yx} on ρ_{xx} in the dilute limit	91

B	Numerical parameters within the KKR method	93
B.1	Periodic host system	93
B.2	Self-consistent impurity problem	94
B.3	Transport calculation	95
C	Fermi velocity for different metals	97
D	Influence of vertex corrections (scattering-in term) on the spin Hall effect	99
E	Spin diffusion length in a free-electron like model	101
F	Relativistic symmetry of a cubic lattice	103
	Bibliography	104
	Publications	111
	Acknowledgment	113
	Eidesstattliche Erklärung	115
	Curriculum vitae	117

Chapter 1

Introduction

1.1 Motivation

The first basic considerations of the extrinsic spin Hall effect were published by Mott and Massey [1] and Landau and Lifshitz [2] in 1965. Some years later, Dyakonov and Perel [3] continued the theoretical discussion of the extrinsic mechanism. After many years without any significant progress, Hirsch [4] proposed an experimental setup in 1999. Starting from this year, the spin Hall effect attracted a lot of attention because of its possible application in the spintronic field of research [E7, 5–13]. In spintronics the spin degree of freedom of an electron is used in addition to its charge [14–16]. Usually, spin polarized currents injected from a ferromagnet are necessary to address the spin degree of freedom. However, this procedure is quite inefficient, especially, for semiconductors [14, 17, 18]. The hope is that the spin Hall effect opens the opportunity to create reasonable spin currents without the problem of spin injection.

In a simple picture the spin Hall effect (SHE) describes the transversal spin current induced by a longitudinal charge current in a non-magnetic material as sketched in Fig. 1.1. The driving mechanism is the spin-orbit coupling. At first glance, it seems

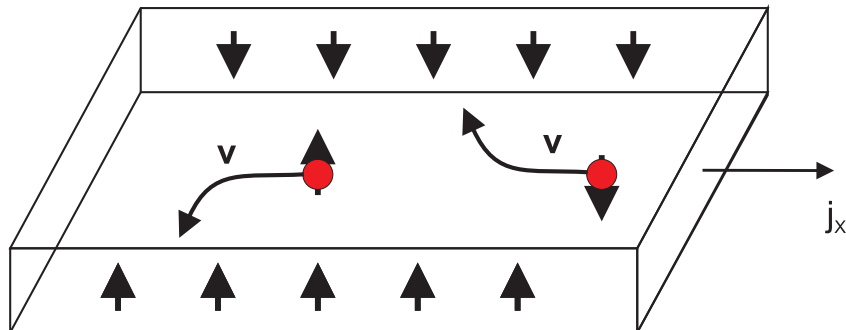


Figure 1.1: Principle of the spin Hall effect: Perpendicular to the applied charge current (j_x) spin accumulation accompanied by a spin current, is induced.

easy but it already implies several crucial problems. First of all, a definition of a spin current in comparison to a charge current is needed. Furthermore, a possible way of measuring spin currents has to be established.

The usual and intuitive way of defining a spin current comes from the "two current model" of a non-relativistic discussion. The main assumption is a parallel circuit of two independent spin channels contributing to the total current. The total charge current density \mathbf{j}_e is the sum of both,

$$\mathbf{j}_e = \mathbf{j}_\uparrow + \mathbf{j}_\downarrow, \quad (1.1)$$

whereas, the spin current, namely the amount of transported spin, is given by the difference

$$\mathbf{j}_s = \mathbf{j}_\uparrow - \mathbf{j}_\downarrow. \quad (1.2)$$

The conductivity tensor $\sigma_{\uparrow(\downarrow)}$ is defined for both spin channels by

$$\mathbf{j}_{\uparrow(\downarrow)} = \underline{\sigma}_{\uparrow(\downarrow)} \mathbf{E}, \quad (1.3)$$

respectively. For a system with at least tetragonal symmetry the conductivity tensor has the form

$$\sigma_\uparrow = \begin{pmatrix} a & b & 0 \\ -b & a & 0 \\ 0 & 0 & c \end{pmatrix}, \quad \sigma_\downarrow = \begin{pmatrix} a & -b & 0 \\ b & a & 0 \\ 0 & 0 & c \end{pmatrix}. \quad (1.4)$$

Such a system with spin Hall effect would have zero charge Hall current

$$\sigma_e = \sigma_\uparrow + \sigma_\downarrow = \begin{pmatrix} 2a & 0 & 0 \\ 0 & 2a & 0 \\ 0 & 0 & 2c \end{pmatrix} \quad (1.5)$$

and a non zero spin Hall current

$$\sigma_s = \sigma_\uparrow - \sigma_\downarrow = \begin{pmatrix} 0 & 2b & 0 \\ -2b & 0 & 0 \\ 0 & 0 & 0 \end{pmatrix}. \quad (1.6)$$

The spin Hall effect in this language is a non vanishing off-diagonal term in the conductivity tensor. The usual way to quantify the spin Hall effect is to calculate the ratio

$$\alpha = \frac{\sigma_s^{yx}}{\sigma_e^{xx}} \quad (1.7)$$

which is the so called *spin Hall angle*. Two problems remain with such a definition. Firstly, we have not specified how the spin current can be measured. Secondly, the spin is not conserved and not a good quantum number. It follows from the fact that the spin operator does not commute with the operator of the spin-orbit coupling which is the driving force of the effect. In fact, the idea of two currents flowing independently through a sample is then questionable.

Already from the previous point of view a deeper understanding of the spin Hall effect is necessary and several physical questions have to be solved. The spin-orbit interaction, which is a purely relativistic effect has to be treated correctly. The spin relaxation processes need to be considered, and possible measurements of a spin current have to be understood.

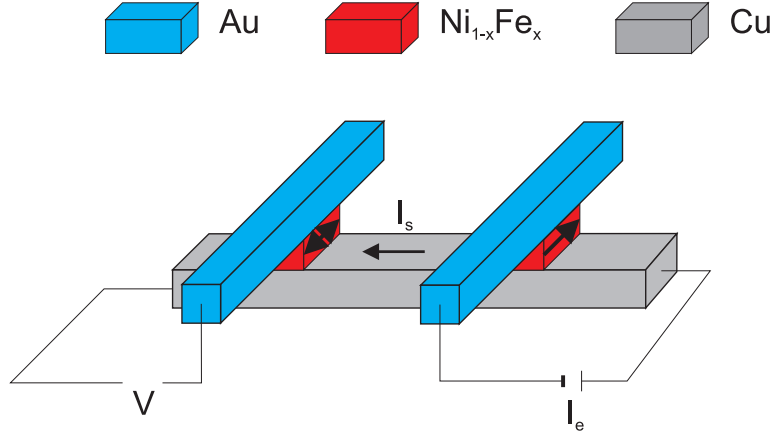


Figure 1.2: The experimental setup of Yang et al. [19] to switch the magnetization of a small ferromagnet via a pure spin current. Substituting the spin current injected from another ferromagnet by a spin Hall device would lead to a magnetization switching device without a reference ferromagnet.

In addition, the spin Hall effect has a high potential for applications as already mentioned. As an example I shortly introduce the experiment of Yang et al. [19] (see Fig. 1.2). In this experiment it was possible to switch the magnetization of a small ferromagnet by a pure spin current. So far they used for the injection of the spin current another ferromagnet. If one would replace this ferromagnet by a spin Hall device the small magnet could be switched without any other magnet in the system. This experiment implies two requirements for a spin Hall device in future applications. The spin Hall angle should be large in order to minimize the charge current through the nonmagnet. The largest angle reported so far is about 0.1 in a Au sample [11]. A new proposal should be at least of comparable order of magnitude. On the other hand, the induced spin current must survive in the nonmagnet until it reaches the ferromagnet. The quantity characterizing the relaxation of the spin current is the spin diffusion length l_{sf} . It has to be large in comparison to the size of the device. Typical spin Hall devices are prepared by electron beam lithography where the spatial resolution is limited to about 20 nm. The spin diffusion length must be at least longer than this. For maximizing the spin current it should be as large as possible. Both quantities are determined by the spin-orbit interaction. The spin Hall effect needs a strong spin-orbit coupling to induce a large spin Hall current, whereas, the spin diffusion length is infinite for vanishing spin-orbit coupling. Maximizing both, the spin Hall angle and the spin diffusion length, is a difficult task and material dependent calculations are needed. To quantify the conditions for both quantities, future spin Hall devices require

$$\begin{aligned} \alpha &\geq 0.1 \\ \text{and} & \\ l_{sf} &\geq 20 \text{ nm} . \end{aligned} \tag{1.8}$$

The aim of this thesis is to identify systems which exhibit a large spin Hall angle in combination with a long spin diffusion length. For this purpose both, the spin Hall effect and the spin relaxation process will be described by *ab initio* methods. Furthermore, this work should contribute generally to a deeper understanding of the spin Hall effect, its microscopic mechanisms, and the way how the spin-orbit interaction induces the effect.

1.2 Experimental observation of the spin Hall effect

During the last years several experimental results were published on the spin Hall effect. The first were optical measurements using Kerr rotation [5, 20]. They image the spin accumulation at the lateral sites of a semiconductor induced by an applied longitudinal charge current. Subsequently, several groups were able to measure the spin Hall effect in all-metallic devices electronically [8, 9, 11, 21–23]. For two reasons I will restrict the further discussion of experiments to all-metal electronic devices. First of all, the existing electronic measurements are much easier transferable to applications than the optical measurements for semiconductors presented so far. Second, the theoretical discussion in this work is based on metallic materials.

To understand the experimental observation of the spin Hall effect two main concepts are necessary. Those are the spin accumulation at ferromagnet/nonmagnet interfaces [18, 24] and the non-local measurements of spin transport [25–29]. In Fig. 1.3 the spin accumulation model of Fert and Jaffr es is sketched schematically. They derived it using separate diffusion equations for the spin channels including spin relaxation processes. In Fig. 1.3 the chemical potential for both spin channels is sketched at the ferromagnet/nonmagnet interface. Due to the imbalance of spins in the ferromagnet the majority spins accumulate at the interface, whereas, the minority spins are pushed away from it. Caused by spin relaxation the chemical potentials in the non-magnetic electrode are equalized after a characteristic length, the spin diffusion length l_{sf} . The key point is that the chemical potential for the two spin channels separately are continuous functions at the interface but the averaged chemical potential has a jump. The measured quantity in an experiment is the voltage drop, i.e. the jump in the averaged chemical potential.

The second concept, depicted in Fig. 1.4, is the non-local measurement. The basic

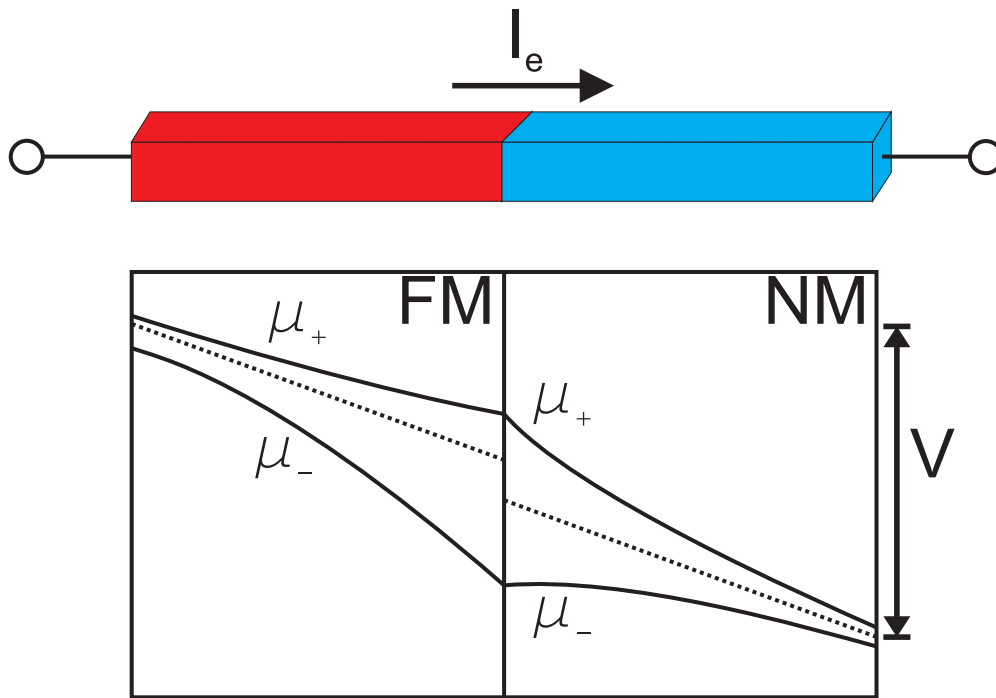


Figure 1.3: The concept of spin accumulation according to Fert and Jaffr es [18] with the dashed line as asymptotes for the case of vanishing spin diffusion length.

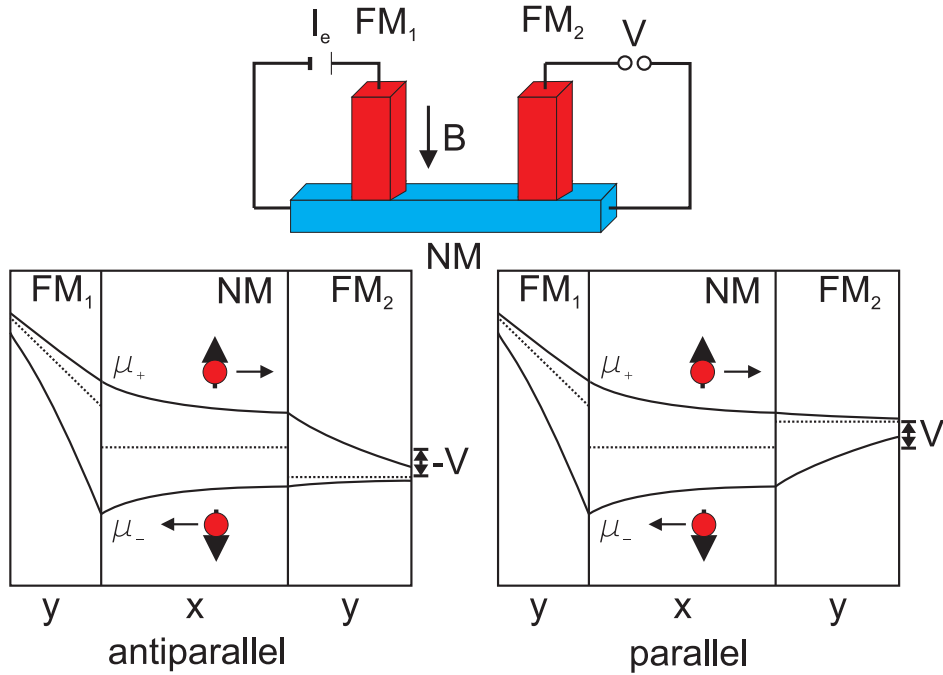


Figure 1.4: The principle of a non-local measurement [29]. The measured quantity is the non-local resistance $R_s = \frac{V}{I_e}$ given by the asymptotes (dashed lines).

idea is that the measurement of a charge current, or the injection of a charge current, is locally separated from the measurement of the voltage drop. The hope is that such a technique allows for a pure measurement of the effect of spin accumulation without any other spurious effects. For an understanding of such an experiment the spin accumulation at interfaces is essential. The current is driven from the first ferromagnet (see Fig. 1.4 FM_1) to the left arm of the nonmagnet (the blue electrode in Fig. 1.4). Due to the concept of spin accumulation the majority electrons accumulate at the interface and the concentration of minority electrons reduces. This leads to a spin current to the right in the non-magnetic electrode. Majority electrons diffuse to the right and minority electrons diffuse to the left, but no net charge is flowing. The second ferromagnet is used as a probe to measure the "up" or "down" electrons, respectively. If the magnetization of the ferromagnetic electrodes is antiparallel the measured voltage drop between the second ferromagnet and the right arm of the nonmagnet has the opposite sign in comparison to the parallel configuration. A typical measurement of that type is presented in Fig. 1.5 [30]. Due to different coercive fields the two ferromagnets switch at different applied magnetic fields and two states, parallel and antiparallel, can be measured. The full and broken lines are a hysteresis cycle going from positive to negative magnetic fields or vice versa. From such an experiment the spin diffusion length can be easily extracted by varying the distance between the two ferromagnets. The experimental diffusion length that we compare our results to is usually taken from such type of experiment.

The extension from a lateral spin valve (non-local measurement) to a spin Hall experiment is just replacing the second ferromagnet by a non-magnetic material. Figure 1.6 shows the scheme for the measurement of the inverse (a) and the direct (b) spin Hall effect. For an explanation it is easier to start with the inverse effect since it is quite similar to the spin accumulation measurements. In this case the charge current

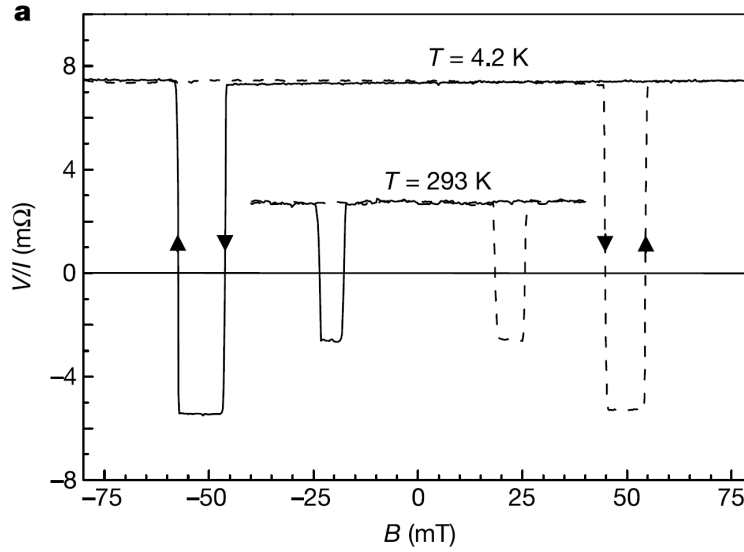


Figure 1.5: The non-local spin accumulation signal for a lateral spin valve (taken from Jedema et al. [30]).

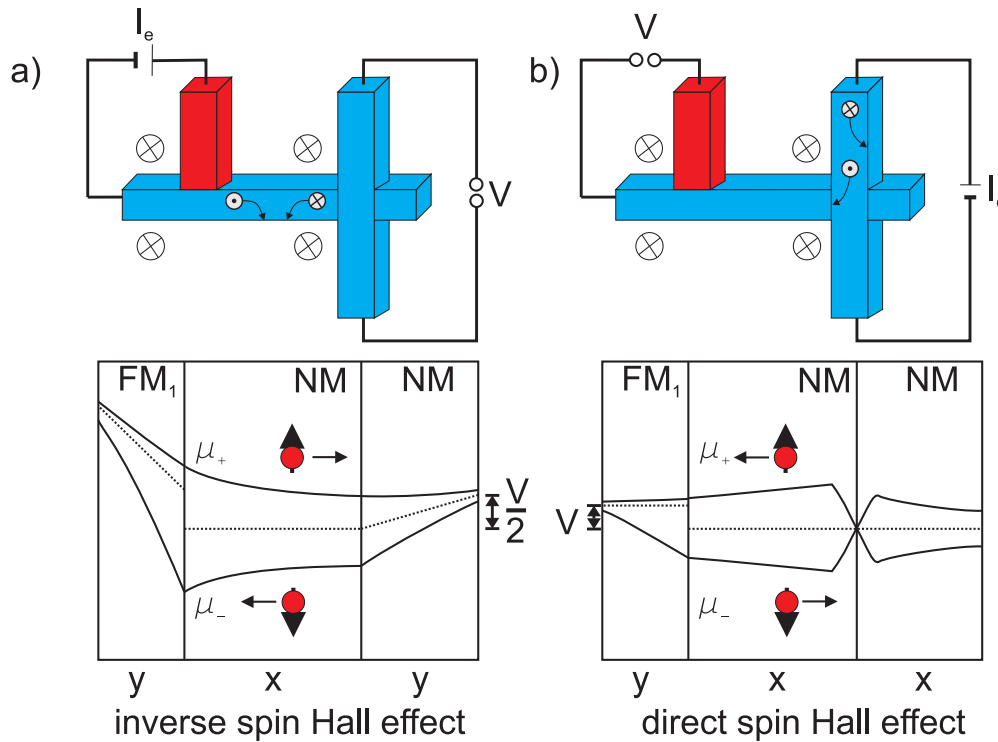


Figure 1.6: The measurement of the inverse and the direct spin Hall effect.

is driven from the ferromagnet to the left arm of the non-magnetic material. The spin accumulation induces a pure spin current flowing to the right side. Due to the spin-orbit interaction and the asymmetric scattering the "up" and "down" spins are scattered to the same side since their drift velocity, induced by the spin accumulation, points in opposite direction. If all electrons are mainly scattered to one side a voltage drop can be measured in the non-magnetic Hall cross. Here, a pure spin current is transformed into a charge current, voltage drop, which is the inverse spin Hall effect. For the direct effect (1.6 a) the charge current is driven through the transverse arms

Table 1.1: Experimental results are given for the longitudinal conductivity σ_{xx} , the spin Hall conductivity σ_{yx} , the Hall angle α , and the spin diffusion length l_{sf} .

material	σ_{xx} $(\mu\Omega cm)^{-1}$	$ \sigma_{yx}^s $ $10^{-3}(\mu\Omega cm)^{-1}$	$ \alpha $	l_{sf} nm	reference
Al	0.1	0.034	0.00034	500	[8, 31] (4.2 K)
Au	0.48	<11.0	<0.023		[22] (4.5 K)
	0.25	0.4	0.0016		[23]
Pt	0.37	42.0	0.113	86	[11] (295 K)
	0.024	0.16	0.0067		[23]
	0.064	0.24	0.0037	7	[9] (295 K)
	0.055	0.33	0.006	14	[21] (295 K)

of the non-magnetic Hall cross. The spin Hall effect induces a spin current into the horizontal arms and the ferromagnet is used to measure the chemical potential of the "up" or "down" electrons, respectively.

A typical measured signal for both, the inverse and the direct spin Hall effect, is shown in Fig. 1.7. The ΔV is the non-local voltage drop symmetrized around zero. The spin Hall signal is the change of the non-local resistance $\Delta R = \Delta V(+B)/I(+B) - \Delta V(-B)/I(-B)$. In Table 1.1 some experimental results for the spin Hall and the non-local spin diffusion measurements are summarized.

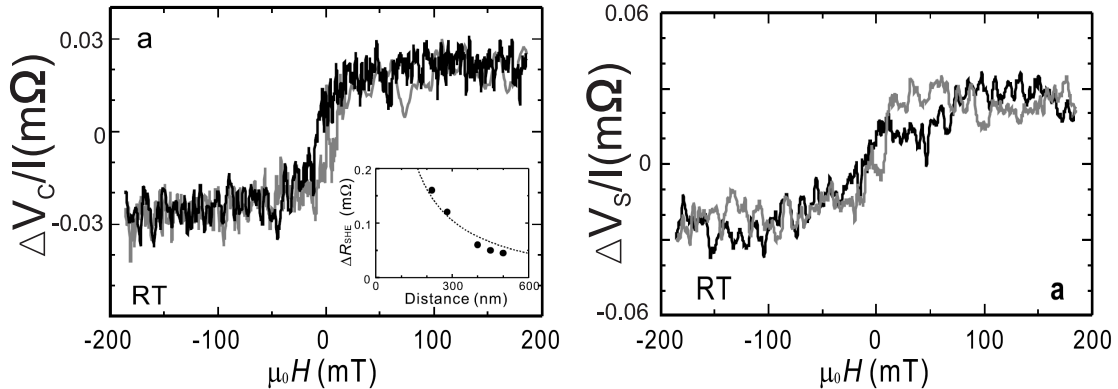


Figure 1.7: The measured signal of a) the inverse and b) the direct spin Hall effect according to Kimura et al. [9].

Two important facts can be deduced from this table. Firstly, the Hall angle can change over orders of magnitude even for a simple metal such as gold. This implies that extrinsic effects like scattering from impurities must be important. Secondly, the spin diffusion length changes over orders of magnitude for different materials. It is very small for Pt and as long as 500 nm for Al which would be ideal for an application. However, the problem is that in Al the observed Hall angle is quite small. From the table Au seems to be a candidate for an application since it combines a large Hall angle with a reasonable spin diffusion length of about 100 nm.

The aim of this thesis is to identify systems which provide the requested properties and to understand the underlying mechanisms for possible tuning.

1.3 Origin of the spin Hall effect

So far I never discussed the origin and mechanisms which lead to the spin Hall effect. The only statement was that the spin-orbit interaction is necessary. This section gives an inside into the various mechanisms and possibilities to create a spin Hall current. This elementary knowledge is crucial for finding a way to be able to tune the spin Hall angle and the spin diffusion length in a device.

First, the analogy of the spin Hall and the anomalous Hall effect (AHE) will be discussed briefly. It shows that the explanations which hold for the AHE are also valid for the SHE. In the next part, the separation into intrinsic and extrinsic contributions is introduced. Those two main contributions are discussed in the third and fourth part in more detail. Various contributing mechanisms and their possible description are explained.

The spin and the anomalous Hall effect

The only statement I gave so far about the mechanism responsible for the SHE is that a spin-dependent asymmetric scattering of the flowing electrons leads to a spin accumulation at the transversal edges of our sample (see Fig. 1.1). Due to the same number of up and down electrons in a non-magnetic sample no voltage drop is measurable. Imagine the same principle in a magnetic material. It necessarily leads to a transversal voltage drop because of the net magnetization. Both cases are depicted in Fig. 1.8. Although the microscopic origin of both effects is the same, namely the

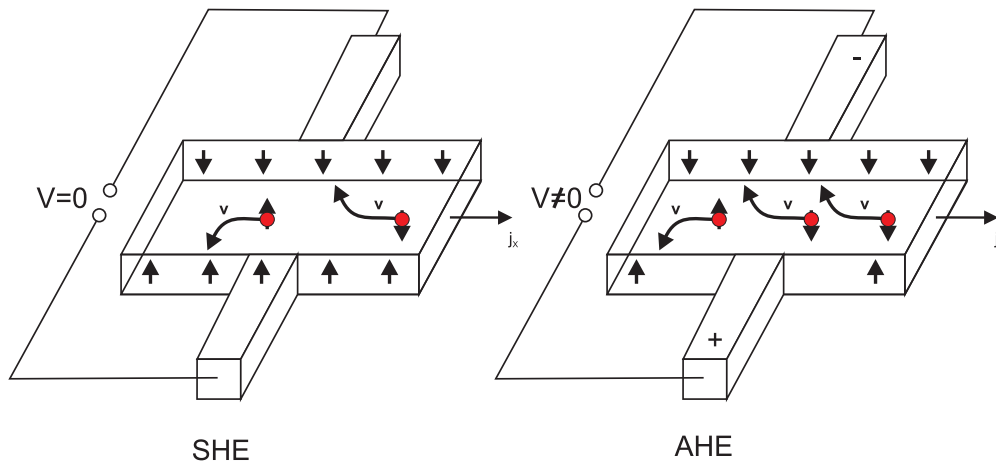


Figure 1.8: The spin (left) and the anomalous Hall effect.

asymmetric spin-dependent scattering, the experimental result is quite different. In one case, a transversal voltage is measurable (AHE), but this is not the case for the SHE. In conclusion, all explanations and descriptions of the mechanism found for the AHE should hold for the SHE as well, except the measuring principle.

The intrinsic and extrinsic mechanism

After the experimental finding of the anomalous Hall effect by E. H. Hall in 1880 no microscopic understanding of this effect was found for decades. It took about 70 years until Karplus and Luttinger [32] and Smit [33, 34] developed the first proper

microscopic explanations for this effect. They used different approaches and found different mechanisms.

Assume that we have an ideal crystal without any impurities. The explanation of the AHE as the result of asymmetric scattering is in this case undefined since the ideal Bloch states would never be scattered. Nevertheless, it was shown [32, 35–38] that even without perturbations of the ideal crystal an anomalous Hall current can be found. This effect is called the *intrinsic* contribution and it is usually explained in terms of an anomalous velocity in addition to the normal velocity $v = \partial E / \partial k$. The other contributions induced by a perturbing potential are called *extrinsic* [33, 34, 39–42]. The distinction sounds naturally but it causes problems, as we will see in the next sections. The different authors used different approaches to derive the effects. Namely, the description via a semiclassical Boltzmann like theory [32–40, 42] and the calculation based on the quantum mechanical Kubo-Streda formula [41, 43, 44]. The connection of both descriptions was shown by Sinitsyn et al. [43] for a 2-dimensional model Hamiltonian.

In the next two sections I will mainly follow the semiclassical Boltzmann approach. On the one hand, this description gives the most understandable microscopic inside into the mechanisms, and, on the other hand, I employ the semiclassical Boltzmann approach in my work to describe the SHE.

The current

$$\mathbf{J} = -e \sum_{\mathbf{k}} \mathbf{v}_{\mathbf{k}} f_{\mathbf{k}} \quad (e > 0) \quad (1.9)$$

is expressed in terms of the effective one-electron distribution function $f_{\mathbf{k}}$ under the action of an applied electric field \mathbf{E} and the velocity $\mathbf{v}_{\mathbf{k}}$ is given for the crystal momentum \mathbf{k} . For the sake of simplicity, I omit the band index n . The distribution function is usually separated into two parts

$$f_{\mathbf{k}} = f_{\mathbf{k}}^{eq} + g_{\mathbf{k}} , \quad (1.10)$$

where $f_{\mathbf{k}}^{eq}$ is the equilibrium distribution function and $g_{\mathbf{k}}$ is the response on the applied electric field. The distribution function is a solution of the Boltzmann equation for a homogeneous system [35, 44, 45]

$$\dot{\mathbf{k}} \frac{\partial f_{\mathbf{k}}^{eq}}{\partial \mathbf{k}} = \sum_{\mathbf{k}'} (P_{\mathbf{k}'\mathbf{k}} g_{\mathbf{k}'} - P_{\mathbf{k}\mathbf{k}'} g_{\mathbf{k}}) , \quad (1.11)$$

where a possible explicit time dependence is neglected. The scattering rates $P_{\mathbf{k}\mathbf{k}'}$ are determined by a proper quantum mechanical description of the scattering process. In addition, the force $\dot{\mathbf{k}}$ has to be expressed by the electric and magnetic fields. Here, the Lagrangian approach of Sundaram and Niu [37] is a possible way to identify the force term under applied fields.

The aim of the following sections is to identify the different contributions to the current entering via the velocity, or via the distribution function, or via both of them.

The intrinsic contribution

Starting with Karplus and Luttinger [32] several authors [33, 34, 36, 37, 43] found an impurity independent contribution to the AHE caused by the ideal crystal only. This mechanism is not as intuitive as the asymmetric scattering but can, nevertheless, contribute significantly to the anomalous Hall current.

The origin of this contribution is an additional velocity usually called *anomalous* velocity. In the semiclassical Boltzmann approach the net velocity takes the form [37, 38, 44]

$$\mathbf{v}_{\mathbf{k}} = \frac{\partial E_{\mathbf{k}}}{\partial \mathbf{k}} + e\mathbf{E} \times \boldsymbol{\Omega}_{\mathbf{k}} . \quad (1.12)$$

The first term is the usual velocity as the derivative of a band energy with respect to the crystal momentum \mathbf{k} . The second term is linear with the applied electric field \mathbf{E} and $\boldsymbol{\Omega}$ is the so-called *Berry curvature* [46]. It can be expressed in terms of the periodic part $u_{\mathbf{k}}(\mathbf{r})$ of the Bloch wave function $\Psi_{\mathbf{k}}(\mathbf{r}) = u_{\mathbf{k}}(\mathbf{r})e^{i\mathbf{k}\cdot\mathbf{r}}$:

$$\boldsymbol{\Omega}_{\mathbf{k}} = i \begin{pmatrix} \left(\frac{\partial u_{\mathbf{k}}}{\partial k_y}, \frac{\partial u_{\mathbf{k}}}{\partial k_z} \right) - \left(\frac{\partial u_{\mathbf{k}}}{\partial k_z}, \frac{\partial u_{\mathbf{k}}}{\partial k_y} \right) \\ \left(\frac{\partial u_{\mathbf{k}}}{\partial k_z}, \frac{\partial u_{\mathbf{k}}}{\partial k_x} \right) - \left(\frac{\partial u_{\mathbf{k}}}{\partial k_x}, \frac{\partial u_{\mathbf{k}}}{\partial k_z} \right) \\ \left(\frac{\partial u_{\mathbf{k}}}{\partial k_x}, \frac{\partial u_{\mathbf{k}}}{\partial k_y} \right) - \left(\frac{\partial u_{\mathbf{k}}}{\partial k_y}, \frac{\partial u_{\mathbf{k}}}{\partial k_x} \right) \end{pmatrix} . \quad (1.13)$$

The second contribution is already linear in the electric field and omitting higher orders the current is

$$\mathbf{J}_{intr} = -e^2 \sum_{\mathbf{k}} \mathbf{E} \times \boldsymbol{\Omega}_{\mathbf{k}} f_{\mathbf{k}}^{eq} . \quad (1.14)$$

In a system with time inversion symmetry this would give a zero contribution to the anomalous Hall current, because the Berry curvature vanishes $\boldsymbol{\Omega} = 0$.

Is it possible to understand in an easy way where the anomalous velocity comes from? It is related to the basic assumption of the semiclassical approach. The assumption is that the motion of a quasiparticle is restricted to only one band and no transition to other bands are considered. Exactly this approximation is violated in the relativistic case under an applied electric field. This was already found by Karplus and Luttinger [32] and Smit [33, 34]. As a result, the off-diagonal matrix elements of the periodic part of the Bloch functions with the Hamilton operator induced by the electric field are non-zero

$$e \left(u_{\mathbf{k}}^{\nu}(\mathbf{r}), \mathbf{E} \cdot \mathbf{r} u_{\mathbf{k}}^{\nu'}(\mathbf{r}) \right) = i e \mathbf{E} \left(u_{\mathbf{k}}^{\nu}(\mathbf{r}), \frac{\partial u_{\mathbf{k}}^{\nu'}(\mathbf{r})}{\partial \mathbf{k}} \right) \neq 0 \quad (1.15)$$

in the band indices ν . If the semiclassical language with one band only should be retained, then the effect of interband transitions due to the electric field have to be incorporated via the Berry curvature. This origin was nicely discussed by Shindou and Imura [47]. Let us take the z-component of the Berry curvature (1.13) and assume that the \mathbf{k} -dependent Hamiltonian has for a certain \mathbf{k} -point the eigenstates $u^{\nu}(\mathbf{r})$ which form a complete set

$$\sum_{\nu=1}^N u_{\mathbf{k}}^{\nu}(\mathbf{r})(u_{\mathbf{k}}^{\nu}(\mathbf{r}'))^* = \delta(\mathbf{r} - \mathbf{r}') . \quad (1.16)$$

If we introduce this complete set into the definition of the Berry curvature (1.13) it yields the expression

$$\Omega_{\mathbf{k}}^z = i \sum_{\nu} \left[\left(\frac{\partial u_{\mathbf{k}}}{\partial k_x}, u_{\mathbf{k}}^{\nu} \right) \left(u_{\mathbf{k}}^{\nu}, \frac{\partial u_{\mathbf{k}}}{\partial k_y} \right) - \left(\frac{\partial u_{\mathbf{k}}}{\partial k_y}, u_{\mathbf{k}}^{\nu} \right) \left(u_{\mathbf{k}}^{\nu}, \frac{\partial u_{\mathbf{k}}}{\partial k_x} \right) \right] . \quad (1.17)$$

Neglecting the contributions of other bands would be perfectly alright if no other state exist in the system. The complete set would be only one band

$$u_{\mathbf{k}}(\mathbf{r})(u_{\mathbf{k}}(\mathbf{r}'))^* = \delta(\mathbf{r} - \mathbf{r}') \quad (1.18)$$

and the Berry curvature would read as

$$\Omega_{\mathbf{k}}^z = i \left[\left(\frac{\partial u_{\mathbf{k}}}{\partial k_x}, u_{\mathbf{k}} \right) \left(u_{\mathbf{k}}, \frac{\partial u_{\mathbf{k}}}{\partial k_y} \right) - \left(\frac{\partial u_{\mathbf{k}}}{\partial k_y}, u_{\mathbf{k}} \right) \left(u_{\mathbf{k}}, \frac{\partial u_{\mathbf{k}}}{\partial k_x} \right) \right]. \quad (1.19)$$

Using the normalization of the wave function ($u_{\mathbf{k}}, u_{\mathbf{k}} = 1$), it can be shown

$$\frac{\partial}{\partial \mathbf{k}} (u_{\mathbf{k}}, u_{\mathbf{k}}) = 0 = \left(\frac{\partial u_{\mathbf{k}}}{\partial \mathbf{k}}, u_{\mathbf{k}} \right) + \left(u_{\mathbf{k}}, \frac{\partial u_{\mathbf{k}}}{\partial \mathbf{k}} \right) = \left(\frac{\partial u_{\mathbf{k}}}{\partial \mathbf{k}}, u_{\mathbf{k}} \right) + \left(\frac{\partial u_{\mathbf{k}}}{\partial \mathbf{k}}, u_{\mathbf{k}} \right)^* \quad (1.20)$$

that all scalar products in Eq. (1.19) are pure imaginary. That yields into pure real numbers for the products in Eq. (1.19) and in combination with the fact that the second term is just the conjugate complex of the first term it gives

$$\Omega_{\mathbf{k}}^z = 0. \quad (1.21)$$

It is true for a system with only one band.

The above consideration clearly shows that the Berry curvature of a single band system would be zero. Furthermore, it is possible to proof [47] that describing the system in a multiband model, including the complete set of a system, would yield into a vanishing Berry curvature. The Berry curvature is an effect of the special way of describing the system in the semiclassical approach. In a quantum mechanical (Kubo formalism) description of the anomalous Hall effect [35, 43, 44] the anomalous velocity would show up in the off-diagonal terms of the velocity matrix in the band representation which is quite similar to what we discussed in the semiclassical approach.

The extrinsic contribution

Following the definition given above, the extrinsic contributions are caused by scattering events of Bloch states at impurities or any other imperfections of the ideal crystal. Originally two main effects were considered - the skew scattering [33, 34] and the side-jump effect [39, 40]. Already Smit [34] found the side-jump contribution but he argued this term would identically cancel with the intrinsic contribution discussed above. It turned out that this is not the case [39, 40, 42, 44].

The two effects were described [39] starting with a wave packet which is scattered at an imperfection of the lattice including spin-orbit interaction. If the expectation value of the position operator is calculated after the collision event two contributions can be identified. Firstly, the center of the wave packet is shifted instantaneously due to the scattering event. This is called the *side-jump* contribution. Secondly, the expectation value continuously deviates in time from the initial path of the wave packet which is called *skew scattering*. The important fact is that the direction of the scattering is spin dependent. If the spin points out of the plane spanned by the incoming direction and the outgoing direction of the wave packet than it is scattered to the opposite side in comparison to a wave packet with opposite spin. Both effects are depicted in Fig. 1.9 where the lines represent the expectation value of the position operator evolving in time.

How can the charge current be described using Eqs. (1.9) and (1.11)? Both effects are caused by scattering at imperfections. That is why the scattering has to be described properly. Usually, Fermi's Golden rule [44]

$$P_{\mathbf{k}\mathbf{k}'}^{\nu\nu'} = \frac{2\pi}{\hbar} |\tilde{T}_{\mathbf{k}\mathbf{k}'}^{\nu\nu'}|^2 \delta(E_{\mathbf{k}}^{\nu} - E_{\mathbf{k}'}^{\nu'}) \quad (1.22)$$

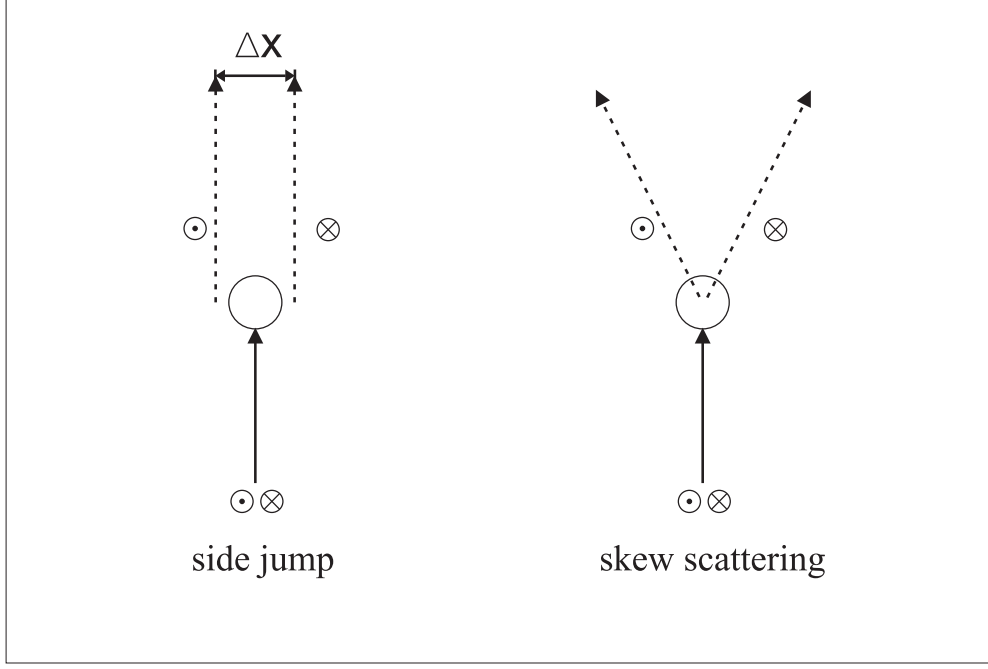


Figure 1.9: The extrinsic contribution to the spin Hall effect is usually separated into the side-jump and the skew scattering mechanism.

is used for the scattering part of the Boltzmann equation (1.11). The expression connects the scattering rate with the corresponding scattering \hat{T} -matrix. Under the influence of spin-orbit coupling the microscopic reversibility is not valid any more ($P_{\mathbf{k}\mathbf{k}'}^{\nu\nu'} \neq P_{\mathbf{k}'\mathbf{k}}^{\nu'\nu}$) which leads directly to the asymmetry needed to incorporate the skew scattering mechanism.

The problem is that the side-jump contribution shows up as a phase change in the scattering \hat{T} -matrix and is therefore not included in the scattering rate. For a description of the side-jump Sinitsyn et al. [42] proposed a renormalization of the velocity to take the coordinate shifts into account. The velocity is then given by

$$\mathbf{v}_{\mathbf{k}} = \mathbf{v}_{\mathbf{k}}^0 + \mathbf{v}_{\mathbf{k}}^{int} + \mathbf{v}_{\mathbf{k}}^{sj} = \frac{\partial E_{\mathbf{k}}}{\partial \mathbf{k}} + e\mathbf{E} \times \boldsymbol{\Omega}_{\mathbf{k}} + \sum_{\mathbf{k}'} P_{\mathbf{k}'\mathbf{k}} \delta r_{\mathbf{k}'\mathbf{k}}^a, \quad (1.23)$$

with the coordinate shift $\delta r_{\mathbf{k}'\mathbf{k}}^a$ which can be expressed in terms of the Berry connection $i(u, \frac{\partial u}{\partial \mathbf{k}})$ [42, 43]. This coordinate shift is independent on the perturbation and just given by the band structure of the ideal crystal. The velocity correction due to the side-jump effect is independent on the applied electric field. For the current being linear in the electric field the corrections of the distribution function due to the electric field have to be taken into account. The extrinsic contributions to the current are

$$\mathbf{J}_{extr} = \mathbf{J}_{sj} + \mathbf{J}_{ss} = -e \sum_{\mathbf{k}} \left(\sum_{\mathbf{k}'} P_{\mathbf{k}'\mathbf{k}} \delta r_{\mathbf{k}'\mathbf{k}}^a g_{\mathbf{k}} + \frac{\partial E_{\mathbf{k}}}{\partial \mathbf{k}} g_{\mathbf{k}} \right). \quad (1.24)$$

In the literature the non-equilibrium part of the distribution function $g_{\mathbf{k}}$ is sometimes split into several contributions to identify the mechanisms more clearly. In addition, it is possible to expand the transition rate in powers of the perturbing potential. This can lead to a distinction of further contributions. Sinitsyn identified the *intrinsic skew scattering* and a contribution caused by an *anomalous distribution*. Here, I will not

comment on those contributions since throughout my work an additional assumption for the scattering rate is made. The problem is restricted to dilute alloys where one impurity can not interact with another one. Under such an assumption the scattering rate (1.22) simplifies to

$$P_{\mathbf{k}\mathbf{k}'}^{\nu\nu'} = \frac{2\pi}{\hbar} c_0 N |T_{\mathbf{k}\mathbf{k}'}^{\nu\nu'}|^2 \delta(E_{\mathbf{k}}^{\nu} - E_{\mathbf{k}'}^{\nu'}), \quad (1.25)$$

where $c_0 N$ is the number of impurities. The scattering rate is linear in the concentration and the dependence of the conductivities on the concentration can easily be discussed. Following the Boltzmann equation (1.11) the non-equilibrium distribution function must be inversely proportional to the concentration. With the expression for the extrinsic part of the current (1.24) the skew scattering is clearly inversely proportional to the concentration and the side-jump effect is independent of the impurity concentration. This result makes the separation into intrinsic and extrinsic contributions questionable. The side-jump is clearly a result of a scattering event but at the same time the induced current is independent on the impurity concentration similar to the intrinsic contribution (1.14).

In summary we identified three contributions to the AHE, i.e. the SHE. Those are the intrinsic mechanism induced by the ideal crystal and the side-jump and skew scattering effect induced by imperfections in the lattice. The total current is given by

$$\mathbf{J}_{Hall} = \mathbf{J}_{intr}(c_0^0) + \mathbf{J}_{sj}(c_0^0) + \mathbf{J}_{ss}(c_0^{-1}), \quad (1.26)$$

where the parts show different dependencies on the impurity concentration. The longitudinal current in the dilute limit is also inversely proportional to the impurity concentration. In the appendix A I will show that under those assumptions the widely used dependence

$$\rho_{yx}^{ss} \propto \rho_{xx} \quad (1.27)$$

$$\rho_{yx}^{sj} \propto (\rho_{xx})^2 \quad (1.28)$$

holds. It is correct if the scattering rate is proportional to the concentration but has been shown to fail if this assumption is not valid [41]. In my work I focus on the description of the skew scattering mechanism since this contribution could easily be identified experimentally by varying the impurity concentration.

Chapter 2

Theoretical background

In this chapter the theoretical concepts and methods used throughout my work are introduced. It is separated into four parts.

It starts with a brief introduction of the *ab initio* method which is based on density functional theory (DFT) and the relativistic version of the Korringa-Kohn-Rostoker (KKR) method. All calculations are based on that concept and, therefore, they are restricted to the considered approximations. Since the spin-orbit interaction is the key for the description of the spin Hall effect, all considerations are based on the solution of the Dirac equation.

In the following the numerical procedure to find the eigenvalues and eigenvectors of the electronic system described by the KKR method is explained. In addition, a numerical robust method for the calculation of Fermi velocities is introduced. Also the spin degree of freedom of the wave functions is discussed in detail.

The third part is dedicated to the description of spin-relaxation processes. It is outlined how to calculate the spin-flip scattering time caused by impurities within the KKR method.

Electronic transport is the topic of the last part of the chapter. It contains an introduction to the linearized Boltzmann equation with a quantum mechanical collision term and the charge and spin conductivity tensor in the semiclassical approach.

2.1 Electronic structure

2.1.1 Density functional theory

The starting point of the quantum mechanical description of a solid is the Schrödinger equation for the wave function $|\Psi\rangle$

$$\hat{H} |\Psi\rangle = E |\Psi\rangle \quad (2.1)$$

with a Hamiltonian \hat{H} using the Dirac representation. This operator consists of the following parts

$$\begin{aligned} \hat{T}_e & \dots \text{kinetic energy of the electrons} \\ \hat{T}_c & \dots \text{kinetic energy of the nuclei} \\ \hat{U}_{ee} & \dots \text{electron-electron interaction potential} \\ \hat{U}_{ec} & \dots \text{electron-nuclei interaction potential} \\ \hat{U}_{cc} & \dots \text{nuclei-nuclei interaction potential} . \end{aligned}$$

The first and fundamental approximation is to separate the motion of the electrons from the vibrations of the lattice. This is the Born-Oppenheimer approximation [48] which is valid at $T = 0$ and for many systems it is also justified for higher temperatures, since the velocity of the electrons is significantly larger than the mobility of the nuclei. The Schrödinger equation for the electronic part

$$\hat{H} |\Psi_e\rangle = (\hat{T}_e + \hat{U}_{ee} + \hat{U}_{ec}) |\Psi_e\rangle = E |\Psi_e\rangle \quad (2.2)$$

is still impossible to solve. The problematic term is the electron-electron interaction \hat{U}_{ee} which couples the motion of $\sim 10^{23}$ particles. The basic idea of Hohenberg and Kohn [49] was to switch from a description of the system with a wave function depending on 10^{23} coordinates to an effective density

$$n(\mathbf{r}) = N \int d\mathbf{r}_2 \dots \int d\mathbf{r}_N |\Psi_e(\mathbf{r}, \mathbf{r}_2, \dots, \mathbf{r}_N)|^2 , \quad (2.3)$$

where the integration over the real space gives the number of particles N . Moreover, the key result of the Hohenberg-Kohn theorem is that the external potential of the electron-nuclei interaction can be written uniquely in terms of the effective density

$$\langle \Psi_e | U_{ec} | \Psi_e \rangle = U_{ec} [n(\mathbf{r})] = \int d^3r U(\mathbf{r}) n(\mathbf{r}). \quad (2.4)$$

The energy of the system is then given by a functional of the density

$$E = \langle \Psi_e | \hat{H} | \Psi_e \rangle = E [n(\mathbf{r})] \quad (2.5)$$

and the energy of the ground state is the absolute minimum at the ground state density

$$E_0 = E [n_0(\mathbf{r})] \leq E [n(\mathbf{r})] . \quad (2.6)$$

In principle, the problem is solved by varying the functional with respect to the density

$$\frac{\delta E [n(\mathbf{r})]}{\delta n(\mathbf{r})} = 0. \quad (2.7)$$

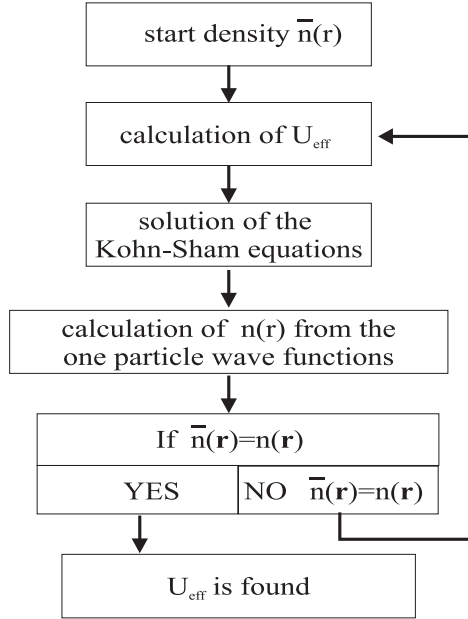


Figure 2.1: Schematic loop of the iteration process for solving the Kohn-Sham equations

However, the main problem is the unknown functional dependence of the electron-electron interaction and the kinetic energy on the density

$$\langle \Psi_e | U_{ee} | \Psi_e \rangle = U_{ee}[n(\mathbf{r})] \text{ and} \quad (2.8)$$

$$\langle \Psi_e | T | \Psi_e \rangle = T[n(\mathbf{r})] . \quad (2.9)$$

The widely used ansatz of Kohn and Sham [50] is based on a separation into a part describing non-interacting electrons and an unknown functional of the effective one-particle density describing the exchange and the correlation of the electrons

$$\left(-\frac{\hbar^2}{2m} \nabla^2 + U_{eff}(\mathbf{r}) \right) \Psi_i(\mathbf{r}) = E_i \Psi_i(\mathbf{r}) \quad (2.10)$$

$$U_{eff}(\mathbf{r}) = U(\mathbf{r}) + \int d^3r' \frac{e^2 n(\mathbf{r}')}{|\mathbf{r} - \mathbf{r}'|} + \frac{\delta E_{xc}[n(\mathbf{r})]}{\delta n(\mathbf{r})} \quad (2.11)$$

with $\Psi_i(\mathbf{r})$ being the effective one-particle wave functions. Here the particle density is given by

$$n(\mathbf{r}) = \sum_{i=1}^N |\Psi_i(\mathbf{r})|^2 . \quad (2.12)$$

This set of equations (Kohn-Sham equations) can be solved iteratively as sketched in Fig. (2.1). All problems are hidden in the unknown exchange and correlation potential $E_{xc}[n(\mathbf{r})]$. One further widely used approach is the local-density approximation (LDA), where a locally slow varying density is assumed. In this situation the exchange-correlation potential can be expressed via the exchange-correlation functional of the non-interacting homogeneous electron gas

$$E_{xc}^{LDA}[n(\mathbf{r})] = \int d^3r n(\mathbf{r}) \epsilon_{xc}^{hom}[n(\mathbf{r})] . \quad (2.13)$$

With this at least an electronic structure calculation becomes possible and only the method to solve the Kohn-Sham equations (2.10) has to be specified.

2.1.2 Dirac equation

The basic ingredient for the description of the spin Hall effect is the spin-orbit coupling. In principle, it could be included perturbatively starting with the non-relativistic solution of the electronic structure calculations described above. We choose another way by solving the Dirac equation instead of the Schrödinger or Pauli equation. For a relativistic DFT the same theorems as in the non-relativistic description are used. The relativistic Kohn-Sham-Dirac equations are expressed generally by [51]

$$\hat{H}\Psi_i(\mathbf{r}) = \left[c \hat{\boldsymbol{\alpha}} \cdot \hat{\mathbf{p}} + \hat{\beta}mc^2 + I_4 U_{eff}[n, \mathbf{m}] + \hat{\beta} \hat{\boldsymbol{\Sigma}} \cdot \mathbf{B}_{eff}[n, \mathbf{m}] \right] \Psi_i(\mathbf{r}), \quad (2.14)$$

with the effective potential

$$U_{eff}[n, \mathbf{m}] = U_{ext}(\mathbf{r}) + \int d^3r' \frac{e^2 n(\mathbf{r}')}{|\mathbf{r} - \mathbf{r}'|} + \frac{\delta E_{xc}[n(\mathbf{r}), \mathbf{m}(\mathbf{r})]}{\delta n(\mathbf{r})}, \quad (2.15)$$

and the effective magnetic field

$$\mathbf{B}_{eff}[n, \mathbf{m}] = \mathbf{B}_{ext}(\mathbf{r}) + \frac{\delta E_{xc}[n(\mathbf{r}), \mathbf{m}(\mathbf{r})]}{\delta \mathbf{m}(\mathbf{r})}, \quad (2.16)$$

including an external magnetic field $\mathbf{B}_{ext}(\mathbf{r})$. The Dirac matrices are given by

$$\hat{\boldsymbol{\alpha}} = \begin{pmatrix} 0 & \boldsymbol{\sigma} \\ \boldsymbol{\sigma} & 0 \end{pmatrix}, \quad \hat{\boldsymbol{\Sigma}} = \begin{pmatrix} \boldsymbol{\sigma} & 0 \\ 0 & \boldsymbol{\sigma} \end{pmatrix}, \quad (2.17)$$

$$\hat{\beta} = \begin{pmatrix} \hat{I}_2 & 0 \\ 0 & -\hat{I}_2 \end{pmatrix}, \quad \hat{I}_4 = \begin{pmatrix} \hat{I}_2 & 0 \\ 0 & \hat{I}_2 \end{pmatrix}, \quad (2.18)$$

where \hat{I}_2 is the 2×2 unit matrix, and $\boldsymbol{\sigma}$ are the Pauli matrices σ_x , σ_y , and σ_z .

2.1.3 Green function method

To solve the Kohn-Sham equations several methods were developed over the last decades. In my thesis I use a Korringa-Kohn-Rostoker Green function method which I now introduce briefly. As indicated by the name, it is based on the solution of the differential equation via the Green function.

Lets assume we have two differential equations

$$\begin{aligned} \hat{H}_0 |\Psi_i^0\rangle &= E_i^0 |\Psi_i^0\rangle \text{ and} \\ (\hat{H}_0 + V) |\Psi_i\rangle &= E_i |\Psi_i\rangle, \end{aligned} \quad (2.19)$$

where the operators on the left hand site differ by a scalar potential. Furthermore, the solution of the first equation is known whereas the second one has to be solved. The Green functions of the two systems are then defined by the operator equations

$$\begin{aligned} (E - \hat{H}_0) \hat{G}_0 &= \hat{I} \\ &\text{and} \\ (E - \hat{H}_0 - V) \hat{G} &= \hat{I}. \end{aligned} \quad (2.20)$$

The product of the differential operator with the Green function operator is the unity operator. The equations can symbolically be solved by inverting the differential operator

$$\begin{aligned}\hat{G}_0 &= (E - \hat{H}_0)^{-1} \\ \text{and} \\ \hat{G} &= (E - \hat{H}_0 - V)^{-1} .\end{aligned}\quad (2.21)$$

From these expressions the Dyson equation for the unknown Green function

$$\hat{G} = \hat{G}_0 + \hat{G}_0 V \hat{G} \quad (2.22)$$

can be deduced. The known system is usually called the reference system.

A similar equation for the wave functions of the reference $|\Psi_i^0\rangle$ and the unknown $|\Psi_i\rangle$ systems

$$|\Psi_i\rangle = |\Psi_i^0\rangle + \hat{G}_0 \hat{V} |\Psi_i\rangle \quad (2.23)$$

is called the Lippmann-Schwinger equation [52]. Defining the \hat{t} operator with

$$\hat{t}|\Psi_0\rangle = \hat{V}|\Psi_0\rangle \quad (2.24)$$

yields

$$\hat{t} = \hat{V}(\hat{I} - \hat{G}_0 \hat{V})^{-1} . \quad (2.25)$$

Thus, if the potential perturbation \hat{V} and the Green function of the reference system \hat{G}_0 is known, the operator can be calculated and the wave function

$$|\Psi\rangle = |\Psi_0\rangle + \hat{G}_0 \hat{t} |\Psi_0\rangle , \quad (2.26)$$

as well as, the Green function of the real system under consideration

$$\hat{G} = \hat{G}_0 + \hat{G}_0 \hat{t} \hat{G}_0 \quad (2.27)$$

can be calculated.

As discussed above, in density functional theory the most important quantity is the electron density, which is connected to the Green function using the spectral representation of \hat{G} [53]

$$\hat{G}(E + i\eta) = \sum_i \frac{|\Psi_i\rangle \langle \Psi_i|}{E + i\eta - E_i} . \quad (2.28)$$

The wave functions are solutions of the hermitian operator

$$(E + i\eta - \hat{H}_0 - \hat{V}) |\Psi_i\rangle = (E + i\eta - E_i) |\Psi_i\rangle . \quad (2.29)$$

The parameter $E + i\eta$ represents the upper part of the complex energy plane with $\eta > 0$. The relation between the Green function and the electron density is

$$n(\mathbf{r}) = \int_{-\infty}^{E_F} dE n(\mathbf{r}, E) = -\frac{1}{\pi} \int_{-\infty}^{E_F} dE \text{Im}\{G^+(\mathbf{r}, \mathbf{r}, E)\} , \quad (2.30)$$

where only the imaginary part of the Green function, in the limit of $\eta \rightarrow 0$, is needed. Here, I used the real space representation of the diagonal element of the Green function

$$\lim_{\eta \rightarrow 0} \langle \mathbf{r} | \hat{G}(E + i\eta) | \mathbf{r} \rangle = G^+(\mathbf{r}, \mathbf{r}, E) . \quad (2.31)$$

The density of states is calculated from the volume integral of the imaginary part of the diagonal element of the Green function

$$n(E) = -\frac{1}{\pi} \int d^3r \operatorname{Im}\{G^+(\mathbf{r}, \mathbf{r}, E)\} . \quad (2.32)$$

The + represents the limit in the upper part of the complex energy plane and the Green function is called advanced Green function .

2.1.4 Relativistic KKR method

The code, which is used to solve the Dyson equation (2.22), is based on the Korringa-Kohn-Rostoker method [54, 55]. In the present work a relativistic extension [51, 56] of the screened KKR [57, 58] is employed. The theoretical concepts of that extension were developed by several authors [56, 59–67] during the last 40 years.

Here, only the basics, which are important in the following chapters, are discussed. For further details the reader is referred to the cited literature and the PhD thesis of P. Zahn [68], J. Binder [69], and M. Czerner [70].

The starting point is the definition of the Green function (2.20)

$$\hat{G}^{-1} = (E - \hat{H}_0 - V) \quad (2.33)$$

for the relativistic Dirac Hamiltonian as in Eq. (2.14). The potential is arbitrary and the system can be an infinite crystal. The problem is numerically very demanding and further approximations are necessary. The most important one is the restriction to spherical symmetric potentials at every atomic position. It seems to be quite natural since an isolated atom would have this symmetry. However, in a crystal this is not the case and the approximation neglects non-spherical contributions to the potential. In Fig. 2.2 a) the potential landscape in the so-called muffin-tin (MT) approximation is sketched. In the non-overlapping muffin-tin spheres we have the potential V and in the interstitial region the potential is fixed to a constant value. The problem of the muffin-tin approximation is the empty space. To reduce it all spheres are enlarged until they reach the volume of the system. This is called atomic sphere approximation (ASA) and all spheres can overlap. The volume is correct and the interstitial region is neglected, but all overlapping regions are counted twice in the system. This method is valid if the integral over the overlapping regions give the same contribution as the interstitial, so the quantity should vary slowly. Usually, the ASA approximation works well for metals. For the description of the potential in ASA approximation cell-centered coordinates as depicted in Fig. (2.3) are introduced. Using this, the crystal potential can be written as

$$V(\mathbf{r}) = \sum_n V^n(|\mathbf{r}_n - \mathbf{R}^n|) , \quad (2.34)$$

where the spherical potential at every atomic site is expressed by

$$V^n(|\mathbf{r}_n - \mathbf{R}^n|) = \begin{cases} V_{atom}^n(|\mathbf{r}_n - \mathbf{R}^n|) & \text{if } |\mathbf{r}_n - \mathbf{R}^n| < R_{ASA}^n \\ 0 & \text{if } |\mathbf{r}_n - \mathbf{R}^n| > R_{ASA}^n \end{cases} . \quad (2.35)$$

Eq. (2.33) simplifies to

$$\left[E + \frac{\hbar^2}{2m} \nabla^2 - V^n(r) \right] G(\mathbf{R}^n + \mathbf{r}, \mathbf{R}^{n'} + \mathbf{r}', E) = \delta_{n,n'} \delta(\mathbf{r} - \mathbf{r}') , \quad (2.36)$$

which is an inhomogeneous differential equation. The inhomogeneity vanishes if the coordinates are not in the same cell. This homogeneous differential equation defines the multiple-scattering solution (*structural* Green function $G_{QQ'}^{mn'}(E)$), since it connects the different atomic positions. The inhomogeneous equation defines the single scattering problem (*on site* Green function $G_S^n(\mathbf{r}, \mathbf{r}', E)$) at a single atom. The full solution can be written as the general solution of the homogeneous problem in combination with a special solution of the inhomogeneous equation

$$G^{mn'}(\mathbf{r}, \mathbf{r}', E) = \delta_{nn'} G_S^n(\mathbf{r}, \mathbf{r}', E) + \sum_{QQ'} \Phi_Q^n(\mathbf{r}, E)^\times G_{QQ'}^{mn'}(E) \Phi_{Q'}^{n'}(\mathbf{r}', E). \quad (2.37)$$

Here the abbreviation

$$G(\mathbf{R}^n + \mathbf{r}, \mathbf{R}^{n'} + \mathbf{r}', E) = G^{mn'}(\mathbf{r}, \mathbf{r}', E) \quad (2.38)$$

for the Green function is used. The multiple-scattering term is expanded into the scattering solutions of the single-site scatterer

$$\Phi_Q^n(\mathbf{r}, E) = \sum_{Q'} \begin{pmatrix} g_{Q'Q}(r) \chi_{Q'}(\hat{\mathbf{r}}) \\ i f_{Q'Q}(r) \chi_{\bar{Q}'}(\hat{\mathbf{r}}) \end{pmatrix}, \quad (2.39)$$

where \times means the conjugate complex of the non-radial part only

$$\Phi_Q^n(\mathbf{r}, E)^\times = \sum_{Q'} \begin{pmatrix} g_{Q'Q}(r) \chi_{Q'}^\dagger(\hat{\mathbf{r}}) \\ -i f_{Q'Q}(r) \chi_{\bar{Q}'}^\dagger(\hat{\mathbf{r}}) \end{pmatrix}. \quad (2.40)$$

These regular solutions are expanded into the spin angular functions $\chi_Q(\hat{\mathbf{r}})$ depending on the direction of \mathbf{r} and the radial solutions of the single site problem, $g_{Q'Q}(r)$ and $f_{Q'Q}(r)$, depending on the norm $r = |\mathbf{r}|$. The spin angular functions are labeled by the index $Q = \{\kappa, \mu\}$ and $\bar{Q} = \{-\kappa, \mu\}$. The quantum numbers κ and μ are defined by

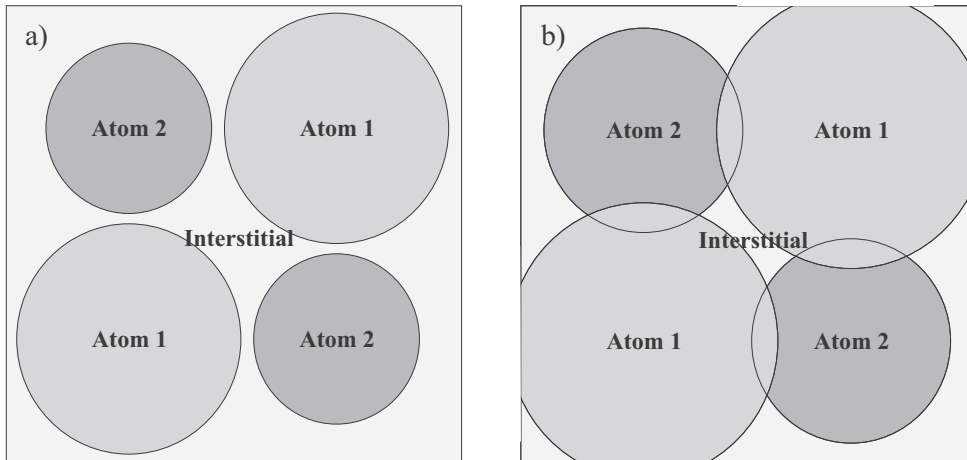


Figure 2.2: two-dimensional sketch of the potential landscape in a) muffin-tin (MT) und b) atomic-sphere approximation (ASA)

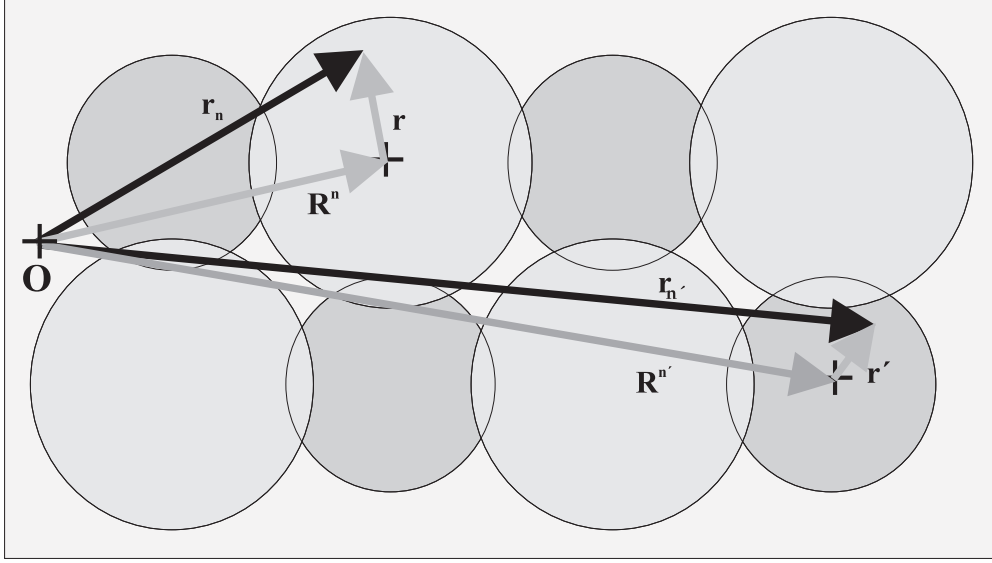


Figure 2.3: global (black) und cell-centered (grey) coordinates

$\chi_Q(\hat{\mathbf{r}})$ being the eigenfunction of the square of the total angular momentum \mathbf{J}^2 , its z component J_z , and the operator $\hat{K} = \boldsymbol{\sigma} \cdot \mathbf{L} + \hat{I}$ (spin-orbit interaction)

$$\begin{aligned} \mathbf{J}^2 \chi_Q(\hat{\mathbf{r}}) &= j(j+1) \chi_Q(\hat{\mathbf{r}}) \\ J_z \chi_Q(\hat{\mathbf{r}}) &= \mu \chi_Q(\hat{\mathbf{r}}) \\ K \chi_Q(\hat{\mathbf{r}}) &= -\kappa \chi_Q(\hat{\mathbf{r}}). \end{aligned} \quad (2.41)$$

They can be expressed in terms of complex spherical harmonics $Y_{l,m}(\hat{\mathbf{r}})$ and the spinor basis functions ϕ_s [51]

$$\chi_Q(\hat{\mathbf{r}}) = \sum_s C(l, \kappa, \frac{1}{2} | (\mu - s), s) Y_{l, \mu - s}(\hat{\mathbf{r}}) \phi_s, \quad (2.42)$$

where $C(l, \kappa, \frac{1}{2} | (\mu - s), s)$ are the Clebsh-Gordan coefficients.

The task is now to find the Green function \hat{G} of the considered real system via the Dyson equation (2.22) starting from a known reference system (\hat{G}_0). Inserting (2.37) into (2.22) yields the Dyson equation for the *on site* Green function

$$g_s^n(\mathbf{r}, \mathbf{r}', E) = \hat{g}_s^n(\mathbf{r}, \mathbf{r}', E) + \int d\mathbf{r}'' \hat{g}_s^n(\mathbf{r}, \mathbf{r}'', E) V_n(\mathbf{r}'') g_s^n(\mathbf{r}'', \mathbf{r}', E) \quad (2.43)$$

and an algebraic Dyson equation for the structural Green function

$$G_{QQ'}^{mn'}(E) = \hat{G}_{QQ'}^{mn'}(E) + \sum_{Q'', n''} \sum_{Q'''} \hat{G}_{QQ''}^{mn''}(E) t_{Q''Q'''}^{n''}(E) G_{Q''Q'}^{m''n'}(E). \quad (2.44)$$

The matrix elements of the single site t-matrix are expressed by the single site scattering solutions of the reference and the real system (2.24)

$$\begin{aligned} t_{Q,Q'}^n(E) &= \int d\mathbf{r} \hat{\Phi}_Q^n(\mathbf{r}) V^n(r) \Phi_{Q'}^n(\mathbf{r}) \\ &= \sum_{Q''} \int_0^{R_{ASA}^n} dr r^2 \left(\hat{g}_{Q''Q}^n g_{Q''Q'}^n + \hat{f}_{Q''Q}^n f_{Q''Q'}^n \right) V_n(r). \end{aligned} \quad (2.45)$$

Fourier transformation and structure constants

A typical problem is to solve the algebraic Dyson equation (2.44) for a three-dimensional periodic crystal. This crystal is described by a basis and a set of three Bravais lattice vectors. For this reason we introduce a new index μ running over the basis atoms and the index n describes the different cells connected by the lattice vectors. Since the periodic potential is independent of the cell index n , this is also true for the t -matrix. The algebraic Dyson equation (2.44) becomes

$$G_{QQ'}^{\mu\mu' nn'} = \mathring{G}_{QQ'}^{\mu\mu' nn'} + \sum_{Q'', \mu'', n''} \sum_{Q'''} \mathring{G}_{QQ''}^{\mu\mu'' nn''} t_{Q''Q'''}^{\mu''} G_{Q''Q'}^{\mu''\mu' n''n'} , \quad (2.46)$$

and I omitted the energy dependence E . In such a form and for a periodic crystal it is natural to apply a Fourier transformation

$$G_{QQ'}^{\mu\mu'}(\mathbf{k}) = \sum_{n'} e^{+i\mathbf{kR}^{0n'}} G_{QQ'}^{\mu\mu' 0n'} \quad (2.47)$$

with the back transformation

$$G_{QQ'}^{\mu\mu' nn'} = \frac{V}{(2\pi)^3} \int_{V_{BZ}} d^3k e^{-i\mathbf{kR}^{nn'}} G_{QQ'}^{\mu\mu'}(\mathbf{k}) . \quad (2.48)$$

In my notation V is the volume of the unit cell and $V_{BZ} = (2\pi)^3/V$ the volume of the first Brillouin zone. If we combine (2.48) and (2.46) we find the Fourier transformed algebraic Dyson equation for the structural constants

$$G_{QQ'}^{\mu\mu'}(\mathbf{k}) = \mathring{G}_{QQ'}^{\mu\mu'}(\mathbf{k}) + \sum_{\mu''Q''} \sum_{Q'''} \mathring{G}_{QQ''}^{\mu\mu''}(\mathbf{k}) t_{Q''Q'''}^{\mu''} G_{Q''Q'}^{\mu''\mu'}(\mathbf{k}) . \quad (2.49)$$

Inverting this matrix equation and introducing the KKR matrix

$$M_{QQ'}^{\mu\mu''}(\mathbf{k}) = \mathring{G}_{QQ'}^{\mu\mu''}(\mathbf{k}) - \delta_{\mu\mu''} [t^{-1}]_{QQ'}^{\mu} \quad (2.50)$$

yields into

$$G_{QQ'}^{\mu\mu'}(\mathbf{k}) = -\delta_{\mu\mu'} [t^{-1}]_{QQ'}^{\mu} - \sum_{Q''Q'''} [t^{-1}]_{QQ''}^{\mu} [M^{-1}(\mathbf{k})]_{Q''Q'''}^{\mu\mu'} [t^{-1}]_{Q''Q'}^{\mu'} . \quad (2.51)$$

If the Green function is known, the electronic density can be calculated (2.30) and in principle, the self-consistent procedure (see Fig. 2.1) can be applied. For a calculation of the Green function using the introduced KKR method the reference system (the known Green function) has to be specified. One could use the free space since its Green function is known analytically. However, several numerical disadvantages would restrict the calculations to less than 100 atoms. The first problem is the long range interaction of the free structural constants. Furthermore, the matrix inversion scales with the number of atoms N as N^3 . Finally the solutions of the free space $E = k^2$ are at the same energy range as the solutions of the real system, that causes singularities in the KKR-matrix. All these problems can be avoided using a screened reference potential as shortly outlined in the next paragraph.

The screening reference system

So far we never specified the reference system. As already mentioned the free space is not the best choice and a screening potential is used (Screened KKR) [57, 58, 68]. The reference system has a repulsive potential at every atomic position screening the structural constants and pushing all states above ~ 1 Ry. The algebraic Dyson equation (2.49) has to be solved in two steps. First, for the reference system \tilde{g} , and then for the real system. The new equations for the real system are similar to Eqs. (2.49), (2.50), and (2.51). Just the single-site \hat{t} matrix is replaced by the difference $\Delta t = t - \tilde{t}$ of the \hat{t} matrix for the reference system and the \hat{t} matrix of the real system with respect to free space. The KKR matrix takes the form

$$M_{QQ'}^{\mu\mu'}(\mathbf{k}) = \tilde{G}_{QQ'}^{\mu\mu'}(\mathbf{k}) - \delta_{\mu\mu'} [\Delta t^{-1}]_{QQ'}^{\mu} . \quad (2.52)$$

In this notation $\tilde{G}_{QQ'}^{\mu\mu'}(\mathbf{k})$ are the structural constants of the reference system which are independent on the actual crystal potential and are only a property of the crystal structure. In addition, the explicit \mathbf{k} dependence is encoded in the structural constants of the reference system.

2.1.5 Impurity problem within the KKR method

In my thesis the influence of impurity atoms on the electronic structure and the electronic transport properties of three-dimensional crystals is discussed. For this purpose the method of calculating the electronic properties of systems with impurities is outlined in the following.

The Green function KKR method is well suited to tackle this problem without using a supercell approach. All ingredients to find the electronic structure of the impurity system are introduced in the previous sections. The key tool is again the Dyson equation. Let us assume that we have solved the three-dimensional problem as discussed above, so we denote the Green function of the system as \mathring{G} . The structural Green function of the perturbed system including a substitutional impurity atom and allowing for charge relaxation around the impurity can be calculated via a real space Dyson equation in the region of the perturbed region. The algebraic Dyson equation has the form

$$G_{QQ'}^{nn'}(E) = \mathring{G}_{QQ'}^{nn'}(E) + \sum_{Q''} \sum_{n''} \mathring{G}_{QQ''}^{nn''}(E) \Delta t_{Q''Q'''}^{n''}(E) G_{Q''Q'}^{n''n'}(E), \quad (2.53)$$

where n and n' are sums over the perturbed real space cluster. Since the reference system of such an impurity calculation is the ideal crystal, the Δt matrix is the difference of the t_0 matrix of the ideal crystal and the t matrix of the perturbed system with respect to free space. For a full impurity calculation the following procedure is applied:

1. Calculation of the structural constants \tilde{g} of the reference system with repulsive potentials from a Fourier transformation of the structural Green function (2.47) on a screened cluster in real space
2. Calculation of the \hat{t} matrix of the reference system with repulsive potentials
3. Calculation of the radial wave functions and t_0 matrices of the periodic potential

4. Calculation of the structural constants \mathring{G} of the periodic system via the algebraic Dyson equation in the reciprocal space (2.46)
5. Calculation of the structural Green function \mathring{G} of the periodic system in a real space cluster corresponding to the perturbed cluster
6. Calculation of the radial wave functions and t matrices of the perturbed cluster
7. Calculation of the structural Green function G in the perturbed cluster via the real space version of the algebraic Dyson equation (2.53)
8. Summation of the *on site* Green function and the multiple scattering term to calculate the perturbed Green function (2.51)

For further readings I refer to the PhD theses of P. Zahn [68] and J. Binder [69].

2.2 Band structure and Fermi surface

In this chapter I outline the basic equations for how to extract the band structure, the Bloch functions, and the Fermi velocity from the KKR method. In addition, the method of calculating the spin expectation value of the Bloch functions is explained.

The first two sections about the band structure, and the wave function evaluation, as well as, the Fermi surface construction are mainly short reviews of the PhD thesis of P. Zahn [68] with extensions to the relativistic case.

The following two sections about the Fermi velocity and the spin expectation value are new features which I implemented in the KKR code. A new way of calculating the Fermi velocity based on an analytic \mathbf{k} derivative of the KKR matrix is shown to be much more stable than the numerical derivative of the band structure.

2.2.1 Evaluation of the eigenvalues and eigenfunctions

Here, the calculation of the band structure and the Bloch functions of the ideal crystal is discussed. It is followed by a description of the wave functions of the perturbed system.

The wave functions of the ideal crystal

The eigenvalue equation of the ideal crystal

$$(E - \hat{H}) \left| \hat{\Psi} \right\rangle = 0 \quad (2.54)$$

in the Green function representation

$$\hat{G}^{-1} \left| \hat{\Psi} \right\rangle = 0 \quad (2.55)$$

follows from the definition of the Green function (2.20). Using the Dyson equation (2.22) and the repulsive potential as reference system the homogeneous integral equation for the Bloch function has the form

$$\hat{\Psi}_{\mathbf{k}}^{n\mu}(\mathbf{r}) = \sum_{n'\mu'} \int d^3r' \tilde{G}^{\mu\mu' n n'}(\mathbf{r}, \mathbf{r}') \hat{V}^{\mu'}(\mathbf{r}') \hat{\Psi}_{\mathbf{k}}^{n'\mu'}(\mathbf{r}') . \quad (2.56)$$

If we expand the Bloch function into the single-site scattering solutions

$$\hat{\Psi}_{\mathbf{k}}^{n\mu}(\mathbf{r}) = \frac{1}{\sqrt{V}} \sum_Q e^{i\mathbf{k}\mathbf{R}^n} \hat{c}_Q^\mu(\mathbf{k}) \hat{R}_Q^\mu(\mathbf{r}) , \quad (2.57)$$

ensuring normalization

$$\left\langle \hat{\Psi}_{\mathbf{k}} | \hat{\Psi}_{\mathbf{k}} \right\rangle = \int_V d^3r \left| \hat{\Psi}_{\mathbf{k}}(\mathbf{r}) \right|^2 = \frac{1}{V} \sum_{\mu=1}^{NEZ} \sum_{QQ'} (\hat{c}_Q^\mu)^* \hat{c}_{Q'}^\mu N_{QQ'}^\mu , \quad (2.58)$$

and with the abbreviation

$$N_{QQ'}^\mu = \int_0^{R_{MT}} dr r^2 \sum_{Q''} \left[\hat{g}_{Q''Q}^* \hat{g}_{Q''Q'} + \hat{f}_{Q''Q}^* \hat{f}_{Q''Q'} \right] , \quad (2.59)$$

we obtain an algebraic eigenvalue equation for the expansion coefficients

$$\sum_{\mu'} \sum_{Q'Q''} \left[[\Delta t_{Q'Q''}^{\mu}]^{-1} \delta_{\mu\mu'} - \tilde{G}_{Q'Q''}^{\mu\mu'} \right] \Delta t_{Q''Q'}^{\mu'} \hat{c}_{Q'}^{\mu'}(\mathbf{k}) = 0 . \quad (2.60)$$

In this derivation we used the fact that the reference system has no solutions in the energy region of interest. Combining the definition of the KKR matrix (2.52) with the algebraic eigenvalue equation (2.60) yields

$$\sum_{\mu'} \sum_{Q'Q''} M_{Q'Q''}^{\mu\mu'}(k) \Delta t_{Q''Q'}^{\mu'} \hat{c}_{Q'}^{\mu'}(\mathbf{k}) = 0 , \quad (2.61)$$

which has the matrix form

$$M(k, E) \Delta t(E) \hat{c}(\mathbf{k}) = 0 . \quad (2.62)$$

In principle, the band structure is well defined by

$$\lambda(E_{\mathbf{k}}, \mathbf{k}) = 0 \quad (2.63)$$

with the eigenvalue equation

$$M(E, \mathbf{k}) a(\mathbf{k}) = \lambda(E, \mathbf{k}) a(\mathbf{k}) . \quad (2.64)$$

The problem is that the KKR matrix M is not hermitian in our definition, which makes it difficult to find the solutions of Eq. (2.64). To solve this problem I apply additional transformations to Eq. (2.62)

$$P^T I M(E, \mathbf{k}) I^{-1} P \quad P^{-1} I \Delta t(E) \hat{c}(\mathbf{k}) = 0 \quad (2.65)$$

with the matrices

$$I_{QQ'} = \sum_s C(l, \kappa, \frac{1}{2} |(\mu - s), s) i^{-l} \delta_{l'l'} C(l', \kappa', \frac{1}{2} |(\mu' - s), s) \quad (2.66)$$

and

$$P_{QQ'} = \sum_s C(l, \kappa, \frac{1}{2} |(\mu - s), s) e^{\tilde{\delta}_l} \delta_{l'l'} C(l', \kappa', \frac{1}{2} |(\mu' - s), s) . \quad (2.67)$$

Here $\tilde{\delta}_Q$ are the phase shifts of the reference system defined as

$$\tan(\tilde{\delta}_l(E)) = \frac{j_l(\sqrt{E} r_{MT})}{n_l(\sqrt{E} r_{MT})} , \quad (2.68)$$

where j_l and n_l are the spherical Bessel and Neumann functions, respectively. This procedure is explained in detail in the PhD thesis of P. Zahn [68] and was generalized to a relativistic description. Both transformations have a different origin. The I transformation takes the special definition of the free space structural constants into account [68]. The reason for the P transformation is the screened KKR formalism. Here the Δt matrix is used and not the ordinary t matrix with the free space as reference system. To bring the KKR matrix in the same form as in the unscreened version the phase shifts of the reference system have to be extracted. Both transformations are

unitary and do not change the band structure. The new hermitian eigenvalue problem takes the form

$$\tilde{M}(E, \mathbf{k})\tilde{c}(E, \mathbf{k}) = 0 . \quad (2.69)$$

The band structure of our system follows from the root zeros of the eigenvalue equation

$$\tilde{M}(E, \mathbf{k})\tilde{c}(E, \mathbf{k}) = \lambda(E, \mathbf{k})\tilde{c}(E, \mathbf{k}) , \quad (2.70)$$

with

$$\lambda(E_{\mathbf{k}}, \mathbf{k}) = 0 \quad (2.71)$$

and the expansion coefficients of the Bloch functions (2.57) are solutions at $\lambda(E_{\mathbf{k}}, \mathbf{k}) = 0$ after applying the back transformation

$$\hat{c}(E_{\mathbf{k}}, \mathbf{k}) = \Delta t^{-1} I^{-1} P \tilde{c}(E_{\mathbf{k}}, \mathbf{k}) . \quad (2.72)$$

The wave functions of the perturbed system

So far we calculated the band structure and the wave functions of the ideal system. However, we are interested in scattering processes. For a description of the perturbed system we need in addition the perturbed wave functions $\Psi_k^{n\mu}(\mathbf{r})$. Those are not translational invariant but they are connected with the Bloch function of the ideal crystal via a Lippmann-Schwinger equation (2.23). If the perturbed wave function is, similarly to the Bloch function (2.57), expanded into the single site scattering solutions at each position

$$\Psi_k^{n\mu}(\mathbf{r}) = \frac{1}{\sqrt{V}} \sum_Q e^{i\mathbf{k}\mathbf{R}^n} c_Q^{n\mu}(\mathbf{k}) R_Q^{n\mu}(\mathbf{r}) , \quad (2.73)$$

a Lippmann-Schwinger like equation for the expansion coefficients can be derived

$$c_Q^{n\mu}(\mathbf{k}) = \hat{c}_Q^{n\mu}(\mathbf{k}) + \sum_{n', \mu', Q'} \sum_{Q''} \hat{G}_{QQ''}^{nn', \mu\mu'} \Delta t_{Q''Q'}^{n', \mu'} c_{Q'}^{n'\mu'}(\mathbf{k}) . \quad (2.74)$$

The formal solution of this problem yields into

$$c_Q^{n\mu}(\mathbf{k}) = \sum_{n', \mu', Q'} D_{QQ'}^{nn', \mu\mu'} \hat{c}_{Q'}^{n'\mu'}(\mathbf{k}') \quad (2.75)$$

with

$$D_{QQ'}^{nn', \mu\mu'} = \delta_{nn'} \delta_{\mu\mu'} \delta_{QQ'} + \sum_{Q''} G_{QQ''}^{nn', \mu\mu'} \Delta t_{Q''Q'}^{n', \mu'} , \quad (2.76)$$

where we used the algebraic Dyson equation (2.53) for the real space cluster.

2.2.2 Evaluation of the Fermi surface

A nice feature of the KKR method is its \mathbf{k} dependence. The important simplification is that it is encoded in the structural constants, which are determined by the geometrical structure only (see Eq. (2.60)). Furthermore, the \mathbf{k} dependence is introduced via the Fourier transformation of the screened structural constants, which is an easy numerical procedure (see section 2.1.4). The influence of the actual potential is given by the Δt matrix, which is independent on \mathbf{k} . All these features allow for an efficient calculation

of the band structure and the Fermi surface.

To determine the Fermi surface we use a tetrahedron method explained in detail in the literature [68,71–73]. The irreducible part of the Brillouin zone is filled with tetrahedra. The iso-energetic surface is determined by calculating all intersections with the edges of the tetrahedra. If the mesh of tetrahedra is small enough the intersections of the iso-energetic surface with one tetrahedron is either a triangle or a quadrangle. All intersections together form the iso-energetic surface.

2.2.3 Evaluation of the Fermi velocity

For all transport calculations the knowledge of the Fermi velocity of the electron states is essential. In this section two methods of calculating the Fermi velocity are presented. The first one is a numerical differentiation of the band structure using the determination of the iso-energetic surface as presented in the last section. The second method is based on an analytic differentiation of the screened structural constants with respect to \mathbf{k} and a simple numerical differentiation because of the energy dependence of the KKR matrix. The energy dependence is numerically much easier to treat and it is a one dimensional derivative instead of the three-dimensional derivative in \mathbf{k} space.

The numerical \mathbf{k} derivative

The task is to find the quantity

$$v_F(\mathbf{k}) = \frac{1}{\hbar} \left. \frac{\partial E(\mathbf{k})}{\partial \mathbf{k}} \right|_{E=E_F} . \quad (2.77)$$

The most natural way is to perform the search for the iso-energetic surface (2.2.3) at two energies - above $E_F + \delta E$ and below $E_F - \delta E$ the Fermi level. The intersections with a tetrahedron are characterized by the points

$$\mathbf{k}_1, \mathbf{k}_2, \mathbf{k}_3 : E_F + \delta E \quad (2.78)$$

$$\tilde{\mathbf{k}}_1, \tilde{\mathbf{k}}_2, \tilde{\mathbf{k}}_3 : E_F - \delta E \quad (2.79)$$

Such points are schematically presented in Fig. (2.4). The approximated Fermi velocity is then given by the system of linear equations

$$\hbar(\mathbf{k}_i - \tilde{\mathbf{k}}_i)\mathbf{v}_F = 2\delta E . \quad (2.80)$$

The accuracy of this procedure strongly depends on the number, i.e. the size, of the used tetrahedra. Especially, for Fermi surfaces with large curvature a very large number of tetrahedra is needed for an accurate calculation of the Fermi velocity. This makes the method inefficient. For this reason I present in the following an alternative way for calculating the Fermi velocity.

The analytic \mathbf{k} derivative

The main ideas were provided by Shirokovskii and Shilkova [74, 75]. Here they are extended to non-hermitian matrices. The starting point for this procedure is the KKR

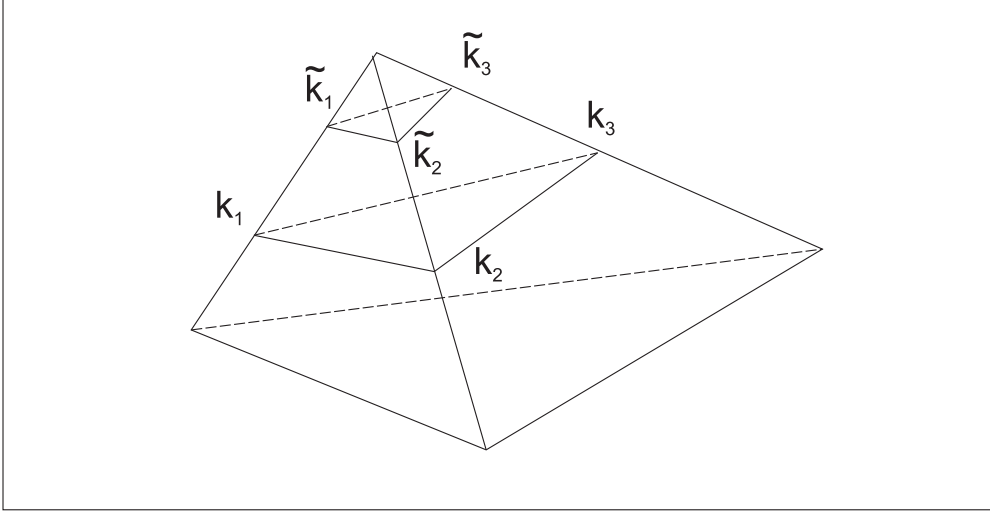


Figure 2.4: The intersections of the iso-energetic surfaces slightly above $E_F + \delta E$ and below $E_F - \delta E$ the Fermi energy with a tetrahedron in the Brillouin zone for the numerical derivative of the dispersion relation.

eigenvalue problem (2.64) with the condition of zero eigenvalues

$$\lambda(E, \mathbf{k}) = 0, \quad E = E(\mathbf{k}) . \quad (2.81)$$

Lets take the total \mathbf{k} derivative

$$\frac{d\lambda(E, \mathbf{k})}{d\mathbf{k}} = \frac{\partial\lambda(E, \mathbf{k})}{\partial E} \frac{\partial E(\mathbf{k})}{\partial \mathbf{k}} + \frac{\partial\lambda(E, \mathbf{k})}{\partial \mathbf{k}} = 0 . \quad (2.82)$$

The Fermi velocity is expressed by

$$\hbar \mathbf{v}_F(\mathbf{k}) = \frac{\partial E_k}{\partial \mathbf{k}} = - \frac{\partial\lambda(E, \mathbf{k})}{\partial \mathbf{k}} / \frac{\partial\lambda(E, \mathbf{k})}{\partial E} . \quad (2.83)$$

The energy derivative of the eigenvalues is numerically stable due to their linear dependence on the energy [68]. What has to be found is the \mathbf{k} derivative of the eigenvalues. Due to the Hellmann-Feynman theorem the derivative of an eigenvalue can be expressed by the derivative of the hermitian operator (or the corresponding matrix) with respect to the same parameter

$$\frac{\partial\lambda_s(E, \mathbf{k})}{\partial \mathbf{k}} = a_s^\dagger(\mathbf{k}) \frac{\partial M(E, \mathbf{k})}{\partial \mathbf{k}} a_s(\mathbf{k}) , \quad (2.84)$$

where s labels the considered eigenvalue and $a_s(\mathbf{k})$ is the corresponding eigenfunction. An analogous formula for a non-hermitian eigenvalue problem can be written as

$$\frac{\partial\lambda_s(E, \mathbf{k})}{\partial \mathbf{k}} = \frac{1}{(b_s(\mathbf{k}), a_s(\mathbf{k}))} b_s^\dagger(\mathbf{k}) \frac{\partial M(E, \mathbf{k})}{\partial \mathbf{k}} a_s(\mathbf{k}) , \quad (2.85)$$

where $a_s(\mathbf{k})$ and $b_s(\mathbf{k})$ are the right and left eigenvectors of the matrix M , respectively. That is

$$\begin{aligned} M(E, \mathbf{k}) a_s(\mathbf{k}) &= \lambda_s(E, \mathbf{k}) a_s(\mathbf{k}) , \\ b_s^\dagger(\mathbf{k}) M(E, \mathbf{k}) &= \lambda_s(E, \mathbf{k}) b_s^\dagger(\mathbf{k}) . \end{aligned} \quad (2.86)$$

They are normalized by $a_s^\dagger(\mathbf{k})a_s(\mathbf{k}) = b_s^\dagger(\mathbf{k})b_s(\mathbf{k}) = 1$. For the partial \mathbf{k} derivative the special properties of the KKR matrix are used. First, the \mathbf{k} dependence of the KKR matrix is given by the structural constants only (2.52). Second, this dependence comes in via the Fourier transformation of the real space structural Green function (2.47) of the screened reference system. The expression for the \mathbf{k} derivative is derived analytically and has the form

$$\frac{\partial M_{QQ'}^{\mu\mu'}(E, \mathbf{k})}{\partial \mathbf{k}} = \frac{\partial \tilde{G}_{QQ'}^{\mu\mu'}(E, \mathbf{k})}{\partial \mathbf{k}} = \sum_{n'} e^{+i\mathbf{k}\mathbf{R}^{0n'}} \tilde{G}_{QQ'}^{\mu\mu'0n'} i\mathbf{R}^{0n'}. \quad (2.87)$$

It is easy to evaluate in this form and it converges still reasonably fast with the size of the real space cluster.

The advantage of the method is the numerical stability and the independence on the number of tetrahedra in the Brillouin zone. If the iso-surface is known, no further numerical \mathbf{k} derivative is necessary. Throughout this work mainly the first method was used since quite simple Fermi surfaces (Cu and Au) were considered. I specify where the new method was applied.

2.2.4 Expectation value of the spin operator

The major goal of my work is to describe the spin Hall effect. An important property of such a discussion is the spin state of the system. Now I describe the calculation of the expectation value of the spin operator for a Bloch function.

For consistency with the used relativistic KKR method where the interaction with an effective magnetic field (2.14) is described with the operator $\hat{\beta}\hat{\Sigma} \cdot \mathbf{B}_{eff}$, we define the vector spin operator as [66]

$$\hat{\beta}\hat{\Sigma} = \begin{pmatrix} \boldsymbol{\sigma} & 0 \\ 0 & -\boldsymbol{\sigma} \end{pmatrix}, \quad (2.88)$$

with the Pauli matrices σ_x , σ_y , and σ_z . The operator does not commute with the Dirac Hamiltonian (2.14) and its expectation value is not a conserved quantity. Therefore, the spin is not a quantum number as it is the case in the non-relativistic situation. Since this approach is consistent with the description of the interaction with an effective magnetic field (see Eq. 2.14), the expectation value encodes important information about the spin state of the system.

The quantity of interest is the \mathbf{k} -dependent expectation value of the defined spin operator for the Bloch states on the Fermi surface

$$\mathbf{s}(\mathbf{k}) = \left\langle \hat{\Psi}_k \left| \hat{\beta}\hat{\Sigma} \right| \hat{\Psi}_k \right\rangle. \quad (2.89)$$

Using the KKR expansion of the wave functions (2.57) and the known properties of the Pauli matrices the z -component can be expressed as

$$\begin{aligned}
\langle \Psi_{n\mathbf{k}} | \hat{\beta} \hat{\Sigma}_z | \Psi_{n'\mathbf{k}} \rangle &= - \sum_{\kappa'\mu'} \sum_{\kappa''\mu''} a_{\kappa'\mu'}^{n*}(\mathbf{k}) a_{\kappa''\mu''}^{n'}(\mathbf{k}) \times \\
&\times \sum_{\kappa\mu} \left\{ \left(\frac{2\mu}{2\kappa+1} \right) \int g_{\kappa\mu;\kappa'\mu'}^*(r) g_{\kappa\mu;\kappa''\mu''}(r) r^2 dr + \right. \\
&+ \frac{2\mu}{2\kappa-1} \int f_{\kappa\mu;\kappa'\mu'}^*(r) f_{\kappa\mu;\kappa''\mu''}(r) r^2 dr + \\
&+ \sqrt{1 - \left(\frac{2\mu}{2\kappa+1} \right)^2} \int g_{\kappa\mu;\kappa'\mu'}^*(r) g_{-\kappa-1,\mu;\kappa''\mu''}(r) r^2 dr - \\
&\left. - \sqrt{1 - \left(\frac{2\mu}{2\kappa-1} \right)^2} \int f_{\kappa\mu;\kappa'\mu'}^*(r) f_{-\kappa+1,\mu;\kappa''\mu''}(r) r^2 dr \right\}.
\end{aligned} \tag{2.90}$$

Similar expressions can be found for the x and y component, but I leave further explanations to the section 3.2 and the Ref. [E5]. Here, it is important to comment on the non-magnetic case. Because of time inversion, Kramers degeneracy [76], and space inversion symmetry, for all considered systems the wave functions are twofold degenerate at every \mathbf{k} point. It means that any linear combination of the two solutions is again a solution of the problem. Lets label the wave functions with $\hat{\Psi}_k^1$ and $\hat{\Psi}_k^2$. They have opposite spin

$$\langle \hat{\Psi}_k^1 | \hat{\beta} \hat{\Sigma} | \hat{\Psi}_k^1 \rangle = - \langle \hat{\Psi}_k^2 | \hat{\beta} \hat{\Sigma} | \hat{\Psi}_k^2 \rangle \tag{2.91}$$

since they are related to each other by time inversion symmetry. Due to the degeneracy, the spin expectation value can point for any \mathbf{k} in arbitrary direction.

However, for the definition of spin-flip scattering and a better understanding of the microscopic processes it was useful to consider a selected axis for all \mathbf{k} points.

The idea is simple: Let us apply a unitary transformation

$$|\Psi_{\mathbf{k}}^3\rangle = c_1 |\Psi_{\mathbf{k}}^1\rangle + c_2 |\Psi_{\mathbf{k}}^2\rangle, \tag{2.92}$$

$$|\Psi_{\mathbf{k}}^4\rangle = -c_2^* |\Psi_{\mathbf{k}}^1\rangle + c_1^* |\Psi_{\mathbf{k}}^2\rangle,$$

$$1 = |c_1|^2 + |c_2|^2$$

to the degenerate subset at every \mathbf{k} point to fulfill the condition

$$\langle \Psi_{\mathbf{k}}^3 | \hat{\beta} \hat{\Sigma}_x | \Psi_{\mathbf{k}}^3 \rangle = \langle \Psi_{\mathbf{k}}^3 | \hat{\beta} \hat{\Sigma}_y | \Psi_{\mathbf{k}}^3 \rangle = 0, \tag{2.93}$$

$$\langle \Psi_{\mathbf{k}}^4 | \hat{\beta} \hat{\Sigma}_x | \Psi_{\mathbf{k}}^4 \rangle = \langle \Psi_{\mathbf{k}}^4 | \hat{\beta} \hat{\Sigma}_y | \Psi_{\mathbf{k}}^4 \rangle = 0.$$

Such a transformation can be defined at every \mathbf{k} point. The details are discussed in chapter 3.2 and Ref. [E5]. The wave function with the spin expectation value parallel to z is labeled further on with $\hat{\Psi}_k^+$ and the other with $\hat{\Psi}_k^-$.

2.3 Spin relaxation

In this section the calculation of the spin relaxation time and the spin diffusion length is introduced. At the beginning the basic mechanisms of spin relaxation is shortly reviewed. In the following the used method and the most important expressions in terms of the KKR expansion (2.57) are presented.

In the literature usually three distinct mechanisms of spin relaxation are discussed [16, 77, 78]. Those are the Elliott-Yafet [79, 80], the D'yakonov-Perel' [3], and the Bir-Aronov-Pikus mechanism [81]. The last one describes electron-hole interactions in semiconductors and is irrelevant for metallic systems. The same holds for the D'yakonov-Perel' mechanism. In this case the spin relaxation is induced by band splittings in systems with a lack of inversion symmetry. Since all considered systems have inversion symmetry, the only remaining mechanism is the spin relaxation according to Elliott and Yafet.

It describes the spin-flip process at perturbations of the ideal lattice. For every momentum scattering event the possibility exists that the spin flip occurs additionally. The perturbations leading to momentum and spin-flip scattering are impurities, grain boundaries, surfaces, and phonons. Whereas phonons are important for high temperatures, the scattering at impurities dominates at low temperatures. Here all calculations are performed at $T = 0$ which leads to the impurity induced Elliott-Yafet spin relaxation as the only remaining process.

The spin relaxation time

I restrict the consideration to metallic non-magnetic systems with space inversion symmetry where the spin relaxation is induced by spin-flip processes at impurities. These systems have degenerate bands even in the relativistic case, including spin-orbit coupling. Since time inversion is present the systems show Kramers degeneracy [76] ($E_{\mathbf{k}}^+ = E_{-\mathbf{k}}^-$). In combination with space inversion symmetry all \mathbf{k} states are two-fold degenerate ($E_{\mathbf{k}}^+ = E_{\mathbf{k}}^-$). The wave functions of every doublet have opposite spin direction. To have one axis for every \mathbf{k} point, we apply the transformation sketched in section 2.2.4. According to this axis (usually the z axis is used) we label the states of the doublet with "+" and "-", respectively.

With time dependent perturbation theory [82, 83] the \mathbf{k} -dependent spin-flip scattering time τ_k^{sf} can be connected to the scattering rate and the corresponding \hat{T} matrix via

$$\frac{1}{\tau_k^{sf}} = \sum_{k'} P_{kk'}^{+-} = \frac{2\pi}{\hbar} \sum_{k'} |T_{\mathbf{k}\mathbf{k}'}^{+-}|^2 \delta(E_{\mathbf{k}}^+ - E_{\mathbf{k}'}^-). \quad (2.94)$$

The elements of the transition matrix are defined as

$$T_{\mathbf{k}\mathbf{k}'}^{+-} = \frac{1}{V} \sum_{n,\mu} \int d^3r \left(\Psi_{\mathbf{k}'}^-(\mathbf{r}) \right)^\dagger \Delta V^{n,\mu}(r) \Psi_{\mathbf{k}}^+(\mathbf{r}). \quad (2.95)$$

Using the expansion of the perturbed and unperturbed wave functions into the single site scattering solutions (2.57 and 2.73) the expression simplifies to

$$T_{\mathbf{k}\mathbf{k}'}^{+-} = \frac{1}{V} \sum_{n,\mu,Q} (\hat{c}_Q^-(\mathbf{k}'))^* \Delta_Q^{n,\mu} c_Q^+(\mathbf{k}). \quad (2.96)$$

The $\Delta_Q^{n,\mu}$ matrix is a radial integral over the perturbed potential and the perturbed and unperturbed radial solutions. It is integrated numerically

$$\Delta_Q^{n,\mu} = \int_0^{R_{\mu,ASA}^n} dr r^2 \left(\overset{\circ}{R}_Q^{n,\mu}(r) \right)^* \Delta V^{n,\mu}(r) R_Q^{n,\mu}(r). \quad (2.97)$$

With the expression of the perturbed expansion coefficients via the unperturbed one (2.74) the transition matrix is expressed by

$$T_{\mathbf{k}\mathbf{k}'}^{+-} = \frac{1}{V} \sum_{n,\mu,Q} (\overset{\circ}{c}_Q^-(\mathbf{k}'))^* \Delta_Q^{n,\mu} D_{QQ'}^{nn',\mu\mu'} \overset{\circ}{c}_Q^+(\mathbf{k}'). \quad (2.98)$$

If the \mathbf{k} -dependent spin-flip scattering time is known, the Fermi surface average is taken by

$$\frac{1}{\tau_{sf}} = \frac{V}{(2\pi)^3} \sum_n \iint_{E_k=E_F} \frac{dS_n}{|\mathbf{v}_k|} \frac{1}{\tau_k^{sf}} \quad (2.99)$$

to find the spin-flip scattering time, comparable to experiments, for instance, conduction electron spin resonance (CESR).

The spin diffusion length

Usually, in non-local measurements not the spin relaxation time is extracted but the spin diffusion length. The distance between spin-current injector and collector is varied and the non-local signal is taken as a function of the distance. The spin diffusion length is extracted by exponential model equations fitted to the experimental curve. The equations are usually based on spin-dependent Boltzmann and diffusion equations. In this respect the model of Valet and Fert [24] is well known.

To connect the spin diffusion length with the calculated spin relaxation time, the widely used expression of Valet and Fert [24]

$$l_{sf} = \sqrt{\frac{\lambda \lambda_{sf}}{6}} \quad (2.100)$$

can be exploited. Here the momentum mean free path $\lambda = \tau v_F$ and the spin-flip length $\lambda_{sf} = \tau_{sf} v_F$ are determined by the momentum relaxation time τ and the spin-flip scattering time τ_{sf} , respectively. The Fermi velocity is a quantity depending on the host system only. However, to make the comparison to experiments easier another formula [E8, 84]

$$l_{sf} = \frac{\pi}{2k_F^2} \sqrt{\frac{3}{2}} \frac{\hbar}{e^2} \sqrt{\frac{\tau_{sf}}{\tau}} \sigma_{xx} \quad (2.101)$$

is used here to estimate the spin diffusion length. In a free-electron model both equations are equivalent. I present the proof in the attachment E. The momentum relaxation time τ , the spin-flip scattering time τ_{sf} , the longitudinal charge conductivity σ_{xx} (see section 2.4), and the Fermi surface averaged wave vector k_F are calculated from our *ab initio* method. The resulting spin diffusion length is obtained with only one free parameter, the impurity concentration.

2.4 Electronic transport

In this part the method of calculating the electronic transport is described. I decided to use the Boltzmann approach for charge and spin transport. This has two reasons. First of all, this method gives a good insight into the microscopic origin of different effects which are sometimes hidden in more sophisticated methods such as solving a Kubo formula. In addition, the Boltzmann approach is well suited to deal with dilute alloys where the extrinsic spin Hall effect is dominant. Furthermore, it is possible to prepare such alloys experimentally in a well defined way. It was shown that numerical calculations of the residual charge conductivity are in good agreement with experimental results [85, 86].

In the first part, the general form of the linearized Boltzmann equation and the expression for the scattering term within the KKR method is discussed. In the following the expressions for the charge and spin conductivities are introduced.

2.4.1 Linearized Boltzmann equation

The starting point is the linearized Boltzmann equation (1.11) for a homogeneous system [35, 44, 45]

$$\dot{\mathbf{k}} \frac{\partial f_{\mathbf{k}}^{eq}}{\partial \mathbf{k}} = \sum_{\mathbf{k}'} (P_{\mathbf{k}'\mathbf{k}} g_{\mathbf{k}'} - P_{\mathbf{k}\mathbf{k}'} g_{\mathbf{k}}) ,$$

which is widely used in the literature. It is an equation for the effective one-electron distribution function $f_{\mathbf{k}} = f_{\mathbf{k}}^{eq} + g_{\mathbf{k}}$ separated in an equilibrium $f_{\mathbf{k}}^{eq}$ and a non-equilibrium part $g_{\mathbf{k}}$ linear in the applied external fields. The equilibrium distribution function for electrons is the Fermi-Dirac distribution $f_{\mathbf{k}}^{eq} = (e^{(E_{\mathbf{k}} - E_F)/k_b T} + 1)^{-1}$. The \mathbf{k} derivative at $T=0$ is proportional to the Fermi velocity \mathbf{v}_F and a δ -function at E_F . The perturbed distribution function in linear response is given by

$$g_{\mathbf{k}} = e \left(\frac{\partial f_{\mathbf{k}}^{eq}}{\partial E_{\mathbf{k}}} \right) \Lambda_{\mathbf{k}} \mathbf{E} \quad (2.102)$$

and is at zero temperature also restricted to the Fermi surface. Combining both and using the semiclassical expression for the force term

$$\dot{\mathbf{k}} = -\frac{e}{\hbar} \mathbf{E} , \quad (2.103)$$

the linearized Boltzmann equation is transformed into

$$\Lambda^{\nu}(\mathbf{k}) = \tau_{\mathbf{k}}^{\nu} \left[\mathbf{v}_{\mathbf{k}}^{\nu} + \sum_{\mathbf{k}'\nu'} P_{\mathbf{k}'\mathbf{k}}^{\nu'\nu} \Lambda^{\nu'}(\mathbf{k}') \right] . \quad (2.104)$$

Here ν is the number of bands available at the Fermi level. The anisotropic relaxation time $\tau_{\mathbf{k}}^{\nu}$ is calculated as the integral over all outgoing states of the transition rate

$$(\tau_{\mathbf{k}}^{\nu})^{-1} = \sum_{\mathbf{k}'\nu'} P_{\mathbf{k}\mathbf{k}'}^{\nu\nu'} . \quad (2.105)$$

The Fermi velocity

$$\mathbf{v}_{\mathbf{k}}^{\nu} = \frac{1}{\hbar} \frac{\partial E_{\mathbf{k}}^{\nu}}{\partial \mathbf{k}} , \quad (2.106)$$

describes the dispersion of the bands in the unperturbed crystal. Furthermore, the scattering-in term $\sum_{\mathbf{k}'\nu'} P_{\mathbf{k}'\mathbf{k}}^{\nu'\nu} \Lambda^{\nu'}(\mathbf{k}')$ turns out to be essential for the description of the spin Hall effect [E7]. It was shown by Butler [87] that the scattering-in term in the Boltzmann approach is equivalent to the vertex corrections caused by impurities in the dilute limit of the Kubo formula. This was confirmed by a comparison of the spin Hall effect calculated in our approach to the solution of a Kubo-Streda formula [88] for dilute alloys described by the coherent-potential approximation [89] (see Appendix D). The anisotropic relaxation time includes the spin-conserving and spin-flipping contributions. This is evident considering, for example Cu, with only two degenerate bands at the Fermi level. Those are labeled according to their spin expectation value by ”+” and ”-”, respectively (see section 2.2.4). Thus, the anisotropic relaxation time is

$$\frac{1}{\tau_{\mathbf{k}}^+} = \frac{1}{\tau_{\mathbf{k}}^{++}} + \frac{1}{\tau_{\mathbf{k}}^{+-}} \quad \text{and} \quad \frac{1}{\tau_{\mathbf{k}}^-} = \frac{1}{\tau_{\mathbf{k}}^{-+}} + \frac{1}{\tau_{\mathbf{k}}^{--}} , \quad (2.107)$$

where clearly spin-conserving τ^{++} and τ^{--} , as well as, spin-flip contributions τ^{+-} and τ^{-+} are included. The same holds for the mean free path. Therefore, the spin relaxation process according to Elliott and Yafet [79] is fully taken into account [E7]. The important quantity is the scattering rate $P_{\mathbf{k}\mathbf{k}'}^{\nu\nu'}$ which is connected to the transition matrix by Fermi’s golden rule (see Eq. 1.25)

$$P_{\mathbf{k}\mathbf{k}'}^{\nu\nu'} = \frac{2\pi}{\hbar} c_0 N \left| T_{\mathbf{k}\mathbf{k}'}^{\nu\nu'} \right|^2 \delta(E_{\mathbf{k}} - E_{\mathbf{k}'}) .$$

Here we assumed a dilute alloy with $c_0 N$ as the number of non-interacting impurity atoms. Following section 2.3 the transition matrix for non-magnetic systems is given by

$$T_{\mathbf{k}\mathbf{k}'}^{+-} = \frac{1}{V} \sum_{n,\mu,Q} \left[(\tilde{c}_Q^{n\mu}(\mathbf{k}'))^* \right]^- \Delta_Q^{n,\mu} D_{QQ'}^{nn',\mu\mu'} \left[\tilde{c}_{Q'}^{n'\mu'}(\mathbf{k}') \right]^+ , \quad (2.108)$$

where the same definitions for $\Delta_Q^{n,\mu}$ and $D_{QQ'}^{nn',\mu\mu'}$ are used (see Eqs. (2.97) and (2.74)). Finally the integral equation (2.104) is solved iteratively including the scattering-in term. This method was used and explained by several authors [69, 86, 90–92].

2.4.2 Charge conductivity and spin transport

After solving the linearized Boltzmann equation (2.104) the next step is to calculate the charge and conductivity tensors. As introduced already in chapter 1.3 the charge current density is expressed by a Fermi surface integral over the distribution function and the Fermi velocity (1.9). Using the expression for the distribution function (1.10) and the Ansatz for the non-equilibrium part (2.102) the charge current is expressed by

$$\mathbf{J} = -e^2 \sum_{\mathbf{k}} \left(\frac{\partial f_{\mathbf{k}}^{eq}}{\partial E_{\mathbf{k}}} \right)_{T=0} \mathbf{v}_{\mathbf{k}} \circ \Lambda_{\mathbf{k}} \mathbf{E} . \quad (2.109)$$

The symbol \circ stands for the tensor product. A comparison to Ohm’s law yields an expression for the conductivity tensor

$$\underline{\sigma} = \frac{e^2}{\hbar} \sum_{\nu} \frac{1}{(2\pi)^3} \iint_{E_{\mathbf{k}}=E_F} \frac{dS_{\nu}}{|\mathbf{v}_{\mathbf{k}}^{\nu}|} \mathbf{v}_{\mathbf{k}}^{\nu} \circ \Lambda_{\mathbf{k}}^{\nu} = \underline{\sigma}^+ + \underline{\sigma}^- . \quad (2.110)$$

The semiclassical expression for the spin conductivity is similar

$$\underline{\sigma}_z^s = \frac{e^2}{\hbar} \sum_{\nu} \frac{1}{(2\pi)^3} \iint_{E_{\mathbf{k}}=E_F} \frac{dS_{\nu}}{|\mathbf{v}_{\mathbf{k}}^{\nu}|} s_z^{\nu}(\mathbf{k}) \mathbf{v}_{\mathbf{k}}^{\nu} \circ \boldsymbol{\Lambda}_{\mathbf{k}}^{\nu} . \quad (2.111)$$

In addition, the spin expectation value of the wave functions $s_z^{\nu}(\mathbf{k})$ is included. Here, I used already the fact that the spin expectation values along x and y direction are zero (see section 2.2.4). In the non-relativistic limit, without spin-orbit coupling, the expression simplifies to ($s_z^+ = -s_z^- = 1$)

$$\underline{\sigma}^s = \frac{e^2}{\hbar} \frac{1}{(2\pi)^3} \iint_{E_{\mathbf{k}}=E_F} \frac{dS}{|\mathbf{v}_{\mathbf{k}}|} \mathbf{v}_{\mathbf{k}} \circ (\boldsymbol{\Lambda}_{\mathbf{k}}^+ - \boldsymbol{\Lambda}_{\mathbf{k}}^-) = \underline{\sigma}^+ - \underline{\sigma}^- \quad (2.112)$$

with the assumption of only one degenerate band at the Fermi level. It is nothing else but the two-current model introduced in section 1.1.

Chapter 3

Results

This chapter summarizes the results of the present work. It is a cumulative thesis which means that after an extended summary the published articles are included. The following pages are used to present the most important results of all considered publications extended by additional explanations.

The idea of my work was a description of the microscopic mechanism of skew scattering in order to contribute to the general understanding of the spin Hall effect. Furthermore, materials showing a strong spin Hall effect in combination with a long spin diffusion length should be identified. These materials are important for any application of the spin Hall effect in spin current generating techniques.

Since we had already some experience in describing the spin relaxation time due to the

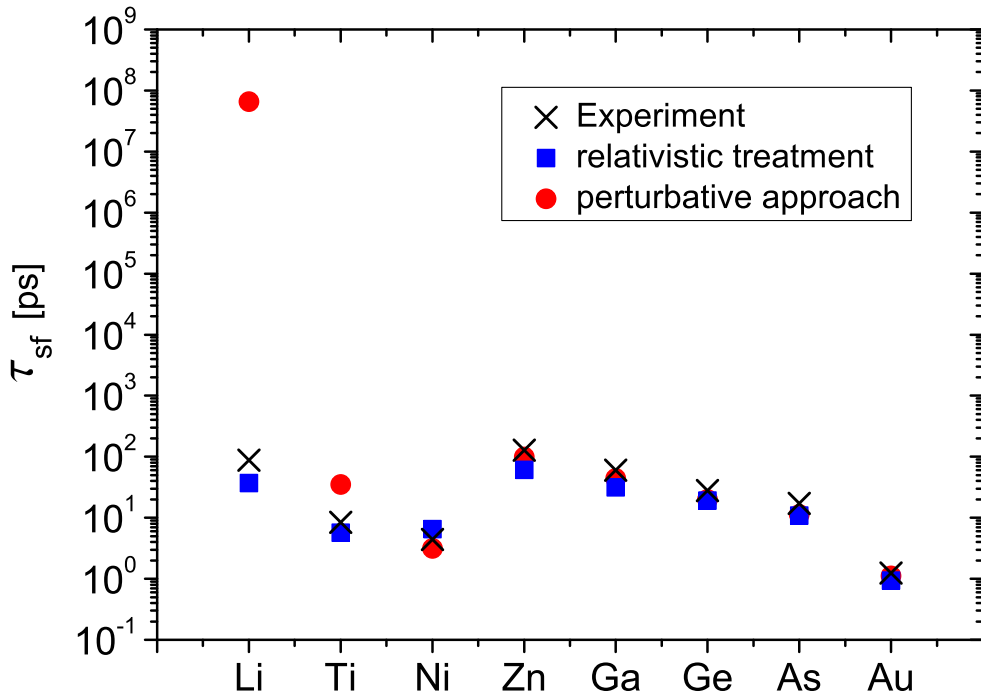


Figure 3.1: Spin-flip scattering time for different impurities in Cu. The perturbative approach [E4] (Sec. 3.1) and the fully relativistic treatment in comparison to the experimental data [93]. Considering the spin-orbit coupling at the impurity site only fails for light impurities in a heavier host completely. Whereas the fully relativistic description works well.

Elliott-Yafet mechanism [E4], it was quite natural to start with a proper description of this mechanism in a fully relativistic treatment. In a first attempt, a perturbative description of the spin-orbit interaction at the impurity site was used [E4]. It turned out that impurities showing comparable spin-orbit coupling to the host atoms were well described. The description of spin-flip processes for light impurities failed completely. In the following, the approach introduced in section 2.3 was applied [E6] to the description of the scattering process. In Fig. 3.1 the results for the perturbative and the fully relativistic description in a Cu host in comparison to conduction spin electron resonance (CESR) experiments are shown. For impurities with a comparable atomic number to Cu both approaches work well, whereas the perturbative approach fails completely for Li. This very light impurity exhibits vanishing spin-orbit interaction and the relaxation mechanism is driven by the spin-orbit coupling of the host.

For a microscopic understanding of this effect two properties of the unperturbed Bloch functions must be analyzed. Those are the angular momentum decomposition and the spin-mixing character of the wave function. In the KKR method, the Bloch functions are expanded into complex spherical harmonics (2.57). If the wave function is normalized to one the angular momentum character is just the fraction of the coefficients with a certain l [94]. The spin-mixing character of the wave functions is discussed using the expectation value of the spin operator Σ [E5] (see section 2.2.4). Due to the twofold degeneracy of the wavefunctions in a non-magnetic host with inversion symmetry, any linear combination is again a solution at a given \mathbf{k} point. From this it follows that any direction of the spin expectation value can be chosen. For simplicity we choose the z direction for all \mathbf{k} points and apply the unitary transformation explained in section 2.2.4 [E5]. After the transformation the $\hat{\beta}\hat{\Sigma}_z$ operator is of interest. In Fig. 3.2 the corresponding expectation value for three metals, the same as used for the further calculations, is presented. I always show both degenerate bands with opposite spin polarization to make clear that no net magnetization is in the system. In the non-relativistic case (without spin-orbit coupling) the spin expectation values for the two bands would be $+1$ or -1 , respectively. In that case spin is a good quantum number and the language of "spin-up" and "spin-down" states can be used. Including spin-orbit interaction yields a reduction of this value which is a measure of the spin mixing of the wave functions. They are not pure "spin-up" or "spin-down" states anymore.

Two main contributions influence the strength of the spin mixing. One is the atomic number which enters the spin-orbit coupling term. The other mechanism is the presence of several bands close to each other. In this case the spin-orbit interaction can lead to a significant spin mixing which can be understood in a two-level perturbation model [E5, 77].

Both effects can be well seen in the presented spin polarization of Fig. 3.2. Starting with Cu (3.2 a) the spin mixing is very small and the non-relativistic value (± 1) is nearly restored. The next system is Au (3.2 b) with a similar electronic structure but with a much larger atomic number. The spin mixing is strongly increased. However, it is still smaller than 10%. Going to Pt (3.2 c) the spin mixing reaches 100% ($s_z(\mathbf{k}) = 0$) at some \mathbf{k} points. This is not induced by the atomic number which is even smaller than for Au but by the mixing of several bands close to the Fermi level. Only the degenerate 9th ($s_z(\mathbf{k}) < 0$) and 10th ($s_z(\mathbf{k}) > 0$) from several bands at the Fermi level are shown. A more detailed discussion was given in Ref. [E5].

These results can be used to understand the \mathbf{k} -dependent spin-flip scattering time as presented in Fig. 3.3. As an example, a Ga impurity in a Cu host is used. It is nec-

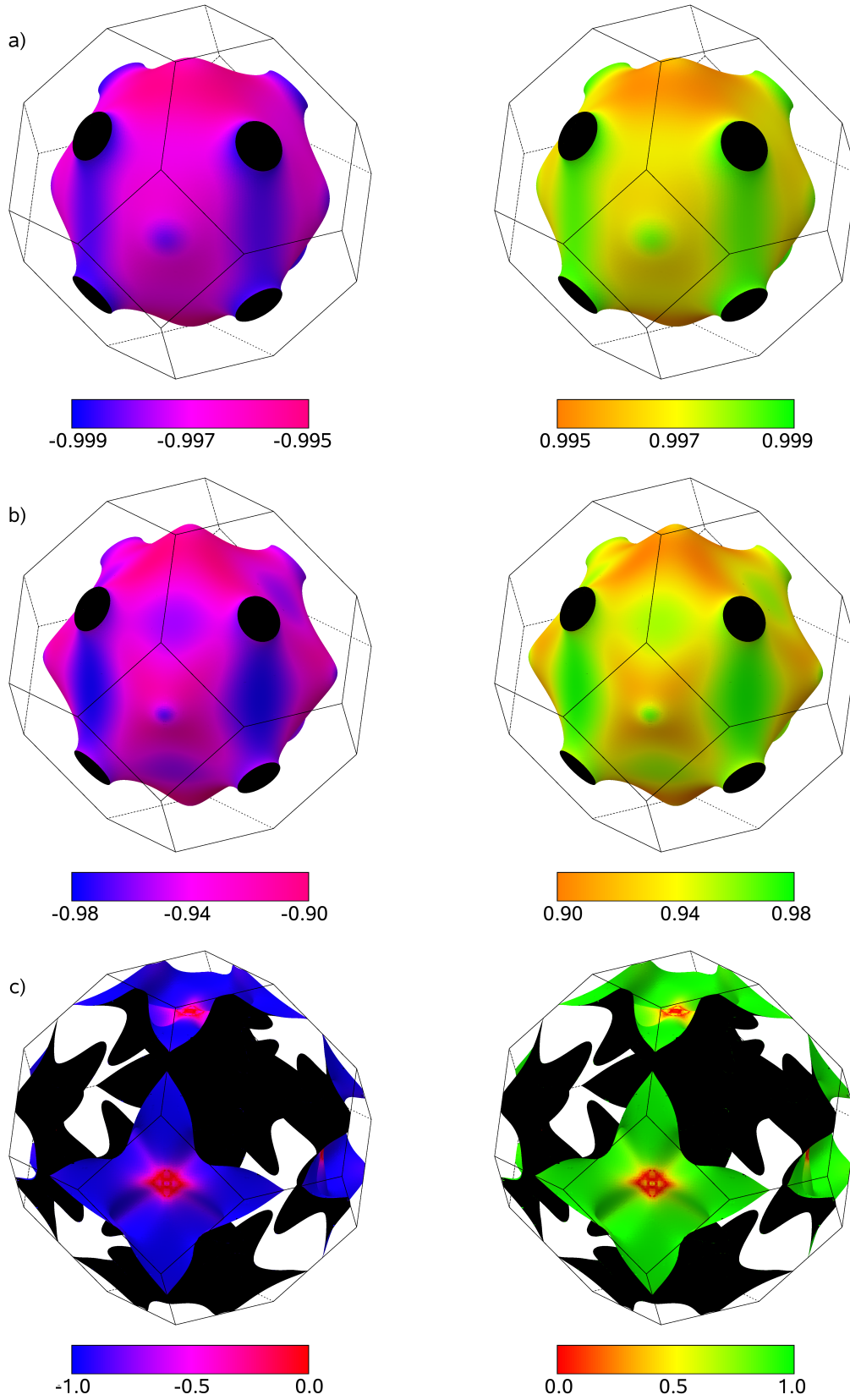


Figure 3.2: The spin expectation value $\langle \hat{\beta} \hat{\Sigma}_z \rangle$ for the two degenerate bands in a non-magnetic material for a) Cu, b) Au and c) Pt (the 9th and 10th bands). Increasing the atomic number leads to stronger mixing (Cu \rightarrow Au). Spin-orbit driven avoided crossings enhances the spin mixing drastically (Au \rightarrow Pt)

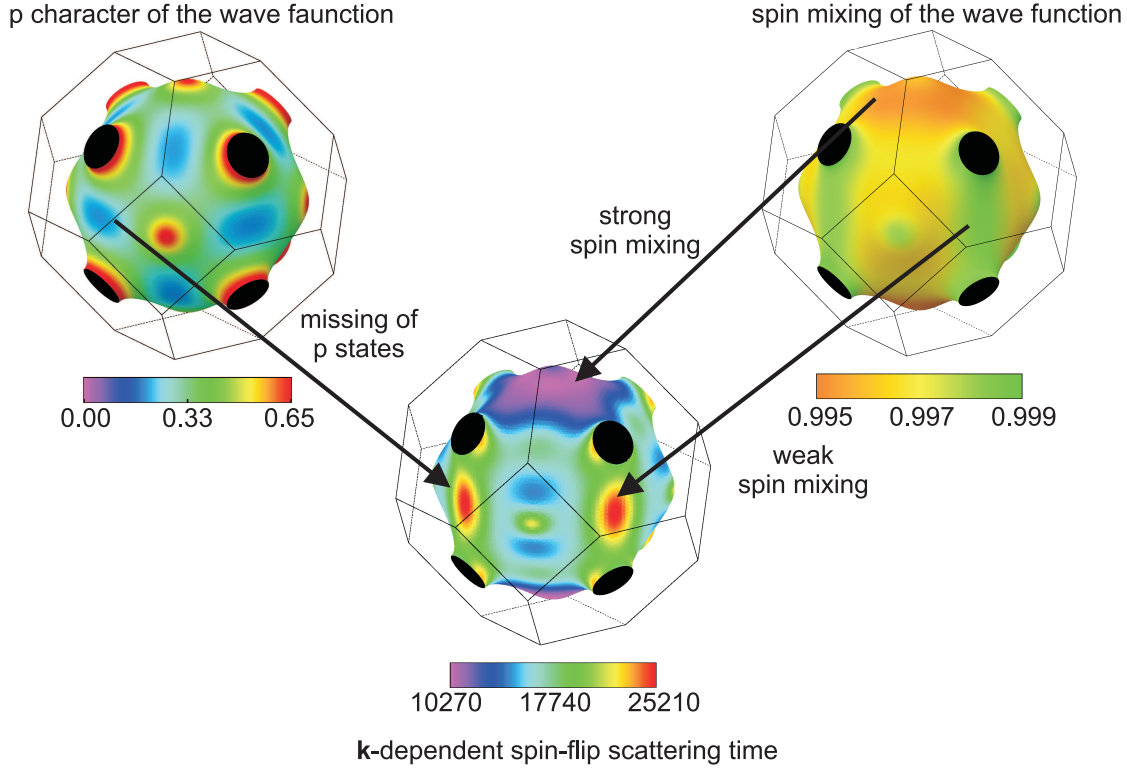


Figure 3.3: The \mathbf{k} -dependent spin-flip scattering time ($\tau_{\mathbf{k}}^{sf}$ middle) can be understood using the l decomposition (left figure) and spin-mixing character (right figure) of the Bloch functions of the ideal crystal. The example is a Ga impurity in a Cu host.

essary to mention that Ga is an sp scatterer. Since the effective spin-orbit interaction of s states is zero, mainly p electrons contribute to the spin-flip scattering time. It is obvious that the anisotropic spin-flip scattering time has the same reduced symmetry in comparison with the non-relativistic case as the spin expectation value. The relativistic symmetry is present with only 8 operations instead of 48 non-relativistic symmetry operations of the cubic lattice (see Appendix F). The red regions with long scattering times (in the middle picture), i.e. weak scattering, are clearly connected to regions on the Fermi surface with a lack of p electrons in a Cu host. In addition, the spin mixing for these regions is smallest which points to the reduced effective spin-orbit coupling of these \mathbf{k} states. The regions with strongest scattering (purple) are related to strong spin mixing of the host wave functions. Such a consideration can be used for any combination of host and impurity atoms to understand the microscopic origin of the scattering rates [E6] (see Sec. 3.3).

After the discussion of the spin-flip scattering time we move our attention to the charge and spin transport of the considered systems as discussed in Ref. [E7] (see Sec. 3.4). The charge conductivity is calculated by using an iterative solution of the linearized Boltzmann equation (Sec. 2.4.1). This method is not new and was already applied by our group to several systems [85, 86, 92, 95]. I extended the method to relativistic wave functions in the scattering term. To convince the reader of the quality of the method experimental results of the residual longitudinal conductivity of dilute alloys are shown in comparison with the calculated values in Fig. 3.4. The agreement is very good for all shown systems.

The next step is the calculation and the understanding of the skew scattering mecha-

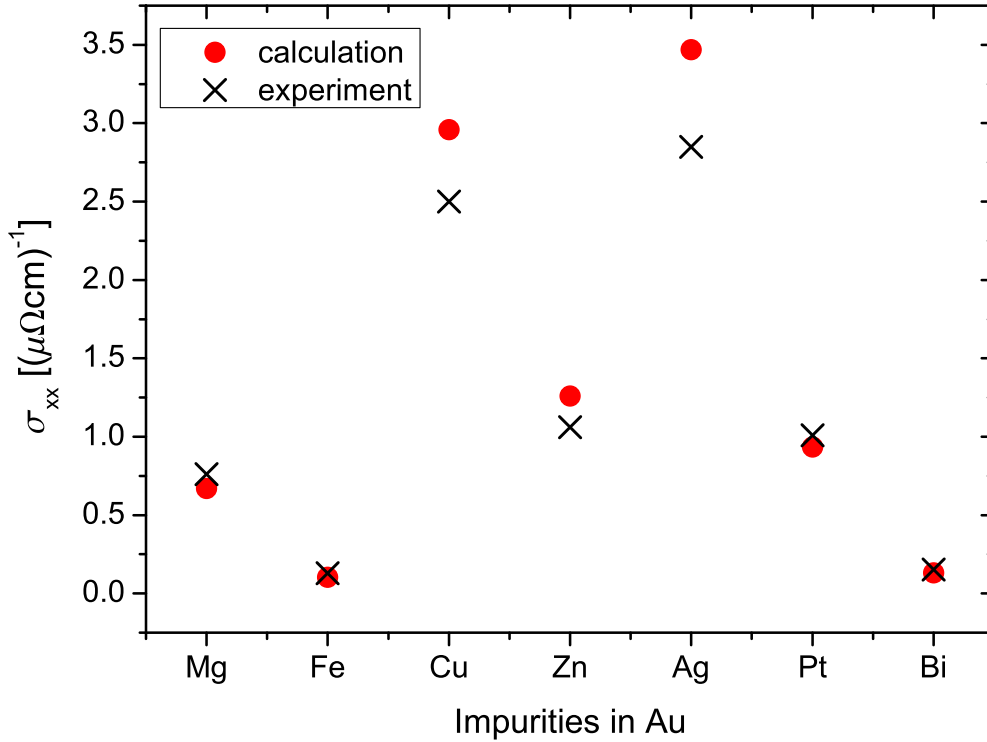


Figure 3.4: Longitudinal conductivities σ_{xx} for different impurities in Au with an impurity concentration of 1 at.% in comparison to experimental results [93]

nism. Some values for the spin Hall angle α in Cu and Au hosts are shown in Fig. 3.5. The first obvious result is the strong variation of the spin Hall angle on the impurity atom. For both hosts, Cu and Au, values up to nearly 0.1 are obtained even for light impurities such as C in Au. A sign change for selected impurity-host combinations is as well present.

Let us try to explain the experimentally found spin Hall angles (see Tab. 1.1) by our calculations. The most interesting result is the possible explanation of the gigantic spin Hall effect in Au (Seki et al. [11]) by light contaminations such as C and N. Moreover, the variation of the Au results [22, 23] can be explained by the existence of other impurities in Au as for instance Ag.

In the following it is necessary to explain the obtained results and to give a better understanding of the microscopic mechanism of the SHE. First, a microscopic picture of the skew scattering will be given. According to the discussion of section 1.3, the skew scattering mechanism is the asymmetric scattering of "spin-up" and "spin-down" electrons due to the spin-orbit interaction and a perturbing potential. In our relativistic language, introduced in section 2.2.4, it is the asymmetric scattering of "+" and "-" states.

For an illustration, the difference of the scattering rates $P_{\mathbf{k}_0\mathbf{k}'}^{++} - P_{\mathbf{k}_0\mathbf{k}'}^{--}$ for a fixed incoming Bloch state is shown in Fig. 3.6. The incoming direction is along x axis and the examples are Li (a), Zn (b) and Au (c) impurities in a Cu host. It is obvious that in the case of Li "+" states are mainly scattered in y direction and "-" states in $-y$ direction. The result for Zn is opposite. The corresponding sign change is seen in Fig. 3.5. Such a simple picture is nice for an easy understanding but in general the situation is much more complicated. In Fig. 3.6 c) the skew scattering effect for a Au impurity in Cu is shown. From a first view, it looks like for Zn, however, it turns out that the spin

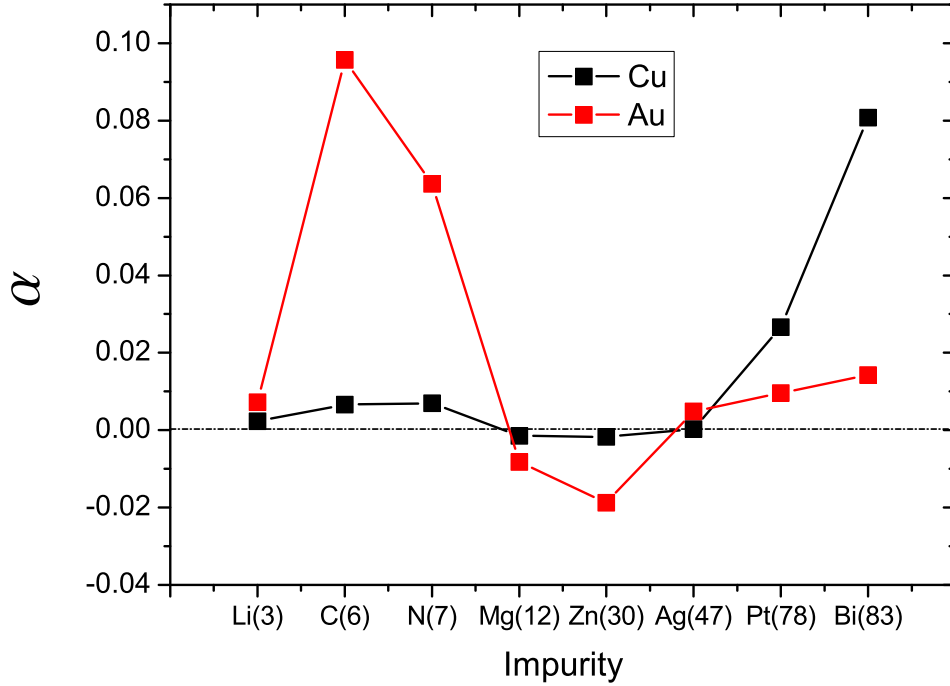


Figure 3.5: The calculated spin Hall angle for different impurities (with the atomic number in brackets) in a Cu and a Au host.

Hall conductivity has the same sign as for Li [E8] (see Sec. 3.5). Considering the effect in Fig. 3.6 c) in detail, it turns out that a strong back scattering contribution occurs, where the sign of the skew scattering is opposite to the forward scattering part. This example should illustrate that the strong \mathbf{k} dependence of the scattering mechanism makes it difficult to find a simple explanation for the actual sign of the spin Hall effect. So far a real calculation is required and no general argument can be found. For an explanation of the strongly varying values for the Hall angle in different sys-

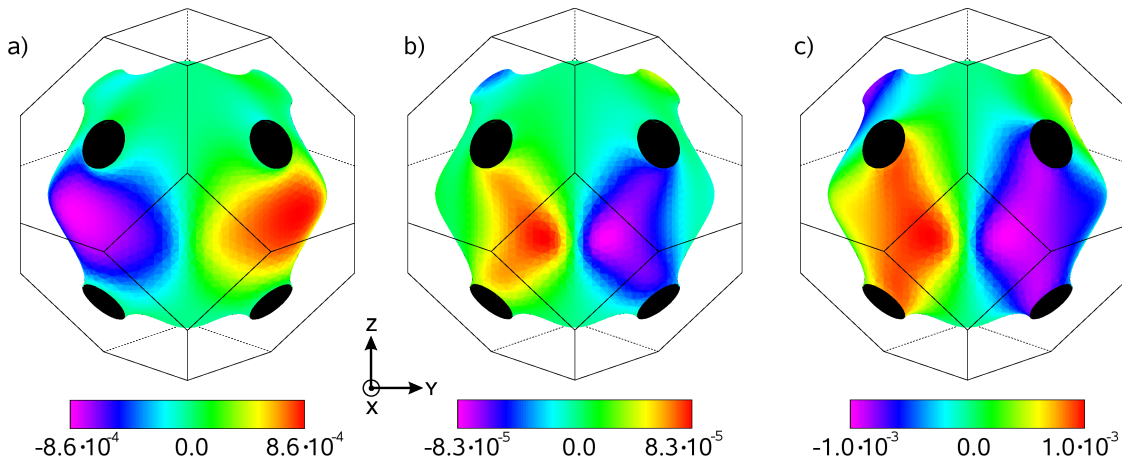


Figure 3.6: The microscopic picture of the skew scattering mechanism. The difference of the scattering rates $P_{\mathbf{k}\mathbf{k}'}^{++} - P_{\mathbf{k}\mathbf{k}'}^{--}$ for "+" and "-" states for a) Li, b) Zn, and c) Au impurities in Cu.

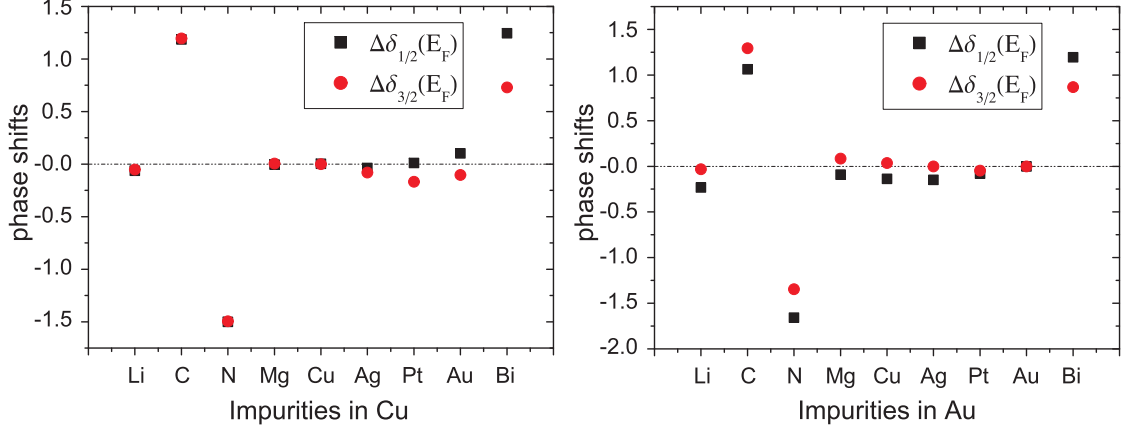


Figure 3.7: The differences between the scattering phase shifts of an impurity and the host atom for the levels $j = 1/2$ and $j = 3/2$ ($l = 1$) in Cu and Au.

tems the scattering phase shifts δ_j of the impurity and host atoms can be used [E8] (see Sec. 3.5). For Cu and Au hosts the differences of the scattering phase shifts $\Delta\delta_j = \delta_j^{impurity} - \delta_j^{host}$ are shown in Fig. 3.7. Here we consider the total angular momentum $j = l + 1/2$ and $j = l - 1/2$ for p electrons ($l = 1$) only. This is valid because all considered atoms (except for Pt) are mainly s and p scatterers, and the spin-orbit coupling for s electrons is zero. From Fig. 3.7 it is obvious that only C, N, and Bi are strong p scatterers with large phase shifts. In all other cases the p scattering is weak. Furthermore, the splitting of the $j = 1/2$ and $j = 3/2$ levels indicates the strength of the effective spin-orbit coupling. Since the spin-orbit interaction is responsible for the SHE, systems with a large asymmetry between $\Delta\delta_{1/2}$ and $\Delta\delta_{3/2}$ phase shifts can exhibit a large spin Hall angle. This asymmetry behaves differently for Cu and Au hosts. Whereas for Cu the Bi impurity induces the largest asymmetry, in Au it is maximal for the light elements C and N. The reason for that is the different spin-orbit coupling of the hosts. The displayed phase shifts are the difference between the host and impurity atoms. Thus, the asymmetry is a measurement of the difference in the spin-orbit couplings between the host and the impurity atom. For a Cu host it is quite weak and the spin-orbit interaction is mostly induced by the impurity atom. For Au this is different since the spin-orbit coupling of p electrons in Au, Pt, and Bi is similar due to their comparable atomic numbers. That leads to a reduction of the asymmetry for Pt and Bi and to a strong increase for light impurities such as Li, C, and N. Combining the strong p scattering and the large asymmetry induced for Bi in Cu and for the light impurities in Au the Hall angles of Fig. 3.5 can be explained.

In the last part I show that the spin Hall angle is tunable by the type of impurity atoms [E7]. For experiments and applications the spin diffusion length is equally important [E8] (see Sec. 3.5). All ingredients are available to use the formula introduced in section 2.3 for calculation of the spin diffusion length. The only free parameter is the impurity concentration. For a comparison to experimental results the longitudinal charge conductivity measured in non-local Hall devices [21, 22, 27] is used. From this the impurity concentrations c_{exp} are estimated assuming only one type of impurity atom to occur in the sample

$$c_{exp} = \frac{\sigma_{xx}^{calc}}{\sigma_{xx}^{exp}} c_0. \quad (3.1)$$

For applications systems with large Hall angles in combination with long spin diffusion lengths are of interest, therefore both quantities are shown in Fig. 3.8 for all considered materials. I can clearly identify three systems with the desired properties. Those are

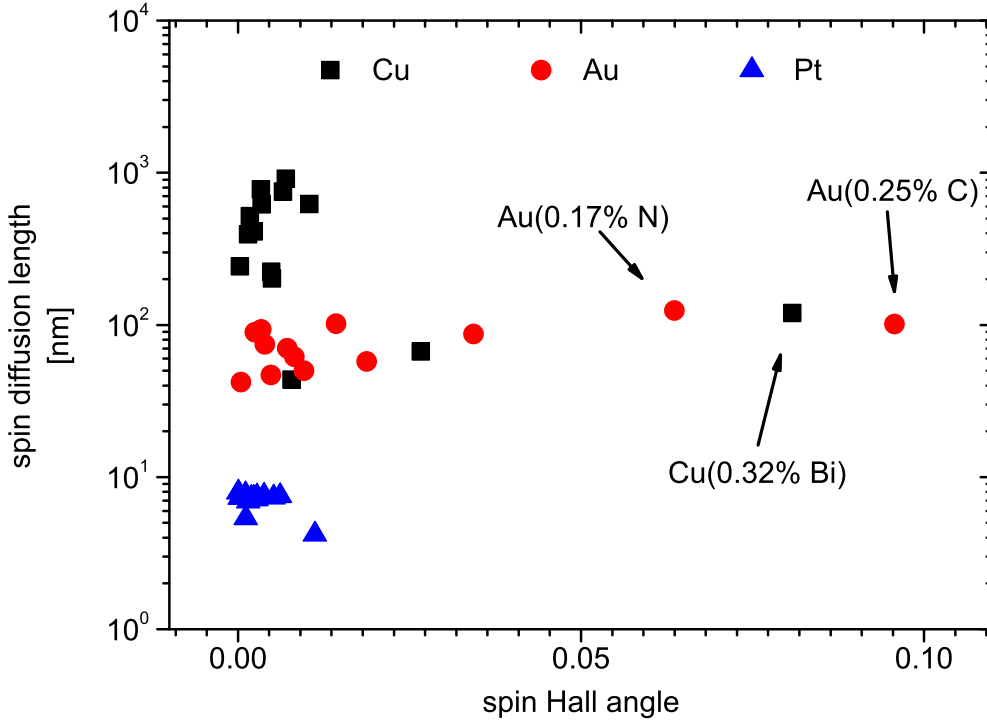


Figure 3.8: The spin diffusion length l_{sf} versus the spin Hall angle α for a fixed longitudinal conductivity ($\sigma_{xx}(Cu) = 0.7 (\mu\Omega cm)^{-1}$ [27], $\sigma_{xx}(Au) = 0.48 (\mu\Omega cm)^{-1}$ [22], and $\sigma_{xx}(Pt) = 0.08 (\mu\Omega cm)^{-1}$ [21]).

the C and N impurities in Au and Bi impurities in Cu. The required concentrations to reproduce the measured longitudinal conductivities are reasonable with respect to the dilute limit, which means the approach I used is valid. The spin diffusion length for all three systems is of the order of 100 nm which is long enough for any nanoelectronic application. The Hall angle is larger than 0.06 which is comparable to the largest value measured so far [11].

The results for Pt based alloys are not very promising. In these systems the spin-orbit coupling of the Pt host plays the dominant role and the spin diffusion length as well as the spin Hall angle are nearly unaffected by the impurity type. In addition, both quantities are small, the spin diffusion length being not longer than 10 nm. From that point of view, Pt is not a very promising material for applications taking advantage of the spin Hall effect. One should rather use Cu. In a Cu host the spin diffusion length is tunable over many orders of magnitude and, at the same time, the Hall angle can be very large.

3.1 First-principles calculations of spin relaxation times of conduction electrons in Cu with non-magnetic impurities

First-principles calculations of spin relaxation times of conduction electrons in Cu with nonmagnetic impurities

D. V. Fedorov,¹ P. Zahn,^{1,*} M. Gradhand,² and I. Mertig^{1,2}

¹Fachbereich Physik, Martin-Luther-Universität Halle-Wittenberg, D-06099 Halle, Germany

²Max-Planck-Institut für Mikrostrukturphysik, Weinberg 2, D-06120 Halle, Germany

(Received 15 January 2008; published 13 March 2008)

We have performed *ab initio* calculations of the spin relaxation time of conduction electrons in Cu containing different types of substitutional non-magnetic impurities. The results obtained with the treatment of the spin-flip transition matrix in the Born approximation are in good agreement with conduction electron spin resonance experiments. The distribution of the spin relaxation time over the Fermi surface is strongly related to the electronic properties of the impurity atom. The important role of charge relaxation around the impurity is discussed.

DOI: 10.1103/PhysRevB.77.092406

PACS number(s): 71.70.Ej, 72.25.Rb, 76.30.-v, 85.75.-d

Spintronics is a rapidly emerging field that exploits the spin degree of freedom of the electrons to store, transfer, and process information.^{1–4} In this respect, it is highly desirable to know how long the electron spin can be conserved without significant changes. To answer this question, one may use either the spin relaxation time measuring the temporal distance of two scattering events or the spin diffusion length characterizing the spatial separation of two spin-flip events. Recent spintronics experiments^{5–7} are able to estimate the spin diffusion length because this quantity is closely related to the spatial distribution of observables. However, the critical point for a theoretical prediction of the spin diffusion length is the calculation of the spin relaxation time.^{8,9} Moreover, the latter can also be determined experimentally. For instance, in the first observation of the spin Hall effect,¹⁰ the spin relaxation time was estimated by the decay of the Kerr signal in an external magnetic field. As discussed in Ref. 11, the characteristic behavior of the spin relaxation time observed experimentally points to the dominant role of the Elliott–Yafet^{12,13} spin-flip scattering mechanism in metals. In this Brief Report, we examine this spin relaxation mechanism caused by the spin-orbit interaction at the impurity site, and we restrict our considerations to bulk Cu at zero temperature. The considered processes are particularly important for the understanding of the *extrinsic* spin Hall effect.^{14–16}

Originally, the spin or magnetization relaxation time was introduced by Bloch¹⁷ to describe the relaxation of magnetization in nuclear magnetic resonance experiments. Dyson¹⁸ gave a definition of the spin relaxation time in the case of conduction electrons. Since the discovery of conduction electron spin resonance (CESR),¹⁹ such experiments were widely used to determine the spin relaxation time in metals. The full width at half amplitude of the absorption resonance with respect to the magnetic field ΔH shows a linear increase with impurity concentration.²⁰ The spin relaxation time T_1 , characterizing the finite lifetime of the spin state, is directly related to the linewidth of the CESR signal by $\Delta H = 2/\gamma T_1$.²⁰ Here, γ is the gyromagnetic factor.

Our present work is based on the determination of the spin-flip scattering time by means of the probability of a transition between electronic states with opposite spin orientations.^{21,22} The spin-flip scattering cross section related

to this time will be compared to the results of a simple model based on the scattering phase shift approach.^{23,24} A very good agreement with experimental CESR data is obtained. The shortcomings of a non-self-consistent treatment of the impurity problem are discussed.

The electronic structure of bulk Cu was self-consistently calculated in the framework of the nonrelativistic screened Korringa–Kohn–Rostoker multiple scattering Green’s function method.^{25–27} Spherical potentials in the atomic sphere approximation (ASA) were used. Exchange and correlation effects were included within the local-density approximation in the parametrization of Vosko *et al.*²⁸ The impurity problem was self-consistently solved in real space on a cluster of 55 atoms, including four nearest neighbor shells around the substitutional impurity to account for charge relaxation.

In the case of a non-magnetic system, the spin relaxation time T_1 is connected with the spin-flip scattering time $\tau^{\text{sf}} = \tau^{\uparrow\downarrow} = \tau^{\downarrow\uparrow}$ by using the relation $T_1 = (1/\tau^{\uparrow\downarrow} + 1/\tau^{\downarrow\uparrow})^{-1} = \tau^{\text{sf}}/2$.⁹ The k -dependent spin-flip scattering time τ_k^{sf} (where k is a shorthand notation for the Bloch wave vector \mathbf{k} and band index n)

$$\frac{1}{\tau_k^{\text{sf}}} = \frac{1}{\tau_k^{\uparrow\downarrow}} = \sum_{k'} P_{kk'}^{\uparrow\downarrow} \quad (1)$$

can be calculated by applying Fermi’s golden rule

$$P_{kk'}^{\uparrow\downarrow} = 2\pi c_0 N |T_{kk'}^{\uparrow\downarrow}|^2 \delta(E_k - E_{k'}). \quad (2)$$

Here, c_0 is the concentration of impurities and $c_0 N$ is the number of impurity atoms in the system. The linear dependence on the concentration holds for the case of dilute alloys and is based on the assumption that the impurity atoms are noninteracting. The elastic scattering probability $P_{kk'}^{\uparrow\downarrow}$ of the transition of an electron from the “spin-up” state $|\Phi_k^{\uparrow}\rangle$ into the “spin-down” state $|\Phi_{k'}^{\downarrow}\rangle$ is determined by the spin-flip transition matrix for one defect,

$$T_{kk'}^{\uparrow\downarrow} = \int_{\Omega_{\text{ASA}}^{\text{imp}}} d\mathbf{r} \Phi_k^{\uparrow\dagger}(\mathbf{r}) \left[\frac{2}{c^2 r} \frac{dV(r)}{dr} \hat{\mathbf{L}} \cdot \hat{\mathbf{S}} \right] \Phi_{k'}^{\downarrow}(\mathbf{r}). \quad (3)$$

The integration is performed over the impurity ASA sphere. In this Brief Report, Rydberg units are used with the speed of light $c=274.074$. The nonrelativistic spinors $\Phi_k^\uparrow(\mathbf{r})$ and $\Phi_{k'}^\downarrow(\mathbf{r})$ are the perturbed Bloch waves of the dilute alloy related to the corresponding Bloch functions of the ideal host by a Lippmann–Schwinger equation.²⁹ For a non-magnetic system, they are

$$\Phi_k^\uparrow(\mathbf{r}) = \Phi_k(\mathbf{r}) \times \begin{pmatrix} 1 \\ 0 \end{pmatrix} \quad \text{and} \quad \Phi_{k'}^\downarrow(\mathbf{r}) = \Phi_{k'}(\mathbf{r}) \times \begin{pmatrix} 0 \\ 1 \end{pmatrix}.$$

Thus, Eq. (3) is a Born approximation for the spin-flip transition matrix where the nonvanishing contributions are given by the $\hat{L}_-\hat{S}_+$ component only by applying the expansion of $\hat{\mathbf{L}} \cdot \hat{\mathbf{S}} = (\hat{L}_+\hat{S}_- + \hat{L}_-\hat{S}_+)/2 + \hat{L}_z\hat{S}_z$.

With the usual angular momentum expansion of the wave function in the case of spherical atomic potentials,

$$\Phi_k(\mathbf{r}) = \sum_{lm} C_{lm}(k) R_l(r) Y_{lm}(\hat{\mathbf{r}}), \quad (4)$$

we can write

$$\begin{aligned} \frac{1}{\tau_k^{\text{sf}}} &= \frac{2\pi c_0}{\Omega_{\text{BZ}}} \sum_{lm} \sum_{l'm'} \xi_l \xi_{l'} C_{lm}^*(k) C_{l'm'}(k) \\ &\times \sqrt{l(l+1) - m(m+1)} \sqrt{l'(l'+1) - m'(m'+1)} \\ &\times \oint_{E_{k'}=E_F} \frac{dS_{k'}}{|\mathbf{v}_{k'}|} C_{l,m+1}(k') C_{l',m'+1}^*(k'). \end{aligned} \quad (5)$$

Here, Ω_{BZ} is the volume of the Brillouin zone and \mathbf{v}_k denotes the group velocity vector of state k at the Fermi level E_F . The functions $Y_{lm}(\hat{\mathbf{r}})$ are the complex spherical harmonics, and the coefficients ξ_l are given by the following expression:

$$\xi_l = \int_0^{R_{\text{ASA}}^{\text{imp}}} dr |R_l(r)|^2 \frac{r}{c^2} \frac{dV(r)}{dr}, \quad (6)$$

where the radial functions $R_l(r)$ are normalized to unity: $\int dr r^2 |R_l(r)|^2 = 1$. Thus, ξ_l corresponds to half of the spin-orbit constants introduced in Ref. 13. To compare with the experiment, we use the spin-flip scattering time averaged over the Fermi surface by using the following procedure:^{21,22} $1/\tau^{\text{sf}} = \langle 1/\tau_k^{\text{sf}} \rangle_k$. This average can be related to the spin-flip scattering cross section²⁰

$$\sigma_{\text{sf}} = \Omega_{\text{ws}} / v_F \tau^{\text{sf}} c_0, \quad (7)$$

where v_F is the Fermi surface average of the Fermi velocity and Ω_{ws} denotes the volume of the bulk Wigner–Seitz cell, which gives the inverse density of atoms in the host.

The spin-flip scattering cross section σ_{sf} can also be expressed in terms of differences of the phase shifts δ_j for the levels $j=l \pm 1/2$,^{23,24}

$$\sigma_{\text{sf}} = \frac{24\pi}{3} \sum_{E_F} \frac{l(l+1)}{2l+1} \sin^2[\delta_{l+1/2}(E_F) - \delta_{l-1/2}(E_F)]. \quad (8)$$

Let us now assume a weak scattering and replace the sine in Eq. (8) by the difference of the phase shifts. To first order in the spin-orbit interaction, it can be written as²³

TABLE I. Spin relaxation time T_1 and momentum relaxation time τ in bulk Cu with an impurity concentration of 1 at. %. The experimental results for T_1 were derived from the data for ΔH of Tables III and IV of Ref. 20. For the calculation of τ , the scheme described in Ref. 29 was applied. All values are given in picoseconds.

Impurity	Other calculation ^a T_1	CESR ^b T_1	Our results	
			T_1	τ
Ni	4.0	2.2 ± 0.2	1.9	0.057
Zn	125	64 ± 9	58	0.078
Ga	33	30 ± 4	26	0.017
Ge	14	14 ± 2	12	0.0072
As		8.6 ± 0.7	6.7	0.0043
Au	2.0 ± 0.4	0.62 ± 0.21	0.67	0.48

^aReference 22.

^bReference 20.

$\delta_{l+1/2}(E_F) - \delta_{l-1/2}(E_F) \approx \pi n_l(E_F) \xi_l / 2$, where $n_l(E_F)$ is the angular momentum resolved impurity local density of states at the Fermi level. As a result, we obtain

$$\sigma_{\text{sf}} = \sum_{l>0} \sigma_{\text{sf}}(l) = \frac{2}{3} \frac{\pi^3}{E_F} \sum_{l>0} \frac{l(l+1)}{2l+1} \xi_l^2 n_l^2(E_F). \quad (9)$$

Similar approximations were made in Ref. 24, and it was demonstrated that a good agreement with experiment can be reached for a Mg host.³⁰ Equation (9) provides a possibility for a simplified analysis of the results discussed below.

Table I summarizes the spin relaxation time T_1 for bulk Cu with different types of impurities calculated by our *ab initio* method. Our calculation is compared with CESR experiments of Monod and Schultz²⁰ and with the calculation of Holzwarth and Lee.²² A good agreement between our results and the experimental data is found. The values obtained in Ref. 22 show a significant deviation from the experimental data, except in the case of Ga and Ge impurities. Holzwarth and Lee²² neglected spin-orbit interactions in the Cu host and performed a relativistic treatment of impurity scattering based on the solution of the Dirac equation for the muffin-tin model. Nevertheless, approximate muffin-tin potentials were constructed for substitutional impurities in Cu by superposition of atomic potentials. Thus, the lack of a self-consistent solution for the impurity problem, including charge relaxation around the impurity, seems to be the main reason for this discrepancy. In addition, we present our results for the momentum relaxation time τ (Table I) to make a comparison with T_1 . In the case of Au impurities, both relaxation times are already of the same order of magnitude. The reason is that the momentum scattering is quite weak since Au and Cu are isovalent. At the same time, the spin-flip scattering is much stronger for Au with respect to other impurities because of the large atomic number of Au.

Monod and Schultz²⁰ made estimations based on the virtual bound state (VBS) model, including the spin-orbit interaction. The obtained values for the spin-flip scattering cross section are reasonable but do not quantitatively reproduce

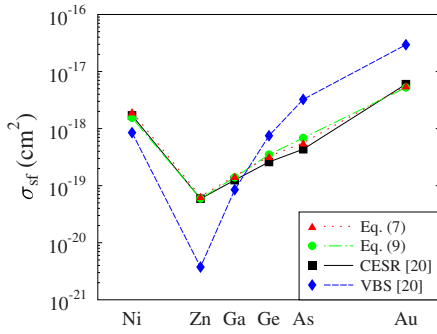


FIG. 1. (Color online) Spin-flip scattering cross section for impurities in bulk Cu (the ordinate is a logarithmic scale). The lines are to guide the eyes.

the experimental situation.²⁰ We performed calculations of σ_{sf} by using Eq. (7), with the values of $\tau^{sf}=2T_1$ taken from Table I, and by using Eq. (9) for comparison. Figure 1 shows σ_{sf} for bulk Cu with different types of impurities obtained by our calculations. For comparison, the values derived from the experimental data²⁰ and the estimations based on the VBS model²⁰ are shown. We emphasize that the spin-flip scattering cross section used in Ref. 20 is actually twice the σ_{sf} . To follow the calculation of Ref. 20, we use for Eq. (7) the same value of the averaged Fermi velocity $v_F=1.57 \times 10^8$ cm/s taken from Ref. 31, while $v_F=1.1 \times 10^8$ cm/s was obtained in our calculation. The corresponding scaling procedure was also applied to Eq. (9) to ensure a correct comparison of σ_{sf} values.

It is obvious from Fig. 1 that Eq. (9) provides a good agreement with the results obtained by applying Eq. (7) as well as with the experimental data. Moreover, as shown in Table II, the experiment can be well reproduced by restricting the sum of Eq. (9) to the $l=2$ (d electrons) term only for Ni impurities and to the $l=1$ (p electrons) term only for the sp impurities considered. For Au impurities, the $l=1$ and the $l=2$ terms are of comparable orders due to the large atomic number. Thus, the assumption made in Ref. 20, taking into account merely one type of scattered electron (p or d), is quite reasonable. The main reason for the deviation of the VBS model from experiment is the lack of charge relaxation around the impurity. The atomic parameters for the spin-orbit constant and the phase shifts for an impurity atom differ remarkably from those for an isolated atom. In particular, the spin-orbit constant for p electrons at Zn impurities used in

TABLE II. The l -decomposed spin-flip scattering cross section $\sigma_{sf}(l)$ for impurities in Cu according to Eq. (9). All values are given in cm^2 .

Impurity	$\sigma_{sf}(l=1)$	$\sigma_{sf}(l=2)$	$\sigma_{sf}(l=3)$
Ni	3.2×10^{-20}	2.2×10^{-18}	3.1×10^{-29}
Zn	8.1×10^{-20}	4.6×10^{-21}	4.4×10^{-29}
Ga	2.0×10^{-19}	8.1×10^{-22}	7.0×10^{-29}
Ge	5.0×10^{-19}	3.8×10^{-22}	1.1×10^{-28}
As	9.8×10^{-19}	2.8×10^{-22}	1.5×10^{-28}
Au	5.3×10^{-18}	2.2×10^{-18}	2.8×10^{-25}

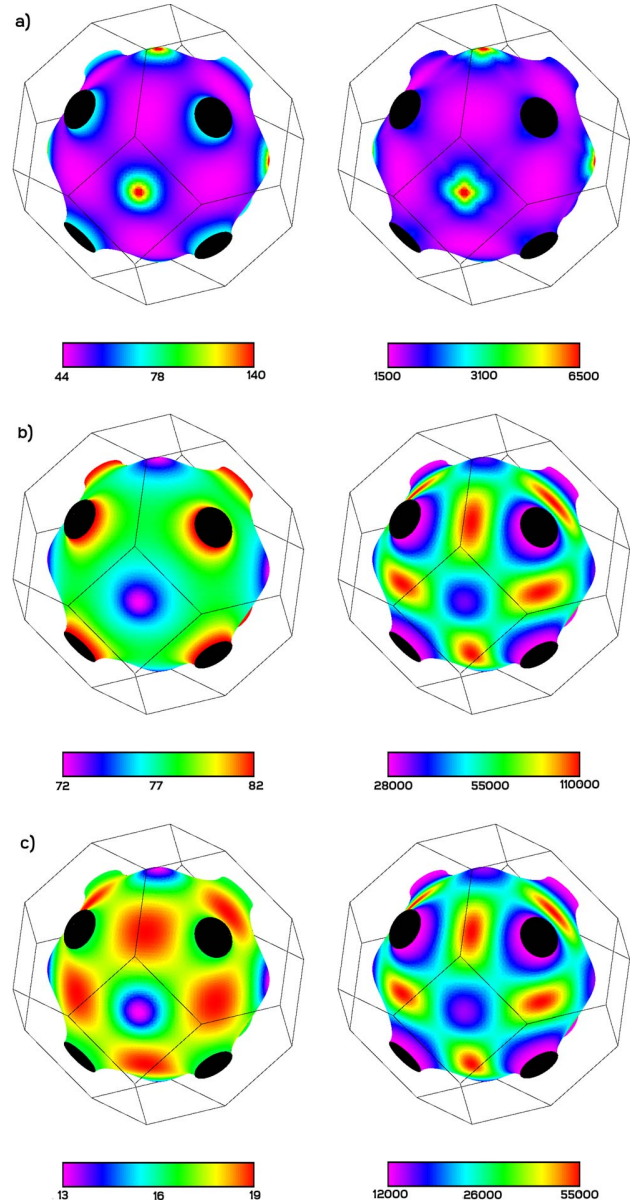


FIG. 2. (Color online) Anisotropic τ (left) and T_1 (right) on the Fermi surface of Cu for (a) Ni, (b) Zn, and (c) Ga impurities with a defect concentration of 1 at. %. All values on the logarithmic scale are given in femtoseconds.

Ref. 20 was assumed to be 48 meV, whereas our self-consistent calculation gives 180 meV.

The distributions of the momentum relaxation time τ and the spin relaxation time T_1 on the Fermi surface of Cu are represented in Fig. 2 for Ni, Zn, and Ga impurities. The color scale indicates the increase in relaxation times going from magenta to red. With respect to the Fermi surface of Cu, it is known that the lack of s electrons is largest at the necks, the lack of p electrons is between the necks, and the lack of d electrons is mostly located around the van Hove singularities in the (100) direction.²⁹ First, let us consider the distribution of τ . The electronic configuration of the impurity atom determines the scattering properties. For example, a Ni impurity is a typical d scatterer.²⁹ It is important to keep in mind

that the maximal values correspond to the red areas and indicate weak scattering, while the magenta areas indicate strong scattering. In the case of Ni impurity, the weakest scattering occurs exactly where a d character is missing. Zn and Ga impurities are typical sp scatterers.²⁹ However, the scattering of s electrons dominates for Zn, and the scattering of p electrons is dominant for Ga. In the case of the spin-flip scattering, according to Eq. (5), s -like electrons do not give any contributions since the spin-orbit interaction vanishes. It is obvious from the top row of Fig. 2 that the momentum and the spin relaxation time show practically the same distribution of scattering strength for Ni impurities. For Zn impurities, the difference is much more pronounced because s electrons dominating the momentum relaxation time do not contribute to the spin relaxation. Spin-flip scattering is weak where a p character is missing, while scattering is strong for the states with a dominant p character. The distributions of the two relaxation times for Ga are quite similar to each other. The picture is determined by p electrons. The corresponding pictures for Ge, As, and Au impurities are qualitatively the same as those for Ga impurities. Actually, as can be seen in Table II, Au impurities cause significant spin-flip

scattering contributions in both p and d channels. In general, p electrons dominate for the considered sp scatterers.

In summary, we have performed *ab initio* calculations of the spin relaxation time and the corresponding scattering cross section of the conduction electrons in bulk Cu containing different types of impurities within the Born approximation for the spin-flip transition matrix. The obtained results are in good agreement with CESR experiments.²⁰ Generally, the spin relaxation time is smaller by several orders of magnitude in comparison to the momentum relaxation time, except for heavy impurities such as Au where spin and momentum relaxation times are of the same order of magnitude. As in the case of the momentum relaxation time, there is a strong relation between the distribution of the spin relaxation time over the Fermi surface and the electronic properties of the impurity atom. The spin-flip scattering is dominated by d electrons for Ni impurities, by p electrons for Zn, Ga, Ge, and As impurities, and by electrons of both characters for Au impurities. It is shown that the self-consistent solution of the impurity problem, including charge relaxation, is essential in properly describing the spin relaxation time.

*peter.zahn@physik.uni-halle.de

¹*Semiconductor Spintronics and Quantum Computation*, edited by D. D. Awschalom, D. Loss, and N. Samarth (Springer-Verlag, Berlin, 2002).

²G. A. Prinz, *Science* **282**, 1660 (1998).

³S. A. Wolf, D. D. Awschalom, R. A. Buhrmann, J. M. Daughton, S. von Molnár, M. L. Roukes, A. Y. Chtchelkanova, and D. M. Treger, *Science* **294**, 1488 (2001).

⁴F. J. Jedema, H. B. Heersche, A. T. Filip, J. J. A. Baselmans, and B. J. van Wees, *Nature (London)* **416**, 713 (2002).

⁵T. Kimura, J. Hamrle, and Y. Otani, *Phys. Rev. B* **72**, 014461 (2005).

⁶T. Kimura, Y. Otani, T. Sato, S. Takahashi, and S. Maekawa, *Phys. Rev. Lett.* **98**, 156601 (2007).

⁷L. Vila, T. Kimura, and Y. C. Otani, *Phys. Rev. Lett.* **99**, 226604 (2007).

⁸T. Valet and A. Fert, *Phys. Rev. B* **48**, 7099 (1993).

⁹A. Fert and S. F. Lee, *Phys. Rev. B* **53**, 6554 (1996).

¹⁰Y. K. Kato, R. C. Myers, A. C. Gossard, and D. D. Awschalom, *Science* **306**, 1910 (2004).

¹¹J. Fabian and S. Das Sarma, *J. Vac. Sci. Technol. B* **17**, 1708 (1999).

¹²R. J. Elliott, *Phys. Rev.* **96**, 266 (1954).

¹³Y. Yafet, in *Solid State Physics*, edited by F. Seitz and D. Turnbull (Academic, New York, 1963), Vol. 14.

¹⁴M. I. D'yakonov and V. I. Perel', *JETP Lett.* **13**, 467 (1971); *Phys. Lett.* **35A**, 459 (1971).

¹⁵J. E. Hirsch, *Phys. Rev. Lett.* **83**, 1834 (1999).

¹⁶S. Zhang, *Phys. Rev. Lett.* **85**, 393 (2000).

¹⁷F. Bloch, *Phys. Rev.* **70**, 460 (1946).

¹⁸F. J. Dyson, *Phys. Rev.* **98**, 349 (1955).

¹⁹T. W. Griswold, A. F. Kip, and C. Kittel, *Phys. Rev.* **88**, 951 (1952).

²⁰P. Monod and S. Schultz, *J. Phys. (Paris)* **43**, 393 (1982).

²¹J. R. Asik, M. A. Ball, and C. P. Slichter, *Phys. Rev. Lett.* **16**, 740 (1966).

²²N. A. W. Holzwarth and M. J. G. Lee, *Phys. Rev. B* **13**, 2331 (1976).

²³Y. Yafet, *J. Appl. Phys.* **39**, 853 (1968).

²⁴N. Papanikolaou, N. Stefanou, P. H. Dederichs, S. Geier, and G. Bergmann, *Phys. Rev. Lett.* **69**, 2110 (1992).

²⁵P. Zahn, J. Binder, I. Mertig, R. Zeller, and P. H. Dederichs, *Phys. Rev. Lett.* **80**, 4309 (1998).

²⁶L. Szunyogh, B. Újfalussy, P. Weinberger, and J. Kollár, *Phys. Rev. B* **49**, 2721 (1994).

²⁷N. Papanikolaou, R. Zeller, and P. H. Dederichs, *J. Phys.: Condens. Matter* **14**, 2799 (2002).

²⁸S. H. Vosko, L. Wilk, and M. Nusair, *Can. J. Phys.* **58**, 1200 (1980).

²⁹I. Mertig, *Rep. Prog. Phys.* **62**, 237 (1999).

³⁰The factor of $2/3$ is missing in expression (2) of Ref. 24, which corresponds to our Eq. (8). It seems to be the reason why, as written in Ref. 24, "the experimental values lie about 30% below the theoretical ones" in the case of the Mg host. So, the approach used in Ref. 24 should give a better agreement with the experiment than what was presented there. Our expression is based on Ref. 23.

³¹N. W. Ashcroft and N. D. Mermin, *Solid State Physics* (Holt-Saunders, New York, 1976).

Erratum: First-principles calculations of spin relaxation times of conduction electrons in Cu with nonmagnetic impurities [Phys. Rev. B 77, 092406 (2008)]

D. V. Fedorov, P. Zahn, M. Gradhand, and I. Mertig
(Received 15 January 2009; published 10 February 2009)

DOI: [10.1103/PhysRevB.79.059901](https://doi.org/10.1103/PhysRevB.79.059901) PACS number(s): 71.70.Ej, 72.25.Rb, 76.30.-v, 85.75.-d, 99.10.Cd

The results for the anisotropic spin relaxation time T_1 presented in our paper were obtained using the symmetry group of the nonrelativistic Hamiltonian. In reality, the spin-orbit interaction in Eq. (3) reduces the symmetry. The corrected Fig. 2 is given below. The momentum relaxation time τ is unchanged.

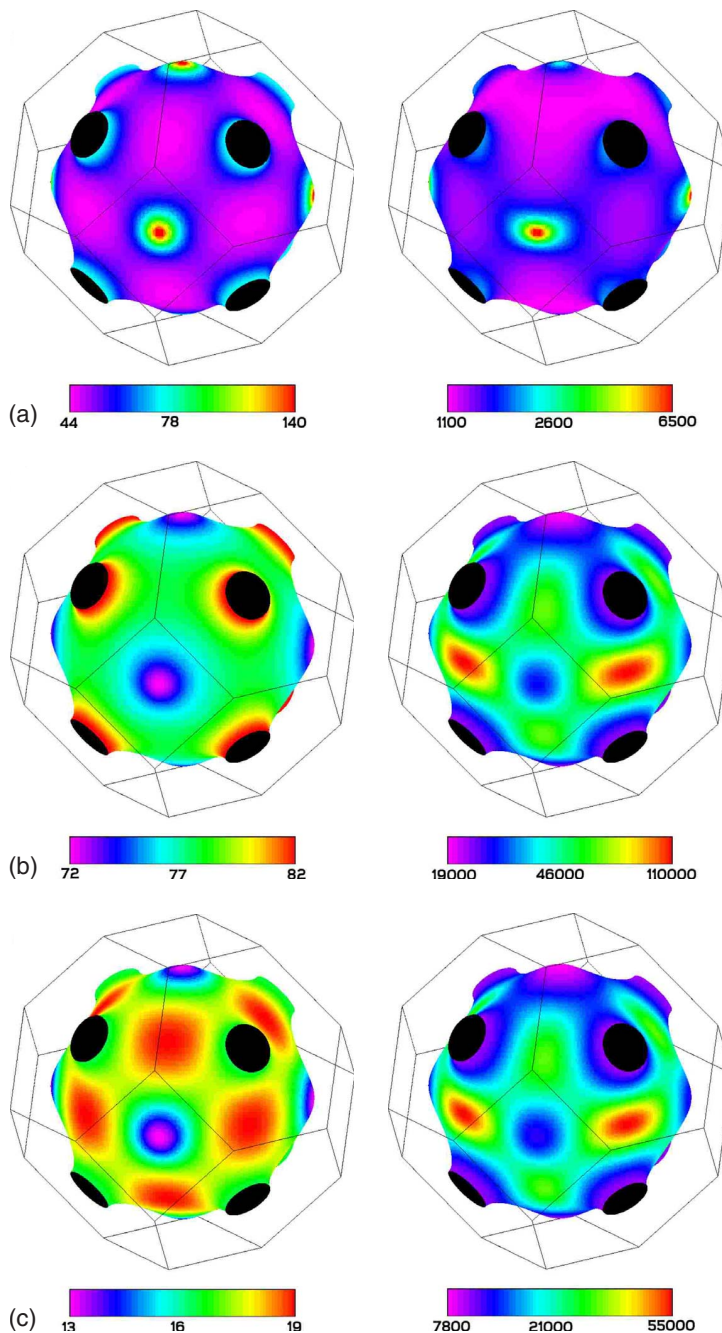


FIG. 2. (Color online) Anisotropic τ (left) and T_1 (right) on the Fermi surface of Cu for (a) Ni, (b) Zn, and (c) Ga impurities with a defect concentration of 1 at. %. All values on the logarithmic scale are given in femtoseconds.

TABLE I. Spin relaxation time T_1 and momentum relaxation time τ in bulk Cu with an impurity concentration of 1 at. %. The experimental results for T_1 were derived from the data for ΔH of Tables III and IV of Ref. 20. For the calculation of τ , the scheme described in Ref. 29 was applied. All values are given in picoseconds.

Impurity	Other calculation ^a	CESR ^b	Our results	
	T_1	T_1	T_1	τ
Ni	4.0	2.2 ± 0.2	1.6	0.057
Zn	125	64 ± 9	49	0.078
Ga	33	30 ± 4	22	0.017
Ge	14	14 ± 2	10	0.0072
As		8.6 ± 0.7	5.7	0.0043
Au	2.0 ± 0.4	0.62 ± 0.21	0.56	0.48

^aReference 22.

^bReference 20.

The integration over the Fermi surface in Eq. (5) was performed in our paper using the irreducible part of the Brillouin zone corresponding to the symmetry group of the non-relativistic Hamiltonian. It is six times smaller than the irreducible part of the Brillouin zone in the presence of the spin-orbit coupling. The correction causes small deviations of the averaged values for T_1 presented in the column ‘‘Our results’’ of Table I. The momentum relaxation time τ is not influenced at all.

In fact, the correction gives a reduction of the values of T_1 for all \mathbf{k} points with nonzero component along z axis (quantization axis). As a consequence, we obtain a systematic reduction of the averaged values for T_1 in comparison to the published ones.

The values of the spin-flip scattering cross section σ_{sf} calculated by Eq. (7) have to be corrected along these lines. But, the corresponding changes are nearly invisible in Fig. 1 due to the logarithmic scale. We emphasize that the whole discussion of our results as well as the conclusions made in our paper are still valid.

3.2 Spin polarization on the Fermi surfaces of metals by the KKR method

Spin polarization on Fermi surfaces of metals by the KKR method

Martin Gradhand,^{1,2,*} Michael Czerner,² Dmitry V. Fedorov,² Peter Zahn,² Bogdan Yu. Yavorsky,² László Szunyogh,³ and Ingrid Mertig^{2,1}

¹Max-Planck-Institut für Mikrostrukturphysik, Weinberg 2, D-06120 Halle, Germany

²Institut für Physik, Martin-Luther-Universität Halle-Wittenberg, D-06099 Halle, Germany

³Department of Theoretical Physics, Budapest University of Technology and Economics, H-1521 Budapest, Hungary

(Received 21 September 2009; revised manuscript received 29 October 2009; published 11 December 2009)

With the implementation of a relativistic Korringa-Kohn-Rostoker Green's function and band-structure method, we analyze the spin-expectation value of the electron states on the Fermi surface of nonmagnetic as well as magnetic metals. It is shown that for relatively light elements such as Cu the spin states are well defined. A separation of all electron states to "up" and "down" spin-polarized states can be done even in the case of quite heavy but monovalent elements such as Au. In contrast, for heavy polyvalent metals such as Pt, the expectation value of the spin operator can be close to zero in large regions of the Fermi surface. In this case the nonrelativistic language of well-defined "spin-up" and "spin-down" states is not valid anymore. For magnetic materials, the relativistic Fermi surfaces change their topology with respect to the nonrelativistic majority and minority sheets because of spin-orbit driven avoided crossings of the bands. As a result, regions with vanishing spin polarization appear.

DOI: [10.1103/PhysRevB.80.224413](https://doi.org/10.1103/PhysRevB.80.224413)

PACS number(s): 71.15.-m, 71.18.+y, 71.20.-b

I. INTRODUCTION

The spin degree of freedom of an electron has attracted a lot of attention over the last years.¹⁻⁶ Since the field of spintronics opened new perspectives in data storage and information technology. After the discovery of giant magnetoresistance,^{7,8} tunneling magnetoresistance,⁹⁻¹² and current-induced switching,¹³⁻¹⁶ phenomena such as spin Hall effect^{1,4,17,18} and anomalous Hall effect¹⁹⁻²² attracted attention. The latter effects are caused by spin-orbit interaction. Thus, a detailed insight into the microscopic origin requires a relativistic description of the electron system.

While the intrinsic contribution to the anomalous Hall conductivity was discussed originally in terms of an integral of the Berry curvature over all occupied states, it was later shown that for low temperatures this quantity can be expressed as a Fermi-surface property.^{23,24} The same holds for the spin Hall effect in nonmagnetic materials. For an understanding of these effects the spin degree of freedom of an electron state is an important quantity. Experimentally, the spin orientation can be changed with respect to the lattice structure either by spin injection from a ferromagnet into a nonmagnetic material or by an external magnetic field. As a consequence spin-flip scattering is observed to be anisotropic.²⁵ To account for related effects, we present a method to analyze the spin-expectation value of the electronic states at the Fermi surface within a fully relativistic (FR) treatment.

A further motivation for our work is the existence of so-called spin hot spots. They are characterized by zero spin polarization and occur at the Fermi surface.²⁶ Level crossings at the zone boundary or at high-symmetry points, or lines of accidental degeneracy are typical locations on the Fermi surface. Spin hot spots exist usually for polyvalent metals such as Al, Pd, Mg, and Be and cause an unexpected fast spin relaxation.²⁶

For magnetic materials the spin hot spots are caused by spin-orbit driven hybridization points, i.e., \mathbf{k} points with

avoided crossing. That is, the considered states would be degenerate in a nonrelativistic (NR) treatment, "spin-up" and "spin-down" bands cross each other. Spin-orbit interaction forces a splitting of the two states and the spin polarization vanishes at the splitting points. If such points occur close to the Fermi level, they can enhance spin-flip scattering by several orders of magnitude and cause ultrafast demagnetization.²⁷ For a theoretical study of this problem, it is very desirable to know the spin-mixing parameter of the electron states in the vicinity of the Fermi level.²⁸

The aim of this paper is to introduce our *ab initio* method that provides a scheme for the calculation of the relativistic band structure and wave functions. In the application of this method, we present relativistic Fermi surfaces and consider the spin polarization of the corresponding electronic states.

We start with a short introduction of the relativistic Korringa-Kohn-Rostoker (KKR) band-structure theory²⁹⁻³⁸ and discuss the treatment of degenerate bands in a nonmagnetic system with space inversion symmetry. For the Fermi-surface calculation, we present Cu, Au, and Pt as nonmagnetic and Fe as magnetic examples. Different spin-mixing parameters obtained for several materials will be discussed in detail.

II. METHOD

For the self-consistent procedure, we use a screened KKR-Green's function method,^{39,40} generalized relativistically.^{35,38} It is based on the density-functional theory in the local spin-density approximation with the parametrization of Vosko *et al.*⁴¹ The magnetic moments are forced to be collinear. An angular momentum cutoff $l_{max}=3$ is used for the Green's function expansion. The relativistic Kohn-Sham-Dirac equation

$$\hat{H}(\mathbf{r})\Psi_{n\mathbf{k}}(\mathbf{r}) = W_n(\mathbf{k})\Psi_{n\mathbf{k}}(\mathbf{r}) \quad (1)$$

with the Hamiltonian

$$\hat{H}(\mathbf{r}) = \frac{\hbar}{i} c \hat{\alpha} \nabla_{\mathbf{r}} + \hat{I}_4 V_{eff}(\mathbf{r}) + \hat{\beta} \boldsymbol{\sigma} \cdot \mathbf{B}_{eff}(\mathbf{r}) + mc^2 \hat{\beta} \quad (2)$$

and the 4×4 matrices

$$\hat{\alpha} = \begin{pmatrix} 0 & \boldsymbol{\sigma} \\ \boldsymbol{\sigma} & 0 \end{pmatrix}, \quad \hat{\beta} = \begin{pmatrix} \hat{I}_2 & 0 \\ 0 & -\hat{I}_2 \end{pmatrix}, \quad \hat{I}_4 = \begin{pmatrix} \hat{I}_2 & 0 \\ 0 & \hat{I}_2 \end{pmatrix} \quad (3)$$

is solved. Here \hat{I}_2 is the 2×2 unit matrix, n is the band index, and \mathbf{k} is the Bloch vector. First we use the KKR-Green's function method to obtain the scalar potential $V_{eff}(\mathbf{r})$ and the vector of the effective magnetic field $\mathbf{B}_{eff}(\mathbf{r})$ self-consistently. Then, the KKR band-structure method is applied to compute the electron energy spectrum

$$W_n(\mathbf{k}) = E_n(\mathbf{k}) + mc^2. \quad (4)$$

The band structure $E_n(\mathbf{k})$ is calculated on the real energy axis with an angular momentum cutoff $l_{max}=3$. The cluster used to calculate the screened structure constants contained at least 225 atoms depending on the crystal structure.

We have different options to analyze the influence of relativistic effects. First of all, the results of the FR calculation can be compared with the ones obtained from the NR equation. In addition, in the fully relativistic calculation, the spin-orbit interaction can be scaled to zero.⁴² This corresponds to the so-called scalar-relativistic approximation (SRA). The scaling of spin-orbit coupling can be performed by a continuous variable x . Calculations without scaling (FR[$x=1$]) and with scaling to zero (FR[$x=0$]) are discussed, respectively.

The relativistic band-structure calculations are performed analogously to the NR case.⁴³ However, the wave functions are expanded now into spin-angular functions χ_Q as³⁸

$$\Psi_{n\mathbf{k}}(\mathbf{r}) = \sum_Q \sum_{Q'} a_{Q'}^n(\mathbf{k}) \begin{pmatrix} g_{QQ'}(r) \chi_Q(\hat{\mathbf{r}}) \\ i f_{QQ'}(r) \chi_{\bar{Q}}(\hat{\mathbf{r}}) \end{pmatrix}, \quad (5)$$

where $Q = \{\kappa\mu\}$ and $\bar{Q} = \{-\kappa\mu\}$. The solutions of the radial differential equation in the atomic sphere approximation for the effective potential are $g_{QQ'}(r)$ for the large and $f_{QQ'}(r)$ for the small component, respectively. The band structure $E_n(\mathbf{k})$ is evaluated from the secular KKR equation

$$\det[\hat{G}(\mathbf{k}, E) - [\Delta \hat{t}(E)]^{-1}] = 0 \quad (6)$$

with the screened structural Green's function $\hat{G}(\mathbf{k}, E)$ and the difference of the single-site t matrices $\Delta \hat{t}(E) = \hat{t} - \hat{t}_r$ with \hat{t}_r being the t matrix of the reference system formed by repulsive potential wells. The expansion coefficients $a_{Q'}^n(\mathbf{k})$ are calculated from the KKR eigenvalue problem

$$\sum_{Q'} [G_{QQ'}(\mathbf{k}, E_n) - [\Delta \hat{t}^{-1}(E_n)]_{QQ'}] c_{Q'}^n(\mathbf{k}) = 0 \quad (7)$$

via

$$a_{Q'}^n(\mathbf{k}) = \sum_{Q''} [\Delta \hat{t}^{-1}(E_n)]_{QQ''} c_{Q''}^n(\mathbf{k}). \quad (8)$$

In the case of a nonmagnetic crystal with inversion symmetry every \mathbf{k} state is twofold degenerate.^{44,45} Let us label the

two orthonormal wave functions corresponding to that degeneracy as $|\Psi_{\mathbf{k}}^1\rangle$ and $|\Psi_{\mathbf{k}}^2\rangle$. All linear combinations of these functions are also solutions at the same energy $E_n(\mathbf{k})$. In the nonrelativistic case one would associate them with spin-up and spin-down states relative to an arbitrary quantization axis. For the relativistic treatment we have to define a quantization axis. In an experimental situation, this axis can be given by a ferromagnet used for injection of spin-polarized electrons. For a theoretical consideration, we can choose, for instance, the z direction as the quantization axis. Then, we apply the following unitary transformation:

$$\begin{aligned} |\Psi_{\mathbf{k}}^3\rangle &= c_1 |\Psi_{\mathbf{k}}^1\rangle + c_2 |\Psi_{\mathbf{k}}^2\rangle, \\ |\Psi_{\mathbf{k}}^4\rangle &= -c_2^* |\Psi_{\mathbf{k}}^1\rangle + c_1^* |\Psi_{\mathbf{k}}^2\rangle \end{aligned} \quad (9)$$

with $|c_1|^2 + |c_2|^2 = 1$. Here the coefficients c_1 and c_2 should fulfill the conditions of spin alignment along z direction for the two new states

$$\begin{aligned} \langle \Psi_{\mathbf{k}}^3 | \hat{\beta} \sigma_x | \Psi_{\mathbf{k}}^3 \rangle &= \langle \Psi_{\mathbf{k}}^3 | \hat{\beta} \sigma_y | \Psi_{\mathbf{k}}^3 \rangle = 0, \\ \langle \Psi_{\mathbf{k}}^4 | \hat{\beta} \sigma_x | \Psi_{\mathbf{k}}^4 \rangle &= \langle \Psi_{\mathbf{k}}^4 | \hat{\beta} \sigma_y | \Psi_{\mathbf{k}}^4 \rangle = 0. \end{aligned} \quad (10)$$

In fact, the upper conditions automatically provide the lower one in Eq. (10). Explicit expressions for the coefficients c_1 and c_2 are given in the Appendix. The normalization

$$\langle \Psi_{\mathbf{k}}^3 | \Psi_{\mathbf{k}}^3 \rangle = \langle \Psi_{\mathbf{k}}^4 | \Psi_{\mathbf{k}}^4 \rangle = 1 \quad (11)$$

and the orthogonality

$$\langle \Psi_{\mathbf{k}}^3 | \Psi_{\mathbf{k}}^4 \rangle = 0 \quad (12)$$

are conserved under the unitary transformation in Eq. (9). The choice of the quantization axis in z direction is not unique and any arbitrary direction can be chosen. For the further discussion of the results the expectation value of the z component of the spin with the transformed wave functions

$$P_{\mathbf{k}} = \langle \Psi_{\mathbf{k}}^3 | \hat{\beta} \sigma_z | \Psi_{\mathbf{k}}^3 \rangle = -\langle \Psi_{\mathbf{k}}^4 | \hat{\beta} \sigma_z | \Psi_{\mathbf{k}}^4 \rangle \quad (13)$$

will be referred to as spin polarization. For a clear interpretation, as what follows, we shall label the states constructed from the degenerate band with $P_{\mathbf{k}} > 0$ by $|\Psi_{\mathbf{k}}^+\rangle$ and those with $P_{\mathbf{k}} < 0$ by $|\Psi_{\mathbf{k}}^-\rangle$. In the nonrelativistic case (without spin-orbit coupling) the two states simplify to the degenerate spin-up $|\Psi_{\mathbf{k}}^+\rangle = |\Phi_{\mathbf{k}}, \uparrow\rangle$ and spin-down states $|\Psi_{\mathbf{k}}^-\rangle = |\Phi_{\mathbf{k}}, \downarrow\rangle$.

III. RESULTS

A. Band structure

First, we present the band-structure calculations to show that our relativistic code works properly. Pt is chosen as a nonmagnetic example since the large atomic number leads to significant relativistic effects in the electronic structure. Figure 1 shows the relativistic band structure of Pt, in comparison to a nonrelativistic approximation which fails for such a heavy element. The electronic structures obtained with the two approaches differ strongly over the whole Brillouin zone. Our relativistic results are in very good agreement to earlier calculations.⁴⁶

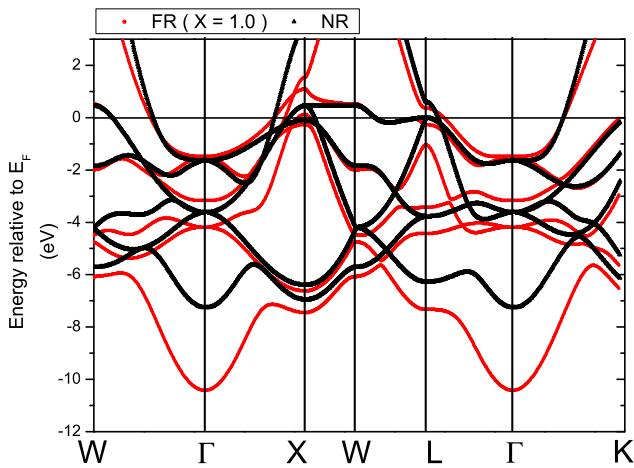


FIG. 1. (Color online) Band structure of Pt from the fully relativistic (gray, red) and the nonrelativistic (black) calculation.

To illuminate the origin of changes in the band structure going from NR to the FR calculation, we perform the FR [$x=0$] calculation. The results are presented in Fig. 2. Especially, the flat bands are affected and the degeneracy at symmetry points is lifted by the spin-orbit coupling, whereas the band bottom at the Γ point is correctly reproduced within SRA (FR[$x=0$]).

In contrast, the band structure of Fe shown in Fig. 3 is only slightly affected by relativistic effects since Fe is a light element in comparison to Pt. However, the changes are important because some degeneracies are lifted leading to avoided crossings of former majority and minority bands.^{46–48} It causes a mixing of bands which were well separated with respect to the spin in the nonrelativistic calculation. This result is especially important for the topology of the Fermi surface and the spin-polarization analysis in the following section.

B. Fermi surface

Here we present the relativistic Fermi surfaces of Cu, Au, Pt, and Fe with the spin polarization of the electronic states.

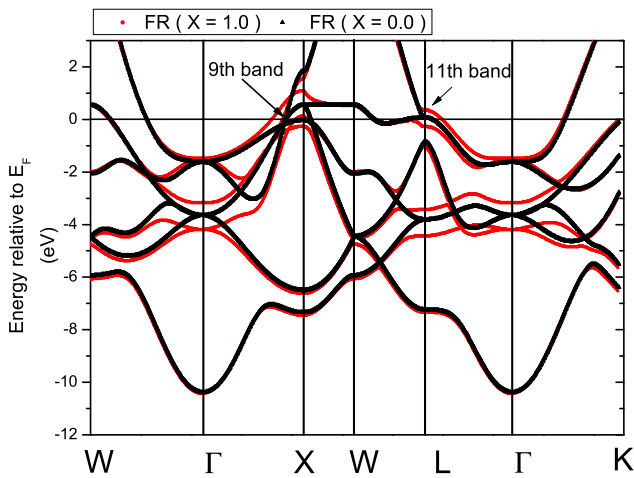


FIG. 2. (Color online) Band structure of Pt from the fully relativistic (gray, red) and the relativistic with the spin-orbit coupling scaled to zero (black) calculation.

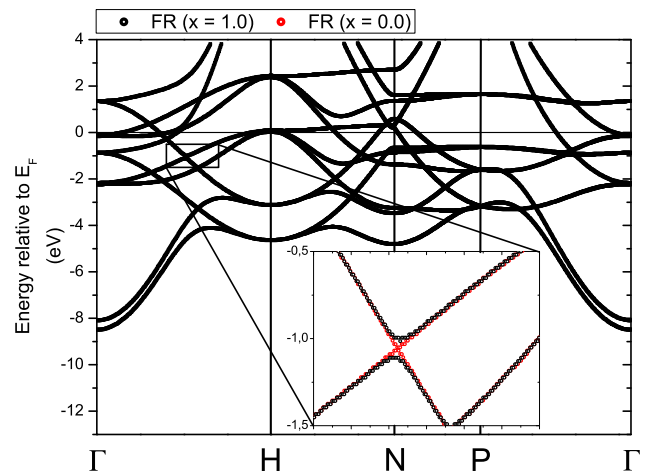


FIG. 3. (Color online) Calculated fully relativistic band structure of bcc Fe. The small inset shows a comparison to the calculation with the spin-orbit coupling scaled to zero ($x=0$). The spin-orbit interaction leads to avoided crossings.

Let us first analyze the polarization of the nonmagnetic Fermi surfaces. The quantization axis is defined by the transformation in Eqs. (9) and (10) explained in Sec. II. The polarization of $|\Psi_{\mathbf{k}}^{\pm}\rangle$ states only is shown in Fig. 4. A figure for $|\Psi_{\mathbf{k}}^{-}\rangle$ states would look the same but with opposite sign. For the monovalent metals Au and Cu the band at the Fermi level

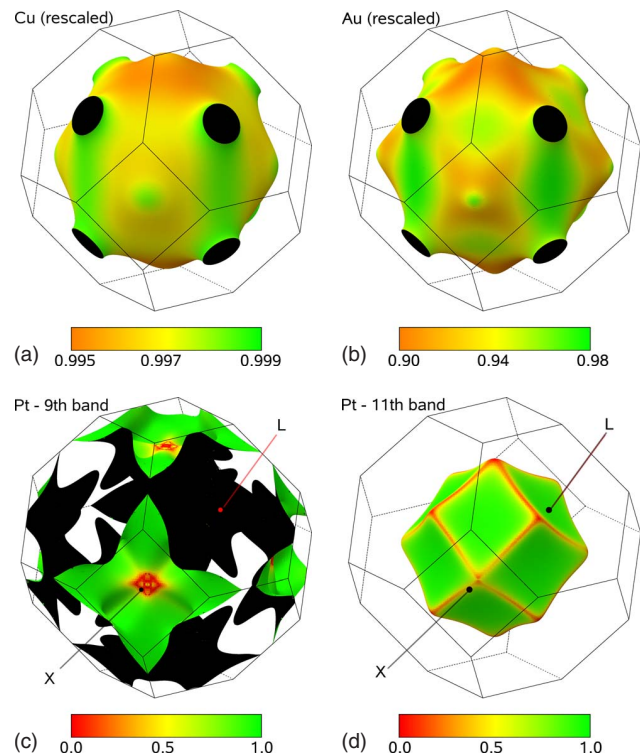


FIG. 4. (Color online) Calculated relativistic Fermi surface of Cu (upper left), Au (upper right), and Pt (lower left: ninth band and lower right: 11th band), and the expectation values of $\hat{\beta}\sigma_z$ for the $|\Psi_{\mathbf{k}}^{\pm}\rangle$ states are indicated as color code. Note the different scale for Cu and Au in comparison to Pt.

is shown. Pt, which is a polyvalent metal, exhibits a very strong influence of the spin-orbit coupling that can be seen from the shown bands with small spin polarization in large regions of \mathbf{k} space. All polarization values between 0 and +1 for the $|\Psi_{\mathbf{k}}^+\rangle$ states are obtained for Pt. The effect is much weaker for Cu and even for Au. Notice the different scales in Fig. 4. It is important to mention that the symmetry of the spin polarization P is lower than the symmetry of the Fermi surface. The spin degree of freedom is coupled to the lattice because of spin-orbit interaction. The operator $\hat{\beta}\sigma$ does not commute with the relativistic Hamiltonian of Eq. (2) and the chosen quantization axis is reflected in the symmetry. If the transformation is applied using the quantization axis along x , the pictures in Fig. 4 would be rotated by 90° around y axis.

There are two reasons why the influence of the spin-orbit coupling is increased. First, Au and Pt are heavier than Cu with atomic numbers of $Z=79$ and $Z=78$ in comparison to $Z=29$. Since the spin-orbit coupling strength is proportional to Z , the effect in Pt and Au is stronger. Second, the band structure affects directly the strength of the spin mixing. As it was discussed in Ref. 26, the spin polarization in regions where two bands are close to each other can be approximately written as $P = \Delta / \sqrt{\Delta^2 + 4V_{SO}^2}$. This expression is based on the consideration of a two-level system with the spin-orbit interaction as a perturbation, where Δ is a band separation and V_{SO} is some effective spin-orbit interaction. It is evident that for \mathbf{k} points with small energetic separation of a few bands, small spin polarizations are obtained. Especially, if certain \mathbf{k} points have degeneracy ($\Delta=0$) in the nonrelativistic case, the spin polarization vanishes for them.

For example, a degeneracy is lifted close to the Fermi energy at the X point of Pt (Fig. 2). This leads to the spin polarization P close to zero at the Fermi surface (Fig. 4, ninth band). The same holds for the L point of the 11th band (compare Figs. 2 and 4). In the literature other examples such as Al (Ref. 26) and Co (Ref. 27) are discussed with special emphasis on the influence on experimental results. Especially, spin-flip scattering rates can be strongly influenced by this effect.

The dominant bands for Fe in a relativistic calculation are shown in Fig. 5, where the spin polarization is given as color code. The calculated Fermi surface is in very good agreement to results of Wang *et al.*²⁴ We obtain the same bands (5–10) but only four bands (7–10) are shown here. Since only very small pockets are formed by the bands 5 and 6, they are skipped for further discussion. From the picture of spin polarization, one can see that the ninth band is dominated by electrons with $\langle \hat{\beta}\sigma_z \rangle \approx 1$ and the tenth band by $\langle \hat{\beta}\sigma_z \rangle \approx -1$ only. This is obvious from a comparison to the Fermi surface of a nonrelativistic calculation shown in Fig. 6. The sixth band of the majority electrons is definitely related to the ninth band of the relativistic calculation. The same holds for the fourth minority band in Fig. 6 and the tenth band in Fig. 5. Since Fe is still a relatively light element, the relativistic treatment gives absolute values of the spin polarization close to the one (namely, $P=1$) obtained by the nonrelativistic approach with well-defined spin-up and spin-down states. For the bands 7 and 8 the result is different since they are mixtures of the fifth majority and the third

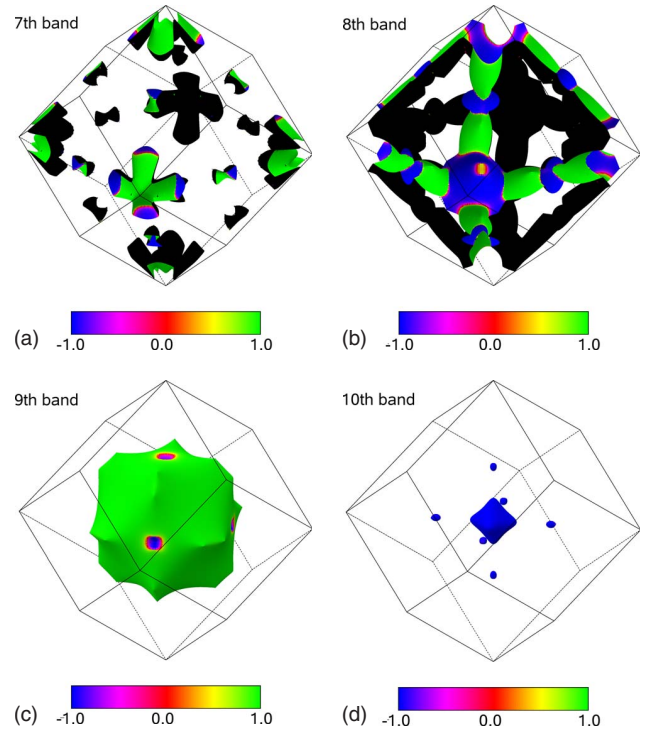


FIG. 5. (Color online) Calculated relativistic Fermi surface for the bands 7–10 of bcc Fe. The expectation values of the $\hat{\beta}\sigma_z$ operator are given as color code.

minority band. In a nonrelativistic calculation both bands are well separated by the spin quantum number. Including relativistic effects, the spin is not any more conserved and the bands intermix. It is an important change that should influ-

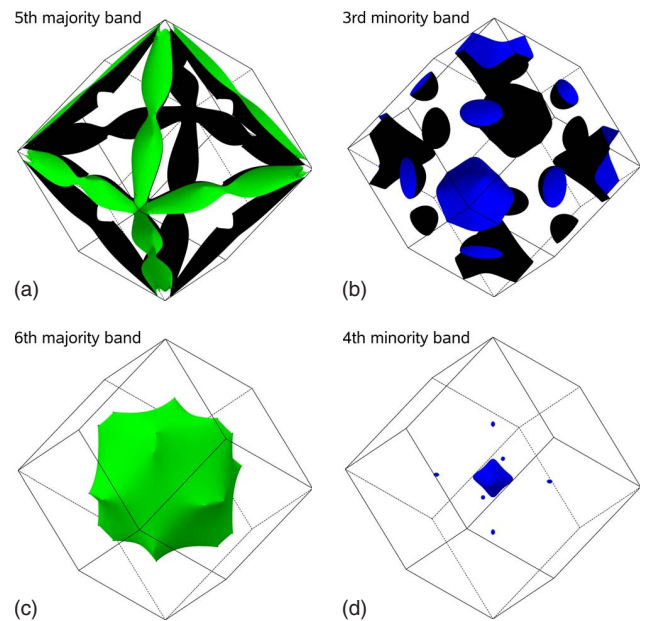


FIG. 6. (Color online) Calculated nonrelativistic Fermi surface of bcc Fe (upper left: fifth majority band, upper right: third minority, lower left: sixth majority band, and lower right: fourth minority band).

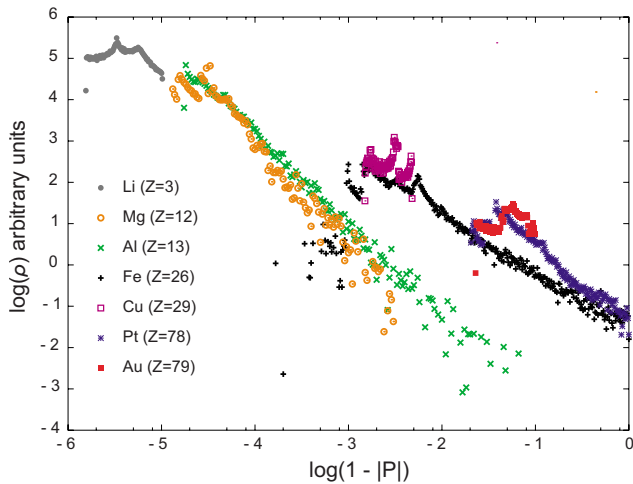


FIG. 7. (Color online) A histogram $\rho(P)$ of calculated spin mixing parameters $1 - |P_k|$ on the Fermi surface of different metals on a double-logarithmic scale. Fabian and Das Sarma (Ref. 26) found for Al the same dependency by treating the spin-orbit coupling as perturbation. Lattice constants are taken from experiment: Li(bcc, $a = 3.509$ Å), Mg(hex, $a = 3.210$ Å), Al(fcc, $a = 4.050$ Å), Fe(bcc, $a = 2.867$ Å), Cu(fcc, $a = 3.614$ Å), Pt(fcc, $a = 3.924$ Å), and Au(fcc, $a = 4.078$ Å). For Mg it was necessary to take a relaxed c/a ratio of 1.48 since in this system c/a is crucial to obtain the spin hot spots.

ence spin sensitive measurements. Values close to zero are obtained in small regions where the spin polarization changes sign. These states are complete mixtures of spin-up and spin-down states. For special symmetry lines this effect was discussed by Ackermann *et al.*⁴⁹ They have found the transition from spin-expectation value $\langle \hat{\beta}\sigma_z \rangle \approx 1$ to $\langle \hat{\beta}\sigma_z \rangle \approx -1$ at anticrossing points in Γ -H direction of Fe. However, their discussion was not focused on the \mathbf{k} points at the Fermi level which are the important states for the spin-dependent electronic transport.

To compare the effect of the spin-orbit coupling in different materials, a histogram of the k -dependent spin-mixing parameter $(1 - |P_k|)$ is shown in Fig. 7 [$\rho(P)$ is the probability to find states at the Fermi level with the polarization P] for Li, Mg, Al, Fe, Cu, Pt, and Au. Here we introduce k as a combined index for the band number n and the crystal momentum \mathbf{k} . Li, Cu, and Au are examples with only one band at the Fermi level far from points of degeneracy. The distributions of $\rho(P)$ are very narrow for these three materials and mainly shifted by the difference in the atomic number. In contrast, the distributions for Mg, Al, Fe, and Pt are very broad with a linear slope in the double-logarithmic plot. In the case of the light elements Mg and Al, spin-mixing parameters comparable to Cu are possible. It has two reasons as explained by Fabian and Das Sarma.²⁶ First, Fermi-surface sheets are close to the Brillouin-zone boundaries that increases the spin mixing. Second, it is due to the crossing of bands (accidental degeneracy) at the Fermi level which leads to an increase in the spin-orbit coupling strength. As shown in Ref. 26 spin-mixing parameters up to unity can be resolved, if a very fine \mathbf{k} mesh is used around the hot spots where the degeneracy is lifted. However, these points are statistically irrelevant and do not contribute significantly to

TABLE I. Averaged spin mixing parameter $\langle 1 - |P_k| \rangle_k$ for different metals (scaled by a factor of 10^3).

Li	Mg	Al	Fe	Cu	Pt	Au
0.005	0.049	0.083	49	3	118	60

Fermi-surface averages. The slope of the probability amplitude $\rho(P)$ with the long tail is similar for Al and Mg and can explain a special behavior of Al and Mg in conduction electron-spin-resonance experiments.²⁶ For the understanding it is instructive to compare also Cu with Fe and Au with Pt. In both cases the atomic number Z is very similar for the two compared materials. Due to the multisheeted Fermi surface of Fe and Pt with several lifted degeneracies, the spin mixing parameter is strongly enhanced and the distribution is broadened. This result shows that for Fe similar effects as discussed for Co by Pickel *et al.*²⁷ should be measurable. They found that the spin hot spots increase the spin-relaxation process drastically.

Figure 7 reflects perfectly the situation with the assumption of well-defined spin-up and spin-down states. For light elements with a simple Fermi surface such as Li, the assumption works fine. That is quite reasonable even for Cu. In contrast, it is already questionable to assume well-defined spin states in the case of heavy materials such as Pt or polyvalent light materials such as Al. The averaged spin-mixing parameters are summarized in Table I. For Fe and Cu, the elements with comparable atomic numbers, the averaged spin mixing parameters differ by a factor of 10. It is caused by the avoided crossings of bands in Fe. For Pt and Au a similar behavior is obvious. The present results for the averaged spin mixing parameters of Fe, Cu, and Au are in good agreement with similar calculations published recently.²⁸

IV. CONCLUSION

We present the implementation of relativistic band structure, Fermi surface, and wave-function calculations in the relativistic screened KKR method. By means of these quantities, the spin polarization on the Fermi surface of several metals is discussed. Such information is important for a theoretical analysis of spin and electronic transports. It is shown that for monovalent metals such as Li, Cu, and Au, the “up” and “down” spin-polarized states are well defined for all \mathbf{k} points on the Fermi surface. Whereas for polyvalent materials such as Mg, Al, Fe, and Pt, electron states with zero spin polarization exist. The effect is drastic in the case of heavy elements where large regions with vanishing spin polarization exist. As an additional mechanism, spin hot spots occur for magnetic materials such as Fe at the avoided crossing points of the exchange-split bands. For such materials it can be essential to take relativistic effects into account for a proper description of spin-dependent phenomena. In addition, an appropriate method to treat the spin polarization of degenerate bands in nonmagnetic materials is proposed.

ACKNOWLEDGMENTS

This work was partially supported by the Deutsche

Forschungsgemeinschaft (SFB 762). M. Gradhand is a member of the International Max Planck Research School for Science and Technology of Nanostructures.

APPENDIX: TRANSFORMATION TO A GLOBAL QUANTIZATION AXIS

In order to apply the transformation given by Eqs. (9) and (10), we need to calculate matrix elements such as

$$\begin{aligned}
& \langle \Psi_{n\mathbf{k}} | \hat{\beta} \sigma_z | \Psi_{n'\mathbf{k}} \rangle \\
&= - \sum_{\kappa' \mu'} \sum_{\kappa'' \mu''} a_{\kappa' \mu'}^{n*}(\mathbf{k}) a_{\kappa'' \mu''}^{n'}(\mathbf{k}) \\
& \times \sum_{\kappa \mu} \left\{ \left(\frac{2\mu}{2\kappa+1} \right) \int g_{\kappa \mu; \kappa' \mu'}^*(r) g_{\kappa \mu; \kappa'' \mu''}(r) r^2 dr \right. \\
& + \frac{2\mu}{2\kappa-1} \int f_{\kappa \mu; \kappa' \mu'}^*(r) f_{\kappa \mu; \kappa'' \mu''}(r) r^2 dr \\
& + \sqrt{1 - \left(\frac{2\mu}{2\kappa+1} \right)^2} \int g_{\kappa \mu; \kappa' \mu'}^*(r) g_{-\kappa-1, \mu; \kappa'' \mu''}(r) r^2 dr \\
& \left. - \sqrt{1 - \left(\frac{2\mu}{2\kappa-1} \right)^2} \int f_{\kappa \mu; \kappa' \mu'}^*(r) f_{-\kappa+1, \mu; \kappa'' \mu''}(r) r^2 dr \right\}, \tag{A1}
\end{aligned}$$

$$\begin{aligned}
& \langle \Psi_{n\mathbf{k}} | \hat{\beta} \sigma_+ | \Psi_{n'\mathbf{k}} \rangle \\
&= - \sum_{\kappa' \mu'} \sum_{\kappa'' \mu''} a_{\kappa' \mu'}^{n*}(\mathbf{k}) a_{\kappa'' \mu''}^{n'}(\mathbf{k}) \sum_{\kappa \mu} \left\{ \sqrt{\kappa^2 - 1/4 - \mu(\mu-1)} \right. \\
& \times \left[\frac{2}{2\kappa+1} \int g_{\kappa \mu; \kappa' \mu'}^*(r) g_{\kappa \mu-1; \kappa'' \mu''}(r) r^2 dr \right. \\
& \left. + \frac{2}{2\kappa-1} \int f_{\kappa \mu; \kappa' \mu'}^*(r) f_{\kappa \mu-1; \kappa'' \mu''}(r) r^2 dr \right] \\
& + \frac{\sqrt{(2\kappa+1-2\mu)(2\kappa+3-2\mu)}}{2\kappa+1} \\
& \times \int g_{\kappa \mu; \kappa' \mu'}^*(r) g_{-\kappa-1, \mu-1; \kappa'' \mu''}(r) r^2 dr \\
& + \frac{\sqrt{(2\kappa-1+2\mu)(2\kappa-3+2\mu)}}{2\kappa-1} \\
& \left. \times \int f_{\kappa \mu; \kappa' \mu'}^*(r) f_{-\kappa+1, \mu-1; \kappa'' \mu''}(r) r^2 dr \right\}, \tag{A2}
\end{aligned}$$

and

$$\begin{aligned}
& \langle \Psi_{n\mathbf{k}} | \hat{\beta} \sigma_- | \Psi_{n'\mathbf{k}} \rangle \\
&= - \sum_{\kappa' \mu'} \sum_{\kappa'' \mu''} a_{\kappa' \mu'}^{n*}(\mathbf{k}) a_{\kappa'' \mu''}^{n'}(\mathbf{k}) \sum_{\kappa \mu} \\
& \times \left\{ \sqrt{\kappa^2 - 1/4 - \mu(\mu+1)} \right. \\
& \times \left[\frac{2}{2\kappa+1} \int g_{\kappa \mu; \kappa' \mu'}^*(r) g_{\kappa \mu+1; \kappa'' \mu''}(r) r^2 dr \right. \\
& \left. + \frac{2}{2\kappa-1} \int f_{\kappa \mu; \kappa' \mu'}^*(r) f_{\kappa \mu+1; \kappa'' \mu''}(r) r^2 dr \right] \\
& - \frac{\sqrt{(2\kappa+1+2\mu)(2\kappa+3+2\mu)}}{2\kappa+1} \\
& \times \int g_{\kappa \mu; \kappa' \mu'}^*(r) g_{-\kappa-1, \mu+1; \kappa'' \mu''}(r) r^2 dr \\
& - \frac{\sqrt{(2\kappa-1-2\mu)(2\kappa-3-2\mu)}}{2\kappa-1} \\
& \left. \times \int f_{\kappa \mu; \kappa' \mu'}^*(r) f_{-\kappa+1, \mu+1; \kappa'' \mu''}(r) r^2 dr \right\}. \tag{A3}
\end{aligned}$$

The expressions above are written in a general form valid for nonmagnetic as well as magnetic systems. Actually, in the nonmagnetic case, they can be simplified due to the dependence of the radial solutions on κ only.³⁸ Thus, with $n'=n$ in Eq. ((A1), we have the expression for the spin polarization used in our calculations.

The implementation of the ladder operators $\sigma_+ = \sigma_x + i\sigma_y$ and $\sigma_- = \sigma_x - i\sigma_y$ in Eqs. ((A2) and (A3) provides us an easier way for dealing with the conditions given by Eq. (10). Finally, we can write the coefficients of the transformation in Eqs. (9) and (10) in the following form:

$$c_1 = \frac{1}{\sqrt{2}} \sqrt{1 + \frac{|a|}{\sqrt{|a|^2 + 4|d|^2}}} \tag{A4}$$

and

$$c_2 = - \left(\frac{|a|}{a} \right) \frac{d\sqrt{2}}{\sqrt{|a|^2 + 4|d|^2 + |a|\sqrt{|a|^2 + 4|d|^2}}}, \tag{A5}$$

where the parameters a and d are given by

$$a = 2i \operatorname{Im} \{ \langle \Psi_k^1 | \hat{\beta} \sigma_y | \Psi_k^2 \rangle \langle \Psi_k^2 | \hat{\beta} \sigma_x | \Psi_k^1 \rangle \} \tag{A6}$$

and

$$d = \langle \Psi_k^2 | \hat{\beta} \sigma_x | \Psi_k^1 \rangle \langle \Psi_k^1 | \hat{\beta} \sigma_y | \Psi_k^1 \rangle - \langle \Psi_k^2 | \hat{\beta} \sigma_y | \Psi_k^1 \rangle \langle \Psi_k^1 | \hat{\beta} \sigma_x | \Psi_k^1 \rangle. \tag{A7}$$

Here we use $c_1 = |c_1|$ as the choice of an arbitrary phase, which does not influence the results.

*martin.gradhand@physik.uni-halle.de

- ¹F. J. Jedema, A. T. Filip, and B. J. van Wees, *Nature* (London) **410**, 345 (2001).
- ²H. Kurt, R. Loloee, K. Eid, W. P. Pratt, J. Bass, and J. Bass, *Appl. Phys. Lett.* **81**, 4787 (2002).
- ³S. O. Valenzuela and M. Tinkham, *Nature* **442**, 176 (2006).
- ⁴L. Vila, T. Kimura, and Y. C. Otani, *Phys. Rev. Lett.* **99**, 226604 (2007).
- ⁵T. Seki, Y. Hasegawa, S. Mitani, S. Takahashi, H. Imamura, S. Maekawa, J. Nitta, and K. Takanashi, *Nature Mater.* **7**, 125 (2008).
- ⁶T. Yang, T. Kimura, and Y. Otani, *Nat. Phys.* **4**, 851 (2008).
- ⁷M. N. Baibich, J. M. Broto, A. Fert, F. Nguyen Van Dau, F. Petroff, P. Etienne, G. Creuzet, A. Friederich, and J. Chazelas, *Phys. Rev. Lett.* **61**, 2472 (1988).
- ⁸G. Binasch, P. Grünberg, F. Saurenbach, and W. Zinn, *Phys. Rev. B* **39**, 4828 (1989).
- ⁹M. Julliere, *Phys. Lett. A* **54**, 225 (1975).
- ¹⁰J. S. Moodera, L. R. Kinder, T. M. Wong, and R. Meservey, *Phys. Rev. Lett.* **74**, 3273 (1995).
- ¹¹T. S. Plaskett, P. P. Freitas, N. P. Barradas, M. F. da Silva, and J. C. Soares, *J. Appl. Phys.* **76**, 6104 (1994).
- ¹²S. Yuasa, T. Nagahama, A. Fukushima, Y. Suzuki, and K. Ando, *Nature Mater.* **3**, 868 (2004).
- ¹³J. Slonczewski, *J. Magn. Magn. Mater.* **159**, L1 (1996).
- ¹⁴M. Tsoi, A. G. M. Jansen, J. Bass, W.-C. Chiang, M. Seck, V. Tsoi, and P. Wyder, *Phys. Rev. Lett.* **80**, 4281 (1998).
- ¹⁵E. B. Myers, D. C. Ralph, J. A. Katine, R. N. Louie, and R. A. Buhrman, *Science* **285**, 867 (1999).
- ¹⁶J. A. Katine, F. J. Albert, R. A. Buhrman, E. B. Myers, and D. C. Ralph, *Phys. Rev. Lett.* **84**, 3149 (2000).
- ¹⁷M. I. Dyakonov and V. I. Perel, *JETP Lett.* **35A**, 459 (1971).
- ¹⁸Y. K. Kato, R. C. Myers, A. C. Gossard, and D. D. Awschalom, *Science* **306**, 1910 (2004).
- ¹⁹A. Crépieux and P. Bruno, *Phys. Rev. B* **64**, 014416 (2001).
- ²⁰T. Tanaka, H. Kontani, M. Naito, T. Naito, D. S. Hirashima, K. Yamada, and J. Inoue, *Phys. Rev. B* **77**, 165117 (2008).
- ²¹Y. Tian, L. Ye, and X. Jin, *Phys. Rev. Lett.* **103**, 087206 (2009).
- ²²T. Miyasato, N. Abe, T. Fujii, A. Asamitsu, S. Onoda, Y. Onose, N. Nagaosa, and Y. Tokura, *Phys. Rev. Lett.* **99**, 086602 (2007).
- ²³F. D. M. Haldane, *Phys. Rev. Lett.* **93**, 206602 (2004).
- ²⁴X. Wang, D. Vanderbilt, J. R. Yates, and I. Souza, *Phys. Rev. B* **76**, 195109 (2007).
- ²⁵N. Tombros, S. Tanabe, A. Veligura, C. Jozsa, M. Popinciuc, H. T. Jonkman, and B. J. van Wees, *Phys. Rev. Lett.* **101**, 046601 (2008).
- ²⁶J. Fabian and S. Das Sarma, *Phys. Rev. Lett.* **81**, 5624 (1998).
- ²⁷M. Pickel, A. B. Schmidt, F. Giesen, J. Braun, J. Minár, H. Ebert, M. Donath, and M. Weinelt, *Phys. Rev. Lett.* **101**, 066402 (2008).
- ²⁸D. Steiauf and M. Fähnle, *Phys. Rev. B* **79**, 140401(R) (2009).
- ²⁹S. Takada, *Prog. Theor. Phys.* **36**, 224 (1966).
- ³⁰Y. Onodera and M. Okazaki, *J. Phys. Soc. Jpn.* **21**, 1273 (1966).
- ³¹R. Feder, F. Rosicky, and B. Ackermann, *Z. Phys. B* **52**, 31 (1983).
- ³²P. Strange, R. Staunton, and B. L. Gyorffy, *J. Phys. C* **17**, 3355 (1984).
- ³³G. Schadler, P. Weinberger, A. M. Boring, and R. C. Albers, *Phys. Rev. B* **34**, 713 (1986).
- ³⁴S. A. Ostanin and V. P. Shirokovskii, *J. Phys.: Condens. Matter* **2**, 7585 (1990).
- ³⁵L. Szunyogh, B. Újfalussy, and P. Weinberger, *Phys. Rev. B* **51**, 9552 (1995).
- ³⁶P. Strange, *Relativistic Quantum Mechanics* (Cambridge University Press, Cambridge, England, 1998).
- ³⁷H. Ebert, *Electronic Structure and Physical Properties of Solids, Lecture Notes in Physics* (Springer, Berlin, 2000), Vol. 535, p. 191.
- ³⁸J. Zabloudil, R. Hammerling, L. Szunyogh, and P. Weinberger, *Electron Scattering in Solid Matter* (Springer-Verlag, Berlin, 2005).
- ³⁹R. Zeller, P. H. Dederichs, B. Újfalussy, L. Szunyogh, and P. Weinberger, *Phys. Rev. B* **52**, 8807 (1995).
- ⁴⁰N. Papanikolaou, R. Zeller, and P. H. Dederichs, *J. Phys.: Condens. Matter* **14**, 2799 (2002).
- ⁴¹S. H. Vosko, L. Wilk, and M. Nusair, *Can. J. Phys.* **58**, 1200 (1980).
- ⁴²H. Ebert, H. Freyer, A. Vernes, and G. Y. Guo, *Phys. Rev. B* **53**, 7721 (1996).
- ⁴³P. Zahn, Ph.D. thesis, Technische Universität Dresden, 1998.
- ⁴⁴R. J. Elliott, *Phys. Rev.* **96**, 266 (1954).
- ⁴⁵H. A. Kramers, *Proc. R. Acad. Sci. Amsterdam* **33**, 959 (1930).
- ⁴⁶S. Bei der Kellen and A. J. Freeman, *Phys. Rev. B* **54**, 11187 (1996).
- ⁴⁷P. Strange, H. Ebert, J. B. Staunton, and B. L. Gyorffy, *J. Phys.: Condens. Matter* **1**, 2959 (1989).
- ⁴⁸X. Wang, J. R. Yates, I. Souza, and D. Vanderbilt, *Phys. Rev. B* **74**, 195118 (2006).
- ⁴⁹B. Ackermann, R. Feder, and E. Tamura, *J. Phys. F: Met. Phys.* **14**, L173 (1984).

3.3 Fully relativistic *ab initio* treatment of spin-flip scattering caused by impurities

Fully relativistic *ab initio* treatment of spin-flip scattering caused by impurities

Martin Gradhand,^{1,2,*} Dmitry V. Fedorov,² Peter Zahn,² and Ingrid Mertig^{2,1}

¹Max-Planck-Institut für Mikrostrukturphysik, Weinberg 2, D-06120 Halle, Germany

²Institut für Physik, Martin-Luther-Universität Halle-Wittenberg, D-06099 Halle, Germany

(Received 8 October 2009; published 7 January 2010)

We present a fully relativistic approach for the first-principles calculation of the spin-relaxation time of conduction electrons caused by substitutional impurities. It is an extension of our previous nonrelativistic perturbative approach. The approach is based on a relativistic Korringa-Kohn-Rostoker Green's function and band-structure method. As an application, we obtain the spin-flip scattering time for a Cu host with different types of impurities. It is shown that the perturbative approach fails for impurities lighter than the host atoms, while the relativistic treatment provides good agreement with conduction-electron spin-resonance experiments for all considered impurities.

DOI: [10.1103/PhysRevB.81.020403](https://doi.org/10.1103/PhysRevB.81.020403)

PACS number(s): 71.15.Rf, 72.25.Rb, 76.30.-v, 85.75.-d

Spin relaxation becomes an increasingly important problem because of the progress in spintronics.¹⁻⁴ Since this process is connected with the spin-orbit interaction, an appropriate relativistic treatment is imperative. In particular, the microscopic understanding of the spin-relaxation anisotropy, which was found to be as large as 20% in graphene,⁵ requires a relativistic treatment.

One of the most important spin-relaxation mechanisms is the Elliott-Yafet mechanism.^{6,7} For this case, the spin relaxation can be described by a spin-flipping process. It is based on the fact that in the presence of spin-orbit interaction, the spin is not anymore a good quantum number and all electronic states are mixtures of pure “spin-up” and “spin-down” states. As a consequence, impurities, grain boundaries, interfaces, and phonons cause spin-flip scattering processes in addition to the usual momentum scattering.⁶⁻⁸ Spin-flip scattering can also be initiated by the spin-orbit interaction of impurities and by the phonon-modulated spin-orbit interaction of the lattice ions.^{8,9}

In our recent paper,¹⁰ we have shown that in certain situations spin-flip scattering caused by impurities can be properly described using the spin-flip transition matrix calculated in the Born approximation. The spin-orbit interaction was taken into account as an additional perturbation at the impurity site only. This approach is valid if spin-orbit interaction in the host material is negligible in comparison to the spin-orbit interaction at the impurity site.

In this Rapid Communication we present a fully relativistic treatment of the Elliott-Yafet mechanism based on the self-consistent solution of the Kohn-Sham-Dirac equation for the host as well as for the impurity problem. In other words, we extend our previous method for the calculation of the spin-flip scattering time¹⁰ to the fully relativistic case. The main point of interest is how to define spin-flip scattering since the spin is not anymore a conserved quantity. The relativistic spin operator $\hat{\beta}\hat{\sigma}$ does not commute with the Hamiltonian $\hat{H}(\mathbf{r})$ of the Kohn-Sham-Dirac equation (we restrict our consideration to a nonmagnetic system),

$$\hat{H}(\mathbf{r})\Psi_n(\mathbf{r}) = \left[\frac{\hbar}{i}c\hat{\alpha}\cdot\vec{\nabla}_r + \hat{\beta}mc^2 + I_4V(\mathbf{r}) \right] \Psi_n(\mathbf{r}). \quad (1)$$

For the solution of Eq. (1), the relativistic Korringa-Kohn-Rostoker method¹¹⁻¹⁵ is applied.¹⁶ We use spherical poten-

tials in the atomic sphere approximation (ASA),

$$V(\mathbf{r}) = \sum_j V_j(|\mathbf{r} - \mathbf{R}_j|), \quad \text{with } |\mathbf{r} - \mathbf{R}_j| \leq R_{ASA}^j. \quad (2)$$

Then the eigenfunctions of $\hat{H}(\mathbf{r})$ inside the j th ASA sphere can be written (for the case of a system with translational symmetry) in the following form:¹⁷

$$\Psi_{n\mathbf{k}}(\mathbf{r} + \mathbf{R}_j) = \sum_{\kappa\mu} a_{\kappa\mu}^{n,j}(\mathbf{k}) \begin{pmatrix} g_{\kappa}^j(r)\chi_{\kappa\mu}(\hat{\mathbf{r}}) \\ i f_{\kappa}^j(r)\chi_{-\kappa\mu}(\hat{\mathbf{r}}) \end{pmatrix}, \quad (3)$$

where $a_{\kappa\mu}^{n,j}(\mathbf{k})$ are the expansion coefficients given for each band n and momentum \mathbf{k} and the functions $g_{\kappa}^j(r)$ and $f_{\kappa}^j(r)$ are the so-called “large” and “small” components, respectively. In addition, $\chi_{\kappa\mu}(\hat{\mathbf{r}})$ denotes the relativistic spinor functions.^{17,18} The corresponding electron eigenvalues are $W_n(\mathbf{k}) = E_n(\mathbf{k}) + mc^2$, where $E_n(\mathbf{k})$ can be related to the nonrelativistic energy spectrum. All the wave functions given by Eq. (3) have a spin-mixed character, and one cannot use the language of the nonrelativistic treatment with well-defined spin-up and -down states anymore.

Let us consider the case of a nonmagnetic system with space-inversion symmetry. For each pair of degenerate states⁶ we can apply the transformation described in Ref. 16 to get two new states $\Psi_{n\mathbf{k}}^+(\mathbf{r})$ and $\Psi_{n\mathbf{k}}^-(\mathbf{r})$ with the spin polarization along a chosen quantization axis. Let us fix the quantization axis along the z direction. Then the superposition of the two original states has to fulfill the condition of zero expectation value for the operators $\hat{\beta}\sigma_x$ and $\hat{\beta}\sigma_y$. In combination with the orthonormalization condition the unitary transformation is defined uniquely at every \mathbf{k} point. Then, the spin polarization is defined as

$$P_{n\mathbf{k}} = \langle \Psi_{n\mathbf{k}}^+ | \hat{\beta}\sigma_z | \Psi_{n\mathbf{k}}^+ \rangle = - \langle \Psi_{n\mathbf{k}}^- | \hat{\beta}\sigma_z | \Psi_{n\mathbf{k}}^- \rangle. \quad (4)$$

In fact, it is a generalization of the procedure used in Ref. 19 to the case of the Dirac bispinor wave functions. Using such a definition of “+” and “-” states, we can introduce the relativistic spin-relaxation time T_1^k as (k is a shorthand notation for \mathbf{k} and n)

$$\frac{1}{T_1^k} = \frac{1}{\tau_k^{+-}} + \frac{1}{\tau_k^{-+}} = \sum_{k'} (P_{kk'}^{+-} + P_{kk'}^{-+}). \quad (5)$$

In the equation above, the spin-flip scattering times τ_k^{+-} and τ_k^{-+} are connected with the corresponding transition probabilities $P_{kk'}^{+-}$ and $P_{kk'}^{-+}$. They are calculated by Fermi's golden rule. For instance, the microscopic probability for a transition from a + state k into a - state k' is given by

$$P_{kk'}^{+-} = 2\pi c_0 N |T_{kk'}^{+-}|^2 \delta(E_k - E_{k'}). \quad (6)$$

Here and further on we use Rydberg atomic units. The linear dependence of $P_{kk'}^{+-}$ on the number of impurities $c_0 N$ (where c_0 is the impurity concentration and N is the number of atoms in the system) holds for dilute alloys. It is based on the assumption of noninteracting impurities. The corresponding spin-flip transition matrix $T_{kk'}^{+-}$ has to be calculated from the change in the potential $\Delta V(\mathbf{r})$ in the disturbed region around the impurity atom,^{20,21}

$$T_{kk'}^{+-} = \sum_j \int_{\Omega_{ASA}^j} d\mathbf{r} \Psi_{k'}^{-\dagger}(\mathbf{r} + \mathbf{R}_j) \Delta V_j(r) \Psi_k^+(\mathbf{r} + \mathbf{R}_j). \quad (7)$$

Here, the bispinor functions $\Psi_{k'}^-$ and Ψ_k^+ are unperturbed and perturbed wave functions, respectively. The disturbed region, where charge relaxation is allowed, is restricted in our calculations to a cluster of 55 atoms that corresponds to four nearest-neighbor shells around the substitutional impurity. Using Eq. (3), this expression simplifies to

$$T_{kk'}^{+-} = \sum_j \sum_{\kappa\mu} [\hat{a}_{\kappa\mu}^{-j}(k')]^* \Delta_{\kappa}^j a_{\kappa\mu}^{+j}(k), \quad (8)$$

where Δ_{κ}^j is given by

$$\Delta_{\kappa}^j = \int_0^{R_{ASA}^j} dr r^2 [\hat{g}_{\kappa}^{j*}(r) g_{\kappa}^j(r) + \hat{f}_{\kappa}^{j*}(r) f_{\kappa}^j(r)] \Delta V_j(r). \quad (9)$$

The averaged value over the Fermi surface is calculated via $1/T_1 = \langle 1/T_1^k \rangle_{E_k=E_F}$.^{21,22}

Actually, choosing the quantization axis in other directions (for instance, along $\langle 111 \rangle$ instead of $\langle 001 \rangle$ direction) should provide for T_1 different results. This effect is caused by the interaction between the spin and the lattice. Generally, a detailed analysis of the anisotropy of the spin-relaxation time with respect to the orientation of the quantization axis is very desirable. Here, we do not concentrate on this point since we expect that the effect should be small for a Cu host.

The most important advantage of our relativistic approach is the consideration of the spin-orbit interaction of the host material. For comparison a method without this influence is introduced in addition. As it was discussed in our previous paper,¹⁰ the spin-relaxation time is related to the spin-flip scattering cross section $\sigma_{sf} = \Omega_{ws}/v_F 2T_1 c_0$, where Ω_{ws} is the volume of the Wigner-Seitz cell and v_F denotes the Fermi velocity. Within a spherical band approximation, the scattering cross section can be expressed in terms of differences of the phase shifts δ_j for the levels $j = l \pm 1/2$ of an impurity,^{23,24}

TABLE I. Spin-relaxation time T_1 in bulk Cu with an impurity concentration of 1 at. %. The experimental results for T_1 were derived from the data for the linewidth of the CESR signal ΔH in Tables III and IV of Ref. 25. The results of the nonrelativistic approach are from Ref. 10. All values are given in ps.

Impurity	Perturbative approach ^b		Our results (relativistic)	
	CESR ^a	T_1	From Eq. (5)	From Eq. (10)
Li	44 ± 10	2.8 × 10 ⁷	19	3.2 × 10 ⁷
Ti	4.2 ± 0.5	18	2.8	9.1
Ni	2.2 ± 0.2	1.6	3.2	3.9
Zn	64 ± 9	49	31	41
Ga	30 ± 4	22	16	16
Ge	14 ± 2	10	9.6	7.1
As	8.6 ± 0.7	5.7	5.4	4.6
Au	0.62 ± 0.21	0.56	0.47	0.38

^aReference 25.

^bReference 10.

$$\sigma_{sf} = \frac{2}{3} \frac{4\pi}{v_F} \sum_{l>0} \frac{l(l+1)}{2l+1} \sin^2[\delta_{l+1/2}(E_F) - \delta_{l-1/2}(E_F)]. \quad (10)$$

Here, the relativistic phase shifts at the impurity site are used but the spin-orbit coupling of the host is neglected.

Table I shows the spin-relaxation time T_1 for different impurities in a Cu host calculated using Eq. (5) as well as Eq. (10) in comparison to conduction-electron spin-resonance (CESR) experiments.²⁵ For all impurities we have a reasonable agreement with experimental data. For the heavier impurities — Ni, Zn, Ga, Ge, As, and Au — our previous nonrelativistic perturbative approach¹⁰ works also well. For impurities with a weaker spin-orbit interaction in comparison to a Cu host (Li and Ti), the fully relativistic description is mandatory to describe the spin-relaxation process properly. The reason is that in our previous method we neglected the spin-orbit coupling in the host, which becomes increasingly important when the impurity atom is lighter in comparison to the host material. In the present approach, the spin-orbit coupling of the host as well as of the impurities is completely taken into account via the relativistic wave functions.

The values of T_1 obtained using Eq. (10) mostly reproduce the results of the perturbative approach and the experimental situation. However, for Li the spin-relaxation time calculated from the phase shifts cannot describe the experimental data. This is evident since the phase shifts account for the spin-orbit coupling at the impurity site only. The atomic number of Li is small and the spin-orbit coupling is negligible. A spin-flip process is only possible if the incoming wave function is already a superposition of spin-up and

-down states. A relatively light impurity, like Li, acts just as a momentum scattering center. The spin relaxation is only provided by the mixed spin character of the Bloch wave function.⁶

This can be seen from the structure of the transition matrix in Eq. (7). The perturbation is just given by the difference of the potential. The action of spin-orbit coupling is hidden in the superposition of spin states of the unperturbed and perturbed wave functions. If the impurity atom is quite light, the spin mixing of the perturbed and unperturbed wave functions is comparable and determined by the spin-orbit coupling of the host material.

It is obvious for Li. For Ti in Cu we have an intermediate situation where both atoms have comparable spin-orbit coupling strengths. In such a case, both contributions, from the host and the impurity site, are important. For all other considered elements the spin-orbit interaction of the impurity atom dominates the relaxation process. It is evident from a comparison to the results calculated using Eq. (10).

Another way of visualizing the influence of unperturbed and perturbed wave functions is to discuss the anisotropic distribution of T_1^k over the Fermi surface shown in Fig. 1. As mentioned in Ref. 10, Ga is mainly a p scatterer, and Ni is mainly a d scatterer. Here, Li is comparable to Zn, which is mainly an s scatterer.¹⁰ This can be seen from the left column of Fig. 1, where the momentum relaxation time is shown. The largest τ_k values are obtained for states k where the corresponding s , p , or d angular momentum character of the host wave function is small.^{10,26}

The right-hand side of Fig. 1 shows the spin-relaxation time T_1^k . General features of the distributions over the Fermi surface are similar for all impurities considered, although the absolute values differ substantially. This result is different from the one obtained by the treatment of the spin-orbit coupling as a perturbation at the impurity site only.¹⁰ Under the previous approximation, Zn (s scatterer) and Ga (p scatterer) had similar distributions over the Fermi surface, but Ni (d scatterer) behaved completely different. This was due to the fact that s electrons are not affected by the spin-orbit interaction and for both, Zn and Ga, impurities only p electrons were scattered. The distributions of T_1^k were only determined by the orbital character of the electrons in a Cu host and the impurity atom.¹⁰ Here, we have taken into account the spin-mixed character of the unperturbed wave functions, which is visible in the distribution of the spin-relaxation time. The purple regions with small values of the spin-relaxation time mean strong scattering and coincide with regions of strong spin mixing in Cu.¹⁶ The green, yellow, and red regions are related to the wave functions with small spin mixing and correspondingly weak spin-flip scattering.

In addition, the angular momentum character of the wave functions in a Cu host is important to understand the red regions in the distributions of the spin-relaxation time. For Ga and Li, which are p scatterers, since s states do not contribute to the spin relaxation, the red areas are related to the minimal p character of the electronic states in Cu.^{10,26} For Ni impurities the red circles are due to small d character of the electronic states in the host.

In summary, we present a fully relativistic *ab initio* ap-

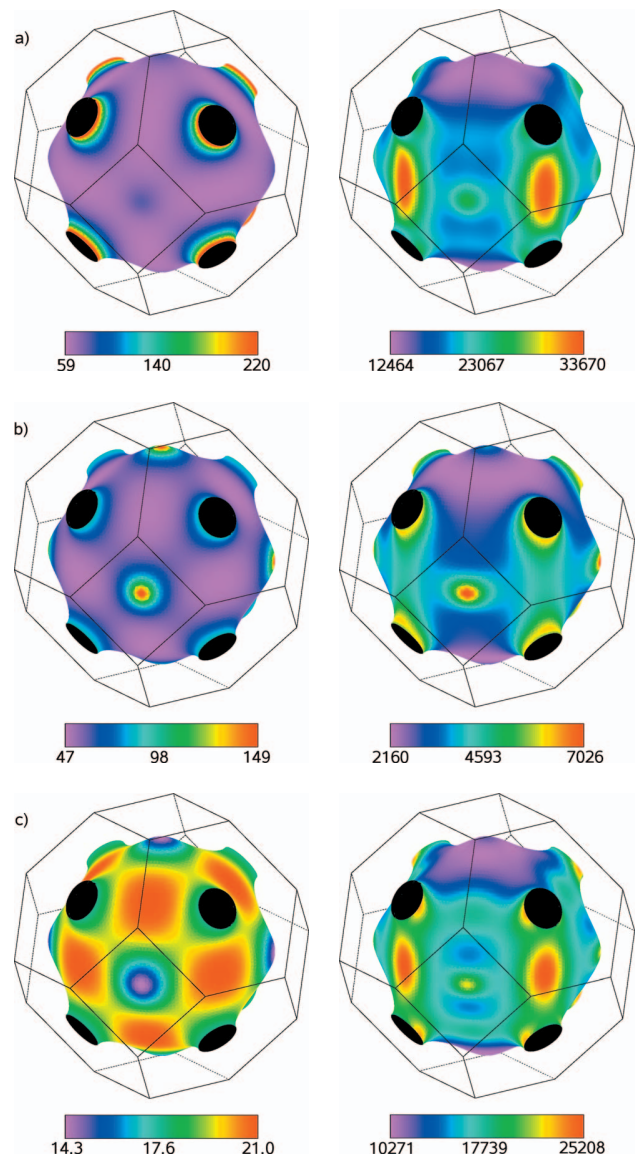


FIG. 1. (Color) Anisotropic $\tau_k=2(1/\tau_k^{++}+1/\tau_k^{--})^{-1}$ (left) and T_1^k (right) on the Fermi surface of Cu for (a) Li, (b) Ni, and (c) Ga impurities with a defect concentration of 1 at. %. All results are given in fs.

proach for investigations of the spin relaxation caused by substitutional defects. The results obtained for a Cu host are in good agreement with CESR experiments. In particular, they demonstrate that a fully relativistic treatment is needed for a proper description of spin-flip scattering caused by light impurities with a weak spin-orbit interaction in comparison to the host. We discuss the different contributions of unperturbed and perturbed wave functions to the spin-relaxation time for light as well as heavy impurities. For defects such as Ni, Au, and Zn, the spin-orbit coupling in a Cu host could be neglected, but for Li it is essential to describe the situation properly. In addition, we discuss the anisotropic distribution of the scattering times over the Fermi surface of Cu. We

show that all main features can be explained by the orbital and the spin-mixing characters of the wave functions in a Cu host in combination with the orbital angular momentum character of the impurity atom. The method presented in this Rapid Communication can be applied for a theoretical study of the Elliott-Yafet spin-relaxation mechanism caused by

impurities in all nonmagnetic materials with space-inversion symmetry.

This work was supported by the Deutsche Forschungsgemeinschaft (SFB 762) and the International Max Planck Research School for Science and Technology.

*martin.gradhand@physik.uni-halle.de

¹*Semiconductor Spintronics and Quantum Computation*, edited by D. D. Awschalom, D. Loss, and N. Samarth (Springer-Verlag, Berlin, 2002).

²G. A. Prinz, *Science* **282**, 1660 (1998).

³S. A. Wolf, D. D. Awschalom, R. A. Buhrman, J. M. Daughton, S. von Molnár, M. L. Roukes, A. Y. Chtchelkanova, and D. M. Treger, *Science* **294**, 1488 (2001).

⁴F. J. Jedema, A. T. Filip, and B. J. van Wees, *Nature (London)* **410**, 345 (2001).

⁵N. Tombros, S. Tanabe, A. Veligura, C. Jozsa, M. Popinciuc, H. T. Jonkman, and B. J. van Wees, *Phys. Rev. Lett.* **101**, 046601 (2008).

⁶R. J. Elliott, *Phys. Rev.* **96**, 266 (1954).

⁷Y. Yafet, *Solid State Physics* (Academic Press, New York, 1963), Vol. 14, pp. 1–98.

⁸J. Fabian and S. D. Sarma, *J. Vac. Sci. Technol. B* **17**, 1708 (1999).

⁹A. W. Overhauser, *Phys. Rev.* **89**, 689 (1953).

¹⁰D. V. Fedorov, P. Zahn, M. Gradhand, and I. Mertig, *Phys. Rev. B* **77**, 092406 (2008).

¹¹S. Takada, *Prog. Theor. Phys.* **36**, 224 (1966).

¹²Y. Onodera and M. Okazaki, *J. Phys. Soc. Jpn.* **21**, 1273 (1966).

¹³R. Feder, F. Rosicky, and B. Ackermann, *Z. Phys. B: Condens. Matter* **52**, 31 (1983).

¹⁴P. Strange, J. B. Staunton, and B. L. Gyorffy, *J. Phys. C* **17**, 3355 (1984).

¹⁵P. Strange, H. Ebert, J. B. Staunton, and B. L. Gyorffy, *J. Phys.: Condens. Matter* **1**, 2959 (1989).

¹⁶M. Gradhand, M. Czerner, D. V. Fedorov, B. Y. Yavorsky, L. Szunyogh, P. Zahn, and I. Mertig, *Phys. Rev. B* **80**, 224413 (2009).

¹⁷J. Zabloudil, R. Hammerling, L. Szunyogh, and P. Weinberger, *Electron Scattering in Solid Matter* (Springer Verlag, Berlin, 2005).

¹⁸M. E. Rose, *Relativistic Electron Theory* (John Wiley & Sons Inc., New York, 1961).

¹⁹J. Fabian and S. D. Sarma, *Phys. Rev. Lett.* **81**, 5624 (1998).

²⁰M. L. Goldberger and K. M. Watson, *Collision Theory* (Wiley, New York, 1964).

²¹N. A. W. Holzwarth and M. J. G. Lee, *Phys. Rev. B* **13**, 2331 (1976).

²²J. R. Asik, M. A. Ball, and C. P. Slichter, *Phys. Rev. Lett.* **16**, 740 (1966).

²³Y. Yafet, *J. Appl. Phys.* **39**, 853 (1968).

²⁴N. Papanikolaou, N. Stefanou, P. H. Dederichs, S. Geier, and G. Bergmann, *Phys. Rev. Lett.* **69**, 2110 (1992).

²⁵P. Monod and S. Schultz, *J. Phys. (Paris)* **43**, 393 (1982).

²⁶I. Mertig, *Rep. Prog. Phys.* **62**, 237 (1999).

3.4 Extrinsic Spin Hall Effect from First Principles

Extrinsic Spin Hall Effect from First Principles

Martin Gradhand,^{1,2,*} Dmitry V. Fedorov,² Peter Zahn,² and Ingrid Mertig^{2,1}

¹Max-Planck-Institut für Mikrostrukturphysik, Weinberg 2, D-06120 Halle, Germany

²Institut für Physik, Martin-Luther-Universität Halle-Wittenberg, D-06099 Halle, Germany

(Received 4 December 2009; published 6 May 2010)

We present an *ab initio* description of the spin Hall effect in metals. Our approach is based on density functional theory in the framework of a fully relativistic Korringa-Kohn-Rostoker method and the solution of a linearized Boltzmann equation including the scattering-in term (vertex corrections). The skew scattering mechanism at substitutional impurities is considered. Spin-orbit coupling in the host as well as at the impurity atom and the influence of spin-flip processes are fully taken into account. A sign change of the spin Hall effect in Cu and Au hosts is obtained as a function of the impurity atom, and even light elements like Li can cause a strong effect. It is shown that the *gigantic* spin Hall effect in Au can be caused by skew scattering at C and N impurities which are typical contaminations in a vacuum chamber.

DOI: 10.1103/PhysRevLett.104.186403

PACS numbers: 71.15.Rf, 72.25.Ba, 75.76.+j, 85.75.-d

During recent years the spin Hall effect (SHE) has attracted a lot of interest caused by its potential to generate spin currents in nonmagnetic materials. It would allow for spintronic devices without the problem of spin injection from a ferromagnet into a nonmagnet. Besides this technological aspect, the microscopic understanding of the effect is of great interest, since it has the same origin as the anomalous Hall effect (AHE). A proper description of the SHE provides the possibility of an extension of the method to magnetic materials and a treatment of the anomalous Hall effect.

After the first proposal of skew scattering [1,2] and the following detailed discussion of the extrinsic SHE by Dyakonov and Perel [3], a possible experimental setup was suggested by Hirsch [4]. Several mechanisms were found to contribute to the SHE and AHE [5–12]. These were the intrinsic contribution described by the Berry curvature [5,11], and the extrinsic contribution where the side jump mechanism [8,9] and skew scattering [6,7] at defects can be distinguished [10,12]. The intrinsic part of the SHE was already calculated for metallic systems by *ab initio* methods [13]. Whereas the extrinsic part, in particular the skew scattering, will be the subject of this Letter.

The SHE was first demonstrated optically in semiconductors [14], and only later were electrical measurements on metallic devices [15–17] performed. These experiments on Al, Cu, Pt, and Au provide a variety of results which can only partly be explained by the intrinsic mechanism [13,18]. Unfortunately, no reliable information is available about defects in the samples under consideration, which makes a comparison between experiment and theory difficult.

Here the extrinsic mechanism caused by the skew scattering at substitutional impurities is considered. Our calculations give an insight into the microscopic mechanism and we propose another explanation for the *gigantic* SHE

observed in Au [17], besides a Kondo resonance at Fe impurities [18].

In the first part of the Letter we introduce the approach based on the Korringa-Kohn-Rostoker method and the solution of the linearized Boltzmann equation. Our main focus is the Boltzmann equation since the band structure calculation was mainly described in Refs. [19,20]. Afterwards, first results of the approach are discussed.

For the description of the transport properties we choose the Boltzmann equation which is well suited to describe dilute alloys and allows for separation of the different microscopic mechanisms contributing to the Hall current. The nonequilibrium distribution function $f^n(\mathbf{k}) = f_0^n(\mathbf{k}) + g^n(\mathbf{k})$ of the considered system is separated into the equilibrium function $f_0^n(\mathbf{k})$ and $g^n(\mathbf{k})$ the responder of the system to the perturbation. These functions depend on the crystal momentum \mathbf{k} and the band index n . According to Kohn and Luttinger [21,22], the Boltzmann equation for a homogeneous system

$$\dot{\mathbf{k}} \cdot \nabla_{\mathbf{k}} f_0^n(\mathbf{k}) = \sum_{\mathbf{k}'} [P_{\mathbf{k}'\mathbf{k}}^{n'n} g^{n'}(\mathbf{k}') - P_{\mathbf{k}\mathbf{k}'}^{n'n} g^n(\mathbf{k})] \quad (1)$$

is given by the force term (l.h.s.) and the collision term (r.h.s.). A crucial point for the skew scattering mechanism is the fact that in the presence of spin-orbit interaction the microscopic reversibility is not any more valid for the scattering probability ($P_{\mathbf{k}\mathbf{k}'}^{n'n} \neq P_{\mathbf{k}'\mathbf{k}}^{n'n}$), although the systems under consideration are space-inversion invariant ($P_{\mathbf{k}\mathbf{k}'}^{n'n} = P_{-\mathbf{k},-\mathbf{k}'}^{n'n}$) [2]. The electrons are driven by an applied electric field $\dot{\mathbf{k}} = -e\mathbf{E}$ ($e > 0$) and the system is forced to a steady state by the collision term. This term is calculated in the dilute limit of impurity concentrations ($c_0 N$ —number of impurities) from Fermi's golden rule [20,23]

$$P_{\mathbf{k}\mathbf{k}'}^{n'n} = \frac{2\pi}{\hbar} c_0 N |T_{\mathbf{k}\mathbf{k}'}^{n'n}|^2 \delta(E_{\mathbf{k}}^n - E_{\mathbf{k}'}^{n'}). \quad (2)$$

The transition matrix in the atomic sphere approximation is given by [20]

$$T_{\mathbf{k}\mathbf{k}'}^{nn'} = \sum_j \int_{\Omega_{ASA}^j} d\mathbf{r} \Psi_{\mathbf{k}'}^{n'\dagger}(\mathbf{r} + \mathbf{R}_j) \Delta V_j(r) \Psi_{\mathbf{k}}^n(\mathbf{r} + \mathbf{R}_j). \quad (3)$$

It describes the scattering of Bloch waves (four component spinors) with spin-mixed character resulting from the relativistic treatment of the ideal and perturbed system at a potential perturbation $\Delta V_j(r)$. Here j runs over all atoms of the impurity cluster. The impurity problem for the potential and the perturbed wave functions $\Psi_{\mathbf{k}}^n(\mathbf{r})$ is solved self-consistently on a real space cluster of 55 atoms via Dyson and Lippman-Schwinger equations starting from the unperturbed ideal crystal with the Bloch states $\Psi_{\mathbf{k}}^n(\mathbf{r})$ [23].

Under the approximation of a weak electric field and the knowledge of a Fermi-Dirac distribution in equilibrium, the linearized Boltzmann equation

$$\Lambda^n(\mathbf{k}) = \tau_{\mathbf{k}}^n \left[\mathbf{v}_{\mathbf{k}}^n + \sum_{\mathbf{k}'} P_{\mathbf{k}'\mathbf{k}}^{n'n} \Lambda^{n'}(\mathbf{k}') \right] \quad (4)$$

is obtained. Here the unknown quantity is the mean free path $\Lambda^n(\mathbf{k})$ determined by the relaxation time

$$(\tau_{\mathbf{k}}^n)^{-1} = \sum_{\mathbf{k}'} P_{\mathbf{k}'\mathbf{k}}^{n'n}, \quad (5)$$

the group velocity

$$\mathbf{v}_{\mathbf{k}}^n = \frac{1}{\hbar} \frac{\partial E_{\mathbf{k}}^n}{\partial \mathbf{k}}, \quad (6)$$

and the scattering-in term $\sum_{\mathbf{k}'} P_{\mathbf{k}'\mathbf{k}}^{n'n} \Lambda^{n'}(\mathbf{k}')$ [24,25]. The linearized Boltzmann equation is an integral equation and can be solved iteratively [23,25,26]. In the low temperature limit the conductivity tensor is given by a Fermi surface integral [23]

$$\underline{\sigma} = \frac{e^2}{\hbar} \sum_n \frac{1}{(2\pi)^3} \iint_{E_{\mathbf{k}}=E_F} \frac{dS_n}{|\mathbf{v}_{\mathbf{k}}^n|} \mathbf{v}_{\mathbf{k}}^n \circ \Lambda^n(\mathbf{k}). \quad (7)$$

For the spin conductivity $\underline{\sigma}^s$, the spin polarization, defined as the expectation value of the spin operator for the states $\Psi_{n\mathbf{k}}$ on the Fermi surface

$$s_z^n(\mathbf{k}) = \langle \Psi_{n\mathbf{k}} | \hat{\beta} \sigma_z | \Psi_{n\mathbf{k}} \rangle, \quad (8)$$

has to be included

$$\underline{\sigma}^s = \frac{e^2}{\hbar} \sum_n \frac{1}{(2\pi)^3} \iint_{E_{\mathbf{k}}=E_F} \frac{dS_n}{|\mathbf{v}_{\mathbf{k}}^n|} s_z^n(\mathbf{k}) \mathbf{v}_{\mathbf{k}}^n \circ \Lambda^n(\mathbf{k}). \quad (9)$$

The conductivities ($\underline{\sigma}$ and $\underline{\sigma}^s$) include the vertex corrections in the dilute limit [27] due to the scattering-in term in Eq. (4). For degenerate bands in a nonmagnetic system with space-inversion symmetry, the procedure introduced

in Ref. [19] is applied to put the quantization axis along the z direction for each \mathbf{k} point. This is necessary to simulate a tiny external magnetic field or ferromagnetic leads to align the electron spins. Following Ref. [19], we denote the wave functions with a positive spin expectation value as Ψ^+ and with a negative one as Ψ^- states, respectively.

The quantum mechanical properties of the system, i.e., the result of the *ab initio* calculation, enter the conductivity evaluation threefold. First, the topology of the Fermi surface determines the states contributing to the conductivity. Second, their Fermi velocities $\mathbf{v}_{\mathbf{k}}^n$, defined by Eq. (6), are taken into account. Finally, the collision term in the Boltzmann equation is calculated from the unperturbed $\Psi_{\mathbf{k}}^n(\mathbf{r})$ and the perturbed $\Psi_{\mathbf{k}}^n(\mathbf{r})$ wave functions of a system with substitutional impurities.

From Fermi's golden rule [Eq. (2)] it follows immediately that, in the dilute limit, the conductivity scales inversely with the number of impurities $c_0 N$. Consequently the ratio of spin Hall conductivity σ_{yx}^s and charge conductivity σ_{xx} is independent on the impurity concentration c_0 . This ratio

$$\alpha = \frac{\sigma_{yx}^s}{\sigma_{xx}} \quad (10)$$

is called the *Hall angle* [16–18].

All calculations presented below are performed with a \mathbf{k} -point mesh larger than 2000 points on a piece of the Fermi surface which lies in the irreducible part of the Brillouin zone. The angular momentum cutoff of $l_{\max} = 3$ is used. A convergence test for these parameters, as well as for the size of the perturbed cluster (55 atoms), turned out that the relative errors of the Hall angle are smaller than 2%.

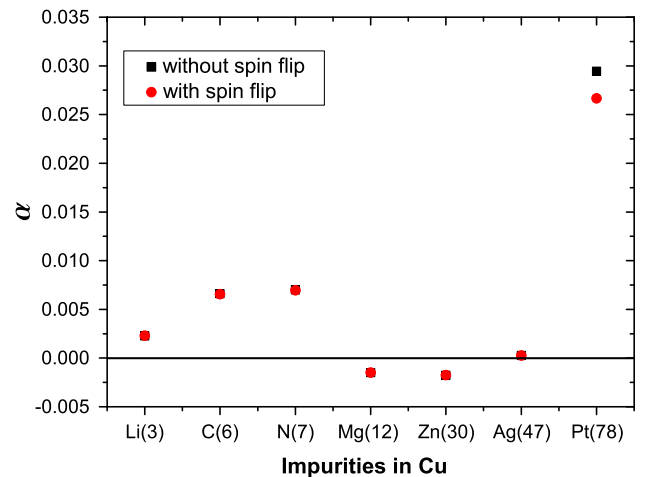


FIG. 1 (color online). The Hall angle α for different substitutional impurities in a Cu host. The number in parentheses gives the core charge connected with the spin-orbit coupling strength at the impurity site.

As the first result, in Fig. 1 the Hall angle α is presented for different substitutional impurities in a Cu host. Without going into details three conclusions can be drawn. First, the very light element Li, which provides nearly no spin-orbit coupling at the impurity site, produces a larger effect than the much heavier element Ag. Second, sign changes of the SHE can occur for some impurities. Finally, the influence of the spin-flip scattering is almost negligible for all impurities.

The presence of a strong extrinsic SHE caused by light impurities is the consequence of the size of the transition matrix elements in Eq. (3). Important for a strong scattering from state \mathbf{k} into \mathbf{k}' is a large potential difference $\Delta V_j(r)$. The spin-orbit coupling is contained in the wave functions already and provided by the host material. Although the spin-orbit interaction caused by Ag is much stronger, the small potential change induced by this isoelectronic element in Cu prevents a sizeable SHE. The mechanism is similar to the effect of the strong spin-flip scattering at light impurities explained in Ref. [20].

The sign change caused by Mg and Zn impurities is more subtle and needs a closer look into the microscopic scattering process included in the Boltzmann equation. As introduced above, the states are separated in Ψ^+ and Ψ^- states by the orientation of their spin polarization along the z axis. The skew scattering process, which is considered here, leads to different scattering amplitudes for these states [6,7,10]. Assuming the incoming state to propagate along the x direction gives an outgoing wave function scattered mainly to the left (+ y) or right ($-y$) depending on the spin state of the wave function. In Fig. 2 the microscopic scattering probabilities for a given state \mathbf{k} are shown as a function of the final states \mathbf{k}' on the Fermi surface of Cu. To visualize the effect of skew scattering, which is usually much weaker than the momentum scattering, the difference ($P_{\mathbf{k}\mathbf{k}'}^{++} - P_{\mathbf{k}\mathbf{k}'}^{--}$) between the probabilities for Ψ^+ and Ψ^- states is shown. The spin-conserving scattering is considered only. The clear asymmetry between the two spin channels is the origin of the spin current and the spatial spin separation, i.e., of the SHE. In addition, the spin separation processes for Zn [Fig. 2(a)] and Li impurities [Fig. 2(b)] are opposite and cause the different sign of the SHE (Fig. 1).

This analysis considers incoming electrons in the x direction only, the spin separation caused by the skew scattering depends strongly on the wave vector \mathbf{k} . For the evaluation of the conductivity tensor, all directions of incoming states have to be considered.

Furthermore, we present the SHE for different impurities in a Au host. The idea is to check if the gigantic SHE of $\alpha \sim 0.1$ measured by Seki *et al.* [17] can be understood in the framework of our approach. As discussed already above, there are several requirements to create a system that exhibits a large SHE. First, a host has to provide significantly spin-mixed Bloch functions. Second, either

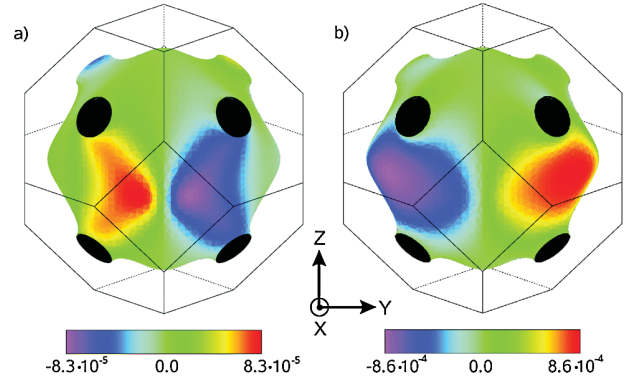


FIG. 2 (color). The skew scattering for (a) Zn and (b) Li impurities in a Cu host. The distribution of ($P_{\mathbf{k}\mathbf{k}'}^{++} - P_{\mathbf{k}\mathbf{k}'}^{--}$) is shown (in arbitrary units) for states \mathbf{k}' at the Fermi level, where the incoming momentum \mathbf{k} points in the [100] direction. The spin polarization for all wave functions is aligned in [001] for Ψ^+ states and in the $[00\bar{1}]$ direction for Ψ^- states, respectively.

the spin-orbit coupling at the impurity site should be strong or the perturbation of the potential has to be large. Consequently, the heavy impurities Ag and Pt are calculated in a Au host. In addition, the light atoms Li, C, and N are considered. The results for α in Au, summarized in Fig. 3, show a very counterintuitive picture. Heavy impurities like Pt and Ag cannot explain the large effect, but typical contaminations in a standard vacuum chamber, like C and N, cause a *gigantic* Hall angle. This result is not in contradiction to the already proposed mechanism originating from a Kondo resonance at Fe impurities, since we are not able to judge which explanation is relevant for the samples investigated in Ref. [17]. Whether the Kondo resonance or the scattering at light impurities causes the *gigantic* spin Hall effect has to be proven experimentally.

In the last part, two important aspects of our calculations are elucidated. Namely, we show how the spin relaxation is included in our calculations. In addition, the importance of the scattering-in term will be discussed. In Cu and Au hosts only two bands are present at the Fermi level with $\Psi_{\mathbf{k}}^+$ and $\Psi_{\mathbf{k}}^-$ degenerate states, according to the spin orientation along the z axis [19]. As a sum over all bands in Eq. (4), we obtain the following expression

$$\Lambda^+(\mathbf{k}) = \tau_{\mathbf{k}}^+ \left[\mathbf{v}_{\mathbf{k}}^+ + \sum_{\mathbf{k}'} \{ P_{\mathbf{k}'\mathbf{k}}^{++} \Lambda^+(\mathbf{k}') + P_{\mathbf{k}'\mathbf{k}}^{--} \Lambda^-(\mathbf{k}') \} \right] \quad (11)$$

with spin-conserving contributions $P_{\mathbf{k}'\mathbf{k}}^{++} \Lambda^+(\mathbf{k}')$ and spin-flip contributions $P_{\mathbf{k}'\mathbf{k}}^{--} \Lambda^-(\mathbf{k}')$. It turns out that the influence of the spin-flip processes is of minor importance and qualitatively similar results are obtained neglecting the spin-flip contribution (see Figs. 1 and 3).

We show the importance of the scattering-in term using $\underline{\sigma}^s$ in the anisotropic relaxation time approximation. This means that the mean free path of Eq. (4) is taken without

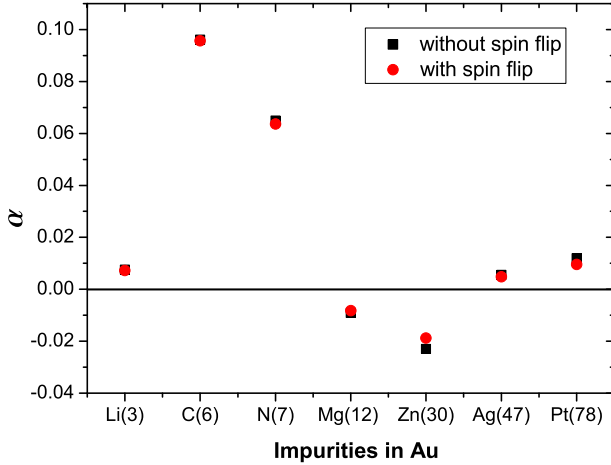


FIG. 3 (color online). The Hall angle α for different substitutional impurities in a Au host.

the scattering-in term: $\Lambda_{(0)}^n(\mathbf{k}) = \tau_{\mathbf{k}}^n \mathbf{v}_{\mathbf{k}}^n$. Inserting this into Eq. (9) and taking into account that the spins point along the z direction with $s_z^+(\mathbf{k}) = -s_z^-(\mathbf{k}) = |s_z(\mathbf{k})|$, the following expression for the spin conductivity is obtained

$$\sigma_{xy}^{s(0)} = \frac{e^2}{\hbar} \frac{1}{(2\pi)^3} \iint \frac{dS}{|v_{\mathbf{k}}|} |s_z(\mathbf{k})| (\tau_{\mathbf{k}}^+ - \tau_{\mathbf{k}}^-) v_{\mathbf{k}}^x v_{\mathbf{k}}^y. \quad (12)$$

From Eq. (12) it is obvious that $\sigma_{xy}^{s(0)} = \sigma_{yx}^{s(0)}$. On the other hand, since the quantization axis is along the z direction and the considered crystals are cubic, C_4 symmetry is present meaning x and y axes are equivalent. So, the symmetry of the system requires an antisymmetric spin conductivity tensor $\sigma_{xy}^{s(0)} = -\sigma_{yx}^{s(0)}$. Thus, both conditions together imply $\sigma_{xy}^{s(0)} = 0$. It shows that the scattering-in term (vertex corrections) is mandatory for the description of the SHE.

In summary, we show that our *ab initio* calculations in combination with the solution of the linearized Boltzmann equation, taking into account the scattering-in term, allow for a description of the skew scattering mechanism in the SHE. The importance of a strong potential perturbation at the impurity site in competition with the strength of the spin-orbit interaction of the substitutional atom is discussed. The sign change of the SHE provided by different impurity atoms in Cu is explained in terms of the microscopic transition probabilities. The extremely large Hall angle induced by C impurities in a Au host is proposed as a possible explanation of the *gigantic* SHE measured in Au. The theoretical results presented here are obtained in the dilute limit of the number of impurities neglecting the intrinsic contribution. For an experimental realization this would mean concentrations of about 1 at. %.

This work was supported by the International Max Planck Research School for Science and Technology and by the Deutsche Forschungsgemeinschaft (SFB 762). We thank Stephan Lowitzer for fruitful discussions.

*martin.gradhand@physik.uni-halle.de

- [1] N.F. Mott and H.S. Massey, *The Theory of Atomic Collisions* (Clarendon Press, Oxford, 1965).
- [2] L.D. Landau and E.M. Lifschitz, *Quantum Mechanics* (Pergamon, New York, 1965).
- [3] M.I. Dyakonov and V.I. Perel, *Phys. Lett. A* **35**, 459 (1971).
- [4] J.E. Hirsch, *Phys. Rev. Lett.* **83**, 1834 (1999).
- [5] R. Karplus and J.M. Luttinger, *Phys. Rev.* **95**, 1154 (1954).
- [6] J. Smit, *Physica* (Amsterdam) **21**, 877 (1955).
- [7] J. Smit, *Physica* (Amsterdam) **24**, 39 (1958).
- [8] L. Berger, *Phys. Rev. B* **2**, 4559 (1970).
- [9] L. Berger, *Phys. Rev. B* **5**, 1862 (1972).
- [10] A. Crépieux and P. Bruno, *Phys. Rev. B* **64**, 014416 (2001).
- [11] J. Sinova, D. Culcer, Q. Niu, N.A. Sinitsyn, T. Jungwirth, and A.H. MacDonald, *Phys. Rev. Lett.* **92**, 126603 (2004).
- [12] N.A. Sinitsyn, *J. Phys. Condens. Matter* **20**, 023201 (2008).
- [13] G.Y. Guo, S. Murakami, T.-W.Chen, and N. Nagaosa, *Phys. Rev. Lett.* **100**, 096401 (2008).
- [14] Y.K. Kato, R.C. Myers, A.C. Gossard, and D.D. Awschalom, *Science* **306**, 1910 (2004).
- [15] S.O. Valenzuela and M. Tinkham, *J. Appl. Phys.* **101**, 09B103 (2007).
- [16] T. Kimura, Y. Otani, T. Sato, S. Takahashi, and S. Maekawa, *Phys. Rev. Lett.* **98**, 156601 (2007).
- [17] T. Seki, Y. Hasegawa, S. Mitani, S. Takahashi, H. Imamura, S. Maekawa, J. Nitta, and K. Takahashi, *Nature Mater.* **7**, 125 (2008).
- [18] G.-Y. Guo, S. Maekawa, and N. Nagaosa, *Phys. Rev. Lett.* **102**, 036401 (2009).
- [19] M. Gradhand, M. Czerner, D.V. Fedorov, P. Zahn, B.Y. Yavorsky, L. Szunyogh, and I. Mertig, *Phys. Rev. B* **80**, 224413 (2009).
- [20] M. Gradhand, D.V. Fedorov, P. Zahn, and I. Mertig, *Phys. Rev. B* **81**, 020403(R) (2010).
- [21] W. Kohn and J.M. Luttinger, *Phys. Rev.* **108**, 590 (1957).
- [22] J.M. Luttinger and W. Kohn, *Phys. Rev.* **109**, 1892 (1958).
- [23] I. Mertig, *Rep. Prog. Phys.* **62**, 237 (1999).
- [24] J.C. Swihart, W.H. Butler, G.M. Stocks, D.M. Nicholson, and R.C. Ward, *Phys. Rev. Lett.* **57**, 1181 (1986).
- [25] P. Zahn, J. Binder, and I. Mertig, *Phys. Rev. B* **68**, 100403 (R) (2003).
- [26] P.T. Coleridge, *J. Phys. F* **2**, 1016 (1972).
- [27] W.H. Butler, *Phys. Rev. B* **31**, 3260 (1985).

3.5 Spin Hall angle versus spin diffusion length: Tailored by impurities

Spin Hall angle versus spin diffusion length: Tailored by impurities

Martin Gradhand,^{1,2,*} Dmitry V. Fedorov,² Peter Zahn,² and Ingrid Mertig^{2,1}

¹Max-Planck-Institut für Mikrostrukturphysik, Weinberg 2, D-06120 Halle, Germany

²Institut für Physik, Martin-Luther-Universität Halle-Wittenberg, D-06099 Halle, Germany

(Received 24 March 2010; revised manuscript received 12 May 2010; published 8 June 2010)

We performed *ab initio* studies to search for materials where a large spin Hall effect caused by skew scattering is accompanied by a long spin diffusion length. Samples with such properties are promising candidates for all-metallic spintronics devices. Here we consider Cu, Au, and Pt hosts which are typical materials used in experiments. In particular, we identified light impurities such as C and N in Au and heavy impurities such as Bi in Cu to meet this criterion. They exhibit a large spin Hall angle ($\alpha > 0.06$) and an appropriate spin diffusion length of about 100 nm. In addition, a pronounced dependence of the spin diffusion length on the scattering properties of the impurity is found for Cu and Au hosts, in contrast to Pt where much smaller variations are obtained.

DOI: [10.1103/PhysRevB.81.245109](https://doi.org/10.1103/PhysRevB.81.245109)

PACS number(s): 75.76.+j, 71.15.Rf, 72.25.Ba, 85.75.-d

I. INTRODUCTION

The spin Hall effect (SHE) is a key issue of spintronics since it allows for the creation of spin currents in nonmagnetic materials avoiding the problem of spin injection from a ferromagnet. Several groups^{1–3} succeeded to measure the effect electronically in metallic devices. Particularly high values for the spin Hall angle α of about 0.1 were obtained for Au wires.³ This angle is defined as the ratio of the spin Hall conductivity σ_{yx}^s to the longitudinal charge conductivity σ_{xx} . Two possible explanations are already proposed for this *gigantic* SHE in Au—a Kondo resonance at Fe impurities⁴ and skew scattering at substitutional C impurities.⁵ Both theoretical studies elucidate only one aspect of the measurement: is it possible to create a large spin current? However, for practical applications of the SHE the spin diffusion length is as well of crucial importance since it limits the size of a spin Hall device.

In this paper, we present a theoretical study of the extrinsic SHE and the spin diffusion length. Considering the influence of substitutional impurities in Cu, Au, and Pt hosts, we identify favorable systems for future spintronics applications.

II. METHOD

The Hall angle is calculated by means of an *ab initio* relativistic Korringa-Kohn-Rostoker method in combination with the solution of a linearized Boltzmann equation.^{5–9} The method is valid in the dilute limit of the impurity concentration c , assuming well separated, noninteracting impurity atoms. In this limit the scattering term, included in the Boltzmann equation,⁵ is proportional to the impurity concentration c . As a consequence, the conductivity tensor $\underline{\sigma}$ is inversely proportional to c ,

$$\underline{\sigma} \sim \frac{1}{c}. \quad (1)$$

Thus, in the dilute limit the Hall angle is evidently independent on the impurity concentration.⁵ If the scattering probabilities are known for a certain dilute alloy, the momentum relaxation τ , as well as, the spin-flip scattering time τ_{sf} can

be derived.⁹ Both scattering times scale inversely proportional to the impurity concentration and their ratio is independent of c . Using both times the spin diffusion length l_{sf} is obtained according to Valet and Fert.¹⁰ In their theory this quantity

$$l_{sf} = \sqrt{\frac{\lambda \lambda_{sf}}{6}} \quad (2)$$

is determined by the (momentum) mean-free path $\lambda = \tau v_F$ and the spin-flip length $\lambda_{sf} = \tau_{sf} v_F$.¹¹ Here v_F is the Fermi velocity. In a free-electron model the expression above is equivalent to^{12,13}

$$l_{sf} = \frac{\pi}{2k_F^2} \sqrt{\frac{3}{2}} \frac{h}{e^2} \sqrt{\frac{\tau_{sf}}{\tau}} \sigma_{xx}, \quad (3)$$

including the Fermi wave vector k_F . Although both formulas are based on a free-electron model they are nevertheless widely used in the literature. The advantage of our approach is that all parameters of Eq. (3) are calculated from first principles taking into account the anisotropy of the Fermi surface and the scattering. In other words, the used k_F , τ_{sf} , and τ are Fermi-surface averages. Moreover, σ_{xx} is obtained by a full solution of the Boltzmann equation including the scattering-in term.⁵

Our main objective is to identify systems of dilute alloys which exhibit a large spin Hall angle in combination with a long spin diffusion length. Such materials are highly desirable for potential applications of the SHE. In the first part of the next section we present results for the spin Hall angle, the longitudinal and the spin Hall conductivity for the considered hosts with different impurities. Then we discuss the spin diffusion length and estimate a reasonable impurity concentration for experimental samples.

III. RESULTS

A. Extrinsic spin Hall effect

In Table I the calculated values of the spin Hall angle are summarized for several dilute alloys. Since the conductivity

TABLE I. The spin Hall angle α as a function of the impurity atom for Cu, Au, and Pt hosts. In addition, the longitudinal charge conductivity σ_{xx} and the transversal spin Hall conductivity σ_{yx}^s are shown at an impurity concentration of 1 at. %.

	Cu			Au			Pt		
	α 10^{-3}	σ_{xx} $(\mu\Omega \text{ cm})^{-1}$	σ_{yx}^s $(10^3 \mu\Omega \text{ cm})^{-1}$	α 10^{-3}	σ_{xx} $(\mu\Omega \text{ cm})^{-1}$	σ_{yx}^s $(10^3 \mu\Omega \text{ cm})^{-1}$	α 10^{-3}	σ_{xx} $(\mu\Omega \text{ cm})^{-1}$	σ_{yx}^s $(10^3 \mu\Omega \text{ cm})^{-1}$
Li	2.3	1.22	2.8	7.2	0.60	4.3	-2.3	0.29	-0.65
C	6.6	0.16	1.0	96.0	0.12	12.0	-2.8	0.26	-0.73
N	7.0	0.11	0.75	64.0	0.08	5.3	11.0	0.19	2.2
Mg	-1.5	1.57	-2.3	-8.2	0.67	-5.5	-3.8	0.29	-1.1
Cu				-0.44	2.96	-1.3	-5.2	0.42	-2.2
Ag	0.26	30.2	7.9	4.8	3.47	17.0	-2.7	0.48	-1.3
Pt	27.0	0.51	13.6	10.0	0.93	9.0			
Au	7.8	2.37	18.5				-1.1	0.83	-0.94
Bi	81.0	0.22	18.1	14.0	0.13	1.9	-1.2	0.25	-0.29

ties (longitudinal and transverse) are inversely proportional to the impurity concentration in the dilute limit, α is independent of the number of impurities. The conductivities are given for a fixed concentration of 1 at. %. As it was discussed already in Ref. 5, C and N impurities in a Au host provide a very high spin Hall angle. The values are comparable to α found experimentally.³ Smaller values obtained by other experimental groups^{14,15} can be explained by the presence of impurities such as Cu and Ag in Au samples. In addition, we find a very large spin Hall angle for Bi impurities in Cu.

The high α values in a Au host with light impurities are a quite counterintuitive result. Nevertheless, it can be explained by means of the scattering phase shifts at the impurity site. Such an approach is justified by the topology of the Fermi surface of Au and Cu,⁸ which allows to use a spherical band approximation. To estimate the strength of the SHE, we can consider the differences of the scattering phase shifts $\delta_j(E_F)$ at the Fermi energy E_F for the total angular momenta $j=l\pm 1/2$ ($l>0$) of an impurity atom and the host atoms. Moreover, for the considered systems it is sufficient to discuss just $l=1$ since scattering of p electrons dominates the effect. Thus, we can restrict our considerations to the p phase shift differences $\Delta\delta_{1/2}(E_F) = \delta_{1/2}^{mp}(E_F) - \delta_{1/2}^{ost}(E_F)$ and $\Delta\delta_{3/2}(E_F) = \delta_{3/2}^{mp}(E_F) - \delta_{3/2}^{ost}(E_F)$. They account for the scattering strength and for the spin-orbit interaction of the impurity, as well as, of the host atom. As it is well known, the splitting of the $p_{1/2}$ and $p_{3/2}$ levels is proportional to the spin-orbit interaction. In the same spirit the difference of $\Delta\delta_{3/2}(E_F)$ and $\Delta\delta_{1/2}(E_F)$ is a measure of the relevant spin-orbit splitting at the impurity site including both the spin-orbit interaction of the host and of the impurity atom. This difference of the p phase shifts is responsible for the left/right asymmetry of scattering for $s=1/2$ and $s=-1/2$ electrons.

Figures 1(a) and 1(b) show $\Delta\delta_{3/2}(E_F)$ and $\Delta\delta_{1/2}(E_F)$ for Cu and Au hosts, respectively. It turns out that the differences of the scattering phase shifts $\Delta\delta_{3/2}(E_F) - \Delta\delta_{1/2}(E_F)$ in Au are particularly large for light impurities. In combination with a strong scattering indicated by large absolute values of $\Delta\delta_{1/2}(E_F)$ and $\Delta\delta_{3/2}(E_F)$, a large spin Hall conductivity is

expected. From this perspective, C and N in Au as well as Bi in Cu are the best candidates for a large extrinsic SHE. They are strong p scatterers with large differences of spin-orbit interaction between host and impurity atoms. The other considered impurities are mainly s or d (for example, Pt) scatterers which leads to small phase shifts in the $l=1$ channel. The picture is confirmed by C and N impurities in Cu. Al-

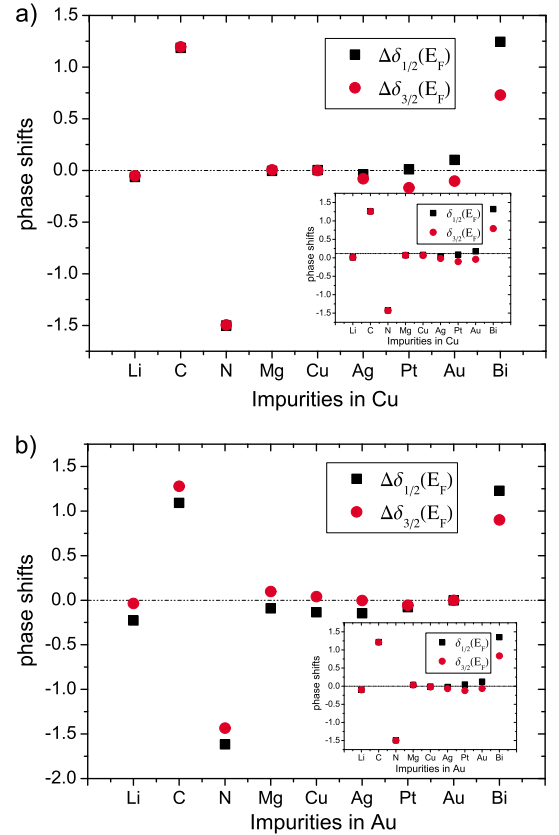


FIG. 1. (Color online) The differences between the scattering phase shifts of an impurity and the host atom for the levels $j=l\pm 1/2$ with $l=1$ (a) Cu host and (b) Au host. As insets the phase shifts of the impurity atoms only are shown.

though they are as well strong p scatterers, the SHE is comparable small since the spin-orbit interaction is negligible for these impurities and for the Cu host. Only heavy p scatterers such as Bi can produce a large α in Cu because of the strong spin-orbit interaction of Bi with respect to Cu. However, the Hall angle for Bi impurities in Au is smaller since the spin-orbit interaction of Bi and Au compensate each other partly. The difference of the phase shifts of Au and Bi atoms, the effective splitting $|\Delta\delta_{3/2}(E_F) - \Delta\delta_{1/2}(E_F)|$ is smaller in Au than in Cu [compare Figs. 1(a) and 1(b)].

To highlight the different nature of the large SHE in Cu with Bi impurities and in Au with C and N impurities, we present as insets of Fig. 1 the phase shifts $\delta_{1/2}^{imp}(E_F)$ and $\delta_{3/2}^{imp}(E_F)$ of the impurity atoms in the considered hosts. Here the phase shift differences between the $p_{1/2}$ and $p_{3/2}$ levels are a measure of the spin-orbit coupling strength of the impurity atoms, only. The light elements, such as C and N, show negligible spin-orbit coupling while for Pt, Au, and Bi the difference between the $p_{1/2}$ and $p_{3/2}$ level is clearly visible. With that knowledge the origin of the large SHE in the Cu(Bi) alloy can clearly be attributed to the spin-orbit coupling induced by Bi impurities. Whereas, for C and N in a Au host, the spin-orbit coupling at the Au atoms is responsible for the large SHE.

The strong variation in α by 2 orders of magnitude as a function of the impurity atom in Cu and Au is attributed to the relatively weak spin-orbit interaction of the hosts. In contrast, the dominant spin-orbit interaction of Pt suppresses the impurity-specific variations. It results in Hall angles which differ by 1 order of magnitude only. In the Pt-based alloys the effect is mainly provided by the host wave functions showing a much stronger spin-mixed character.⁸ The spherical band approximation is not valid for Pt because of its complicated Fermi surface⁸ with mainly d character of the wave functions at the Fermi level. Therefore, such a simple analysis as it was performed above for Au and Cu is impossible for Pt.

To summarize, C and N impurities in Au and Bi impurities in Cu are promising candidates for spintronics applications. However, the preparation of well-defined concentrations of C and N atoms in Au can be rather difficult. In this respect, the dilute Cu(Bi) alloy is preferable since it is known to exist. In addition, a Pt host with N impurities would be as well of interest since we predict a reasonable high spin Hall angle.

An important point to note is that the strength of the SHE in Cu- and Pt-based alloys is of comparable order. Of course, here we neglect the intrinsic SHE which should be much stronger for Pt than for Cu since for Pt several bands cross the Fermi level in contrast to Cu (and Au) with only one band.^{8,16} Nevertheless, our calculated extrinsic spin Hall conductivities are of comparable magnitude to the intrinsic contribution.¹⁶ Therefore, the latter one cannot drastically change α in Pt at low impurity concentrations. Thus, Cu based alloys are equally suited to measure the SHE as Pt based alloys.

B. Spin diffusion length

Now the question arises if it is possible to measure the obtained Hall angles in a real experiment where the system

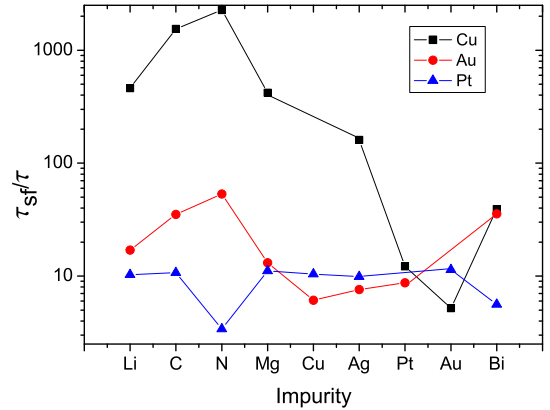


FIG. 2. (Color online) The ratio of the spin-flip scattering time τ_{sf} and the momentum relaxation time τ for different impurity atoms in Cu, Au, and Pt hosts.

size is limited by the spin diffusion length. Equation (3) shows that for a given host material, with a fixed longitudinal conductivity, the ratio of the spin-flip scattering time and the momentum relaxation time determines l_{sf} . Figure 2 summarizes this ratio which is, in the used approximation of dilute alloys, independent on the impurity concentration. For Pt a very weak influence of the impurity character is found. It is different for Cu where the ratio changes over several orders of magnitude. For Au the character of the impurity atom influences the ratio by only 1 order of magnitude. This can be explained by the relatively weak spin mixing of the Au electron states in comparison to the strong mixing induced in Pt.⁸ For a Cu host the spin-orbit coupling is weak and the main contribution arises from the spin-orbit coupling of the impurity atom. In contrast, the spin-orbit interaction in the Pt based alloys is essentially provided by the host.

C. SHE vs spin diffusion length

For the calculation of the spin diffusion length the longitudinal charge conductivity has to be considered as well. However, the conductivity is, in the dilute limit, inversely proportional to the impurity concentration which is not known in experiments. For this purpose the impurity concentration was deduced from experimental data for σ_{xx} published in relation to the SHE and the spin diffusion length.^{14,17,18} We estimated the concentration c_{exp} of a specific impurity by assuming that only one type of impurity atom exists in the sample,

$$c_{exp} = \frac{\sigma_{xx}^{calc}}{\sigma_{xx}^{exp}} c_0. \quad (4)$$

Based on these concentrations, a spin diffusion length $l_{sf}(c_{exp})$ for experimental setups is obtained and summarized in Table II.

For all considered impurities in Pt the value of l_{sf} is nearly the same of about 7 nm, which is in reasonable agreement with experimentally found values in the range of 7–14 nm.^{18,19} For a Au host moderate variations with respect to impurities occur between 42 and 120 nm, which is also in

TABLE II. The spin diffusion length l_{sf} calculated from Eq. (3) with a fixed σ_{xx} for different impurities in Cu, Au, and Pt hosts. The experimental concentration is estimated using Eq. (4). The used experimental values for the conductivity are $\sigma_{xx}(\text{Cu})=0.7$ ($\mu\Omega \text{ cm}$)⁻¹, $\sigma_{xx}(\text{Au})=0.48$ ($\mu\Omega \text{ cm}$)⁻¹, and $\sigma_{xx}(\text{Pt})=0.08$ ($\mu\Omega \text{ cm}$)⁻¹ (Refs. 14, 17, and 18).

	Cu		Au		Pt	
	$l_{sf}(c_{exp})$ (nm)	c_{exp} at. %	$l_{sf}(c_{exp})$ (nm)	c_{exp} at. %	$l_{sf}(c_{exp})$ (nm)	c_{exp} at. %
Li	410	1.7	70	1.3	7.3	3.6
C	750	0.22	100	0.25	7.5	3.3
N	910	0.15	120	0.17	4.2	2.4
Mg	390	2.2	62	1.4	7.6	3.7
Cu			42	6.2	7.4	5.2
Ag	240	43.1	47	7.2	7.2	6.0
Pt	67	0.73	50	1.9		
Au	44	3.4			7.7	10.4
Bi	120	0.32	100	0.28	5.4	3.1

good agreement with experimentally found values of $l_{sf} = 35\text{--}100$ nm.^{3,20–24} The spin diffusion length in Cu varies between 44 nm for Au and 910 nm for N impurities. Experimentally reported values are in the range of 200–1000 nm.^{2,17,21,23–25} Interestingly, the systems with the highest α in Au (C and N impurities) have also the longest l_{sf} which is provided by relatively small longitudinal conductivities. These impurities induce large potential changes which lead to a high resistivity already at low concentrations. The same holds for Bi impurities in Cu and Au lattices. The measured conductivity is reproduced with a small concentration of about 0.3 at. %. At such low concentrations the spin diffusion length is reasonably long ($l_{sf} \approx 100$ nm) for experimental requirements.

Combining the results for the spin Hall conductivity and the estimation of the spin diffusion length, the systems with N and C impurities in Au are good candidates for spintronics applications. In addition, Bi impurities in Cu provide both, a long spin diffusion length and a large spin Hall angle. On the other hand, there is no advantage to use Pt instead of Cu as a host material for spin Hall measurements. The spin diffusion length l_{sf} in Cu is more than one order of magnitude larger than in Pt which implies that Cu should be used instead of Pt.

IV. CONCLUSION

We have investigated the influence of several substitutional defects in Cu, Au, and Pt bulk crystals on the spin Hall angle and the spin diffusion length. It is shown that tailoring these quantities is possible for a light hosts such as Cu. Whereas, the role of impurities is minor for materials with strong intrinsic spin-orbit interaction like Pt. C and N impurities in a Au host and Bi impurities in a Cu host are identified as best candidates for all-metallic spin-current generation. At impurity concentrations feasible in experiment they show a spin Hall angle of 0.096, 0.064, and 0.081 combined with a spin diffusion length of 101 nm, 124 nm, and 120 nm, respectively. In addition, we find that Cu is a more attractive host material in comparison to Pt for the analysis of the skew scattering contribution to the SHE since Cu exhibits an extrinsic SHE comparable to Pt-based alloys and has at the same time a much longer spin diffusion length.

ACKNOWLEDGMENTS

This work was supported by the International Max Planck Research School for Science and Technology of Nanostructures and by the Deutsche Forschungsgemeinschaft (Grant No. SFB 762).

*martin.gradhand@physik.uni-halle.de

¹S. O. Valenzuela and M. Tinkham, *J. Appl. Phys.* **101**, 09B103 (2007).

²T. Kimura, Y. Otani, T. Sato, S. Takahashi, and S. Maekawa, *Phys. Rev. Lett.* **98**, 156601 (2007).

³T. Seki, Y. Hasegawa, S. Mitani, S. Takahashi, H. Imamura, S. Maekawa, J. Nitta, and K. Takahashi, *Nature Mater.* **7**, 125 (2008).

⁴G.-Y. Guo, S. Maekawa, and N. Nagaosa, *Phys. Rev. Lett.* **102**,

036401 (2009).

⁵M. Gradhand, D. V. Fedorov, P. Zahn, and I. Mertig, *Phys. Rev. Lett.* **104**, 186403 (2010).

⁶I. Mertig, *Rep. Prog. Phys.* **62**, 237 (1999).

⁷P. Zahn, J. Binder, and I. Mertig, *Phys. Rev. B* **68**, 100403(R) (2003).

⁸M. Gradhand, M. Czerner, D. V. Fedorov, P. Zahn, B. Y. Yavorsky, L. Szunyogh, and I. Mertig, *Phys. Rev. B* **80**, 224413 (2009).

- ⁹M. Gradhand, D. V. Fedorov, P. Zahn, and I. Mertig, *Phys. Rev. B* **81**, 020403(R) (2010).
- ¹⁰T. Valet and A. Fert, *Phys. Rev. B* **48**, 7099 (1993).
- ¹¹J. Bass and W. P. Pratt, Jr., *J. Phys.: Condens. Matter* **19**, 183201 (2007).
- ¹²S. Takahashi and S. Maekawa, *Physica C* **437-438**, 309 (2006).
- ¹³We want to mention that, according to Eq. (11) of Ref. 12, the spin-flip scattering time used by Takahashi and Maekawa is actually half of our $\tau_{sf}=2T_1$ (Ref. 26) [where T_1 is the spin-relaxation time (Ref. 27)].
- ¹⁴G. Mihajlović, J. E. Pearson, M. A. Garcia, S. D. Bader, and A. Hoffmann, *Phys. Rev. Lett.* **103**, 166601 (2009).
- ¹⁵O. Mosendz, J. E. Pearson, F. Y. Fradin, G. E. W. Bauer, S. D. Bader, and A. Hoffmann, *Phys. Rev. Lett.* **104**, 046601 (2010).
- ¹⁶G. Y. Guo, S. Murakami, T. W. Chen, and N. Nagaosa, *Phys. Rev. Lett.* **100**, 096401 (2008).
- ¹⁷F. J. Jedema, A. T. Filip, and B. J. van Wees, *Nature (London)* **410**, 345 (2001).
- ¹⁸L. Vila, T. Kimura, and Y. C. Otani, *Phys. Rev. Lett.* **99**, 226604 (2007).
- ¹⁹H. Kurt, R. Loloee, K. Eid, W. P. Pratt, and J. Bass, *Appl. Phys. Lett.* **81**, 4787 (2002).
- ²⁰H. Kurt, W. Chiang, C. Ritz, K. Eid, W. Pratt, and J. Bass, *J. Appl. Phys.* **93**, 7918 (2003).
- ²¹Wen-C. Chiang, C. Ritz, K. Eid, R. Loloee, W. P. Pratt, and J. Bass, *Phys. Rev. B* **69**, 184405 (2004).
- ²²Y. Ji, A. Hoffmann, J. S. Jiang, and S. D. Bader, *Appl. Phys. Lett.* **85**, 6218 (2004).
- ²³T. Kimura, J. Hamrle, and Y. Otani, *Phys. Rev. B* **72**, 014461 (2005).
- ²⁴Y. Ji, A. Hoffmann, J. S. Jiang, J. E. Pearson, and S. D. Bader, *J. Phys. D* **40**, 1280 (2007).
- ²⁵Q. Yang, P. Holody, S.-F. Lee, L. L. Henry, R. Loloee, P. A. Schroeder, W. P. Pratt, and J. Bass, *Phys. Rev. Lett.* **72**, 3274 (1994).
- ²⁶D. V. Fedorov, P. Zahn, M. Gradhand, and I. Mertig, *Phys. Rev. B* **77**, 092406 (2008).
- ²⁷A. Fert and S. F. Lee, *Phys. Rev. B* **53**, 6554 (1996).

Chapter 4

Summary

With this work I presented an *ab initio* description of two effects driven by the spin-orbit coupling. The first one is the Elliott-Yafet spin relaxation mechanism and the second one is the extrinsic spin Hall effect. Both of them are induced by spin-orbit scattering of conduction electrons at impurities. Using a relativistic Korringa-Kohn-Rostoker method it is possible to treat the host as well as the impurity atoms taking into account spin-orbit interaction by means of a solution of the Dirac equation, which is essential to describe the effects properly. For the relaxation mechanism I calculated the microscopic transition probabilities which are the origin of the spin relaxation and the spin Hall effect. For the electronic and the spin transport I solved the linearized Boltzmann equation including the scattering-in term (vertex correction), which turns out to be mandatory for a description of the skew scattering mechanism.

I showed, that taking the spin-orbit coupling of the host into account allows for a proper description of conduction electron spin resonance experiments even for light impurities with vanishing spin-orbit interaction. The agreement between the calculated and measured spin relaxation times is convincing.

Concerning the spin Hall effect, I identified two possibilities to create a large spin Hall angle. Since the difference of the spin-orbit coupling between host and impurity atom is shown to be the most important quantity, systems consisting of a heavy host with light impurities or vice versa are of interest. With light elements such, as C or N, I gave an alternative explanation for the gigantic spin Hall effect measured in Au. However, a Cu host with Bi impurities yields a comparable large Hall angle. Small Hall angles can be obtained for many other impurity atoms, which explains the wide range of measured Hall angles in Au.

Having access to the spin state and the total angular momentum decomposition of the wavefunctions on the Fermi surface allows for a clear understanding of the microscopic origin of the Elliott-Yafet mechanism as well as the spin Hall effect. The scattering probabilities give a clear picture of the skew scattering mechanism responsible for the extrinsic spin Hall effect.

From the spin relaxation time it is possible to calculate the spin diffusion length which is in good agreement to the measured ones. Whereas for Cu and Au hosts the spin diffusion length strongly depends on the impurity atom, this is not the case for Pt.

Combining the spin relaxation and the conductivity calculations makes it possible to identify three attractive systems for possible future spintronics applications. They are Au(N), Au(C), and Cu(Bi) dilute alloys which show a large spin Hall angle with a reasonably long spin diffusion length of the order of 100 nm.

Appendix A

Dependence of ρ_{yx} on ρ_{xx} in the dilute limit

To find an expression for the Hall resistivity in terms of the longitudinal conductivity we need the connection between the resistivity and the conductivity tensor for a crystal with cubic symmetry

$$\underline{\rho} = \underline{\sigma}^{-1} = \begin{pmatrix} \sigma_{xx} & \sigma_H & 0 \\ -\sigma_H & \sigma_{yy} & 0 \\ 0 & 0 & \sigma_{zz} \end{pmatrix}^{-1}. \quad (\text{A.1})$$

Inverting the conductivity yields

$$\underline{\rho} = \begin{pmatrix} \frac{\sigma_{xx}}{\sigma_{xx}^2 + \sigma_H^2} & -\frac{\sigma_H}{\sigma_{xx}^2 + \sigma_H^2} & 0 \\ \frac{\sigma_H}{\sigma_{xx}^2 + \sigma_H^2} & \frac{\sigma_{xx}}{\sigma_{xx}^2 + \sigma_H^2} & 0 \\ 0 & 0 & \frac{1}{\sigma_{zz}} \end{pmatrix}. \quad (\text{A.2})$$

In chapters 1.3 and 2.4 it was discussed that the longitudinal conductivity is inversely proportional to the impurity concentration

$$\sigma_{xx} \propto c^{-1} \quad (\text{A.3})$$

whereas, the Hall conductivity

$$\sigma_H = \sigma_H^{intr} + \sigma_H^{ss} + \sigma_H^{sj} \quad (\text{A.4})$$

shows different dependencies on the impurity concentration in the dilute limit for the three distinct mechanisms

$$\sigma_H^{intr} \propto c^0, \sigma_H^{ss} \propto c^{-1}, \text{ and } \sigma_H^{sj} \propto c^0. \quad (\text{A.5})$$

Inserting this into Eq. (A.2) for the different mechanisms separately gives

$$\underline{\rho}^{ss} \propto \begin{pmatrix} c & -c & 0 \\ c & c & 0 \\ 0 & 0 & c \end{pmatrix} \quad (\text{A.6})$$

for the skew scattering contribution, and

$$\underline{\rho}^{intr/sj} \propto \begin{pmatrix} c/2 & -\frac{c^2}{1+c^2} & 0 \\ \frac{c^2}{1+c^2} & c/2 & 0 \\ 0 & 0 & c \end{pmatrix} \approx \begin{pmatrix} c/2 & -c^2 & 0 \\ c^2 & c/2 & 0 \\ 0 & 0 & c \end{pmatrix} \quad (\text{A.7})$$

for the intrinsic and the side-jump mechanism. Consequently, the dependence of the Hall resistivity on the longitudinal conductivity is linear for the skew scattering mechanism

$$\rho_H^{ss} \propto \rho_{xx} \tag{A.8}$$

and quadratic for the other two contributions

$$\rho_H^{intr} \propto \rho_{xx}^2 \tag{A.9}$$

and

$$\rho_H^{sj} \propto \rho_{xx}^2 . \tag{A.10}$$

The additional quadratic term for the skew scattering mechanism found by Crepieux and Bruno [41] is caused by higher orders in the concentration dependence of the longitudinal conductivity σ_{xx} which is already beyond the dilute limit regime.

Appendix B

Numerical parameters within the KKR method

The presented results were checked for convergence with respect to several numerical parameters within the used KKR method. Those are for example the:

- k mesh for the Green function of the periodic system
- k mesh for the Fermi surface integration
- cluster size of the perturbed cluster
- cluster size of the screening cluster
- imaginary part of the energy for the evaluation of the perturbed Green function at the Fermi level

I present here some of the convergence tests and list the typically used parameters for the discussed results. For all test calculations presented in the this chapter Ga impurities in a Cu host were used.

B.1 Periodic host system

Self-consistent calculation

Since the self-consistent bulk calculations are well established for many years, I skip any convergence tests for this part. Only the most prominent parameters are collected in Table B.1.

Table B.1: A collection of the numerical parameters typically used for the self-consistent calculation of the periodic host system

k-mesh	screening cluster	imaginary part of the energy
64x64x64	141 sites (eight nearest neighbor shells)	108 meV

Determination of the Fermi surface, the wavefunctions, and the Fermi velocity of the periodic host system

Table B.2: A collection of the numerical parameters typically used for the evaluation of the Fermi surface properties in the irreducible part of the Brillouin zone

screening cluster	imaginary part of the energy	ΔE for the numerical energy derivative	k-points
249 sites (twelve nearest neighbor shells)	0.0 eV	13.6 μeV	≈ 40000

B.2 Self-consistent impurity problem

For the impurity problem the Green function of the host system is needed (see Sec. 2.1.5). The numerical parameters are equivalent to the self-consistent host calculation in Sec. B.1. The only further parameter is the size of the perturbed cluster with 55 atoms. I checked the convergence of the spin Hall angle α and the ratio of the spin-flip scattering τ_{sf} and momentum relaxation times τ with respect to the size of the perturbed cluster (Fig. B.1). It is obvious that 55 atoms is large enough.

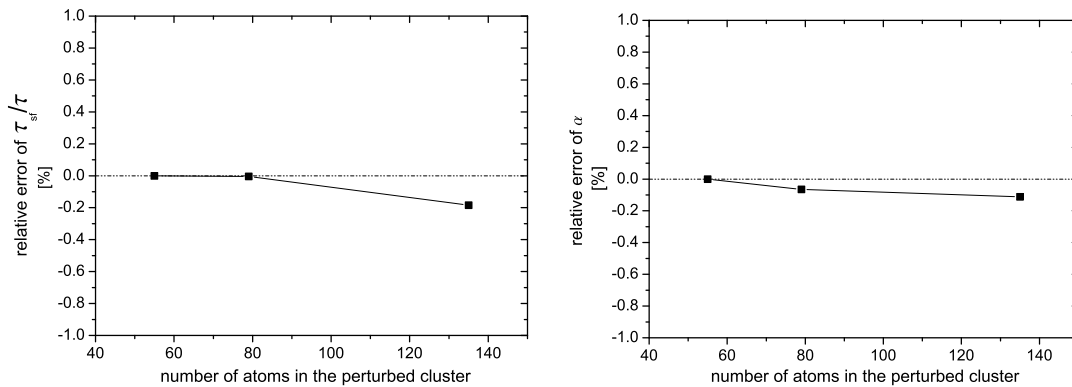


Figure B.1: The convergence test for τ_{sf}/τ and α with respect to the perturbed cluster in the impurity calculation.

B.3 Transport calculation

The implementation to calculate the scattering term using the relativistic band structure and wavefunctions of the system was a main part of the thesis. Here, I present convergence tests for the spin Hall angle and the ratio of the spin-flip scattering and momentum relaxation times with respect to several numerical parameters. It is separated in two parts. The first one contains parameters for the calculation of the impurity Green function and the second part the numerics for the Fermi surface averages.

Calculation of the Green function of the impurity system

Table B.3: A collection of the numerical parameters typically used for the calculation of the Green function of the host system for the transport calculation

screening cluster	imaginary part of the energy	k-points
249 sites (twelve nearest neighbor shells)	5.4 meV	400x400x400

For a calculation of the Green function of the impurity system the Green function of the host system has to be known. The two important numerical parameters are the imaginary part of the energy and the number of k points. In principle, the Green function with vanishing imaginary part of the energy is needed. However, in this case a numerical integration is impossible due to the poles caused by the states of the host system. The number of k points would be infinitely large. In reality a compromise between the number of k points and the imaginary part of the energy must be found. The typically used parameters are summarized in Tab. B.3. It turned out that the actual calculated numbers are quite robust against the parameters. Especially an increase of the size of the screening cluster has nearly no influence. The number of k points is already more crucial for small imaginary parts of the energy. Using 5.4 meV as imaginary part, the influence of the number of k points on the calculated values is

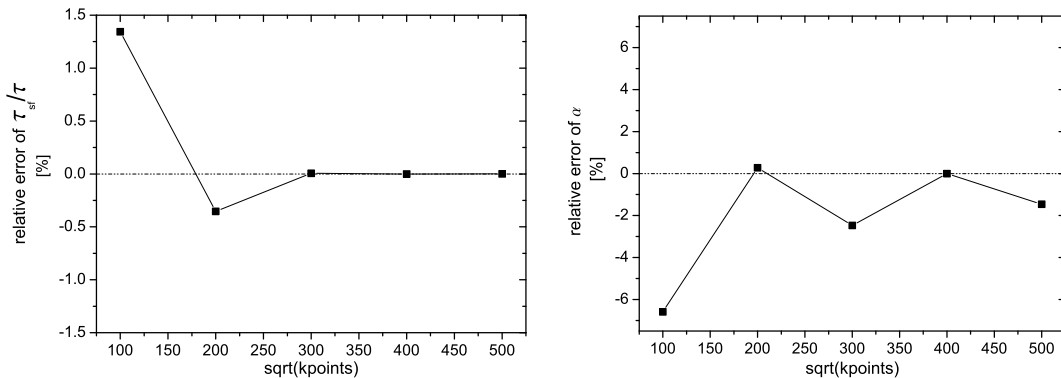


Figure B.2: The convergence test for τ_{sf}/τ and α with respect to the k mesh used in the evaluation of the host Green function for the transport calculation.

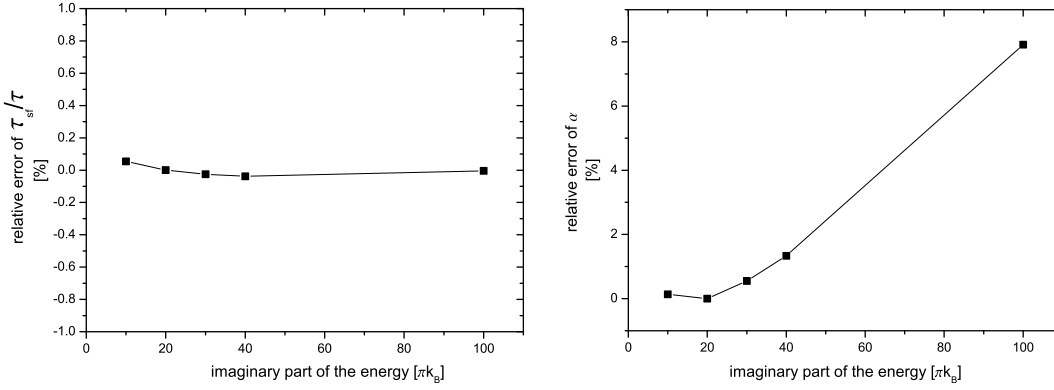


Figure B.3: The convergence test for τ_{sf}/τ and α with respect to the imaginary part of the energy used in the evaluation of the host Green function for the transport calculation

shown in Fig. B.2. The ratio of the relaxation times is perfectly well converged whereas for the error of the Hall angle small oscillations of about 2 % are visible. However, this accuracy is good enough for all discussion of the Hall angles.

A similar result I obtain changing the imaginary part of the energy (see Fig. B.3). The ratio of the relaxation times is nearly independent of the imaginary part of the energy and the error is smaller than 0.1 %. For the Hall angle α the influence is more pronounced. With the exception of the largest imaginary part all deviations are smaller than 2 % which is good enough for all discussions.

K-mesh for the Fermi surface integration

Here an important quantity, the number of k points used in the Fermi surface integration, is discussed. For all calculations I used at least 2000 k points in the irreducible part of the Fermi surface. Figure B.4 turns out that increasing the k points would change the results only within 1 %.

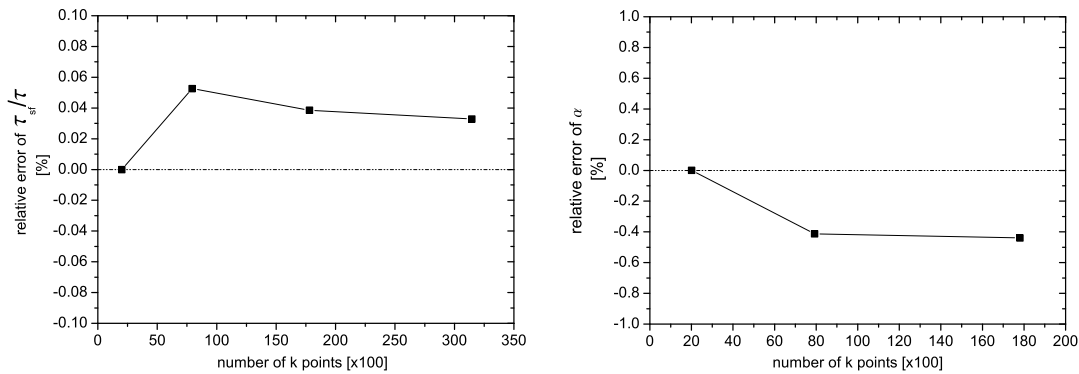


Figure B.4: The convergence test for τ_{sf}/τ and α with respect to the number of k points used in the Fermi surface integration. The actual number of k points on the full Fermi surface is larger by the factor of 8 due to the used symmetry operations.

Appendix C

Fermi velocity for different metals

Here, I will compare the results of the two methods presented in section 2.2.3 for the calculation of the Fermi velocity. In Fig. C.1 the x component of the Fermi velocity for three non-magnetic materials is shown. First of all it is obvious that for the here considered simple Fermi surfaces both methods show a reasonable agreement. That is the reason why for all calculations presented in this thesis the already implemented numerical method was used to calculate the Fermi velocity. However comparing both methods in more detail turns out that for the numerical derivative (Fig. C.1 left column) the Fermi velocity depends on the orientation of the tetrahedron. This leads to small jumps going from one tetrahedron to the other. This is especially pronounced in regions of a strongly bent Fermi surface. For the analytical \mathbf{k} derivative (Fig. C.1 right column) this feature vanishes due to the direct evaluation of the Fermi velocity for a certain \mathbf{k} state. The advantage of the analytical \mathbf{k} derivative is evident. Whereas for the numerical method the \mathbf{k} mesh must be increased for a strongly bent Fermi surface to compute the Fermi velocity correctly the new method is much more stable and can be evaluated on a smaller mesh which saves computing time.

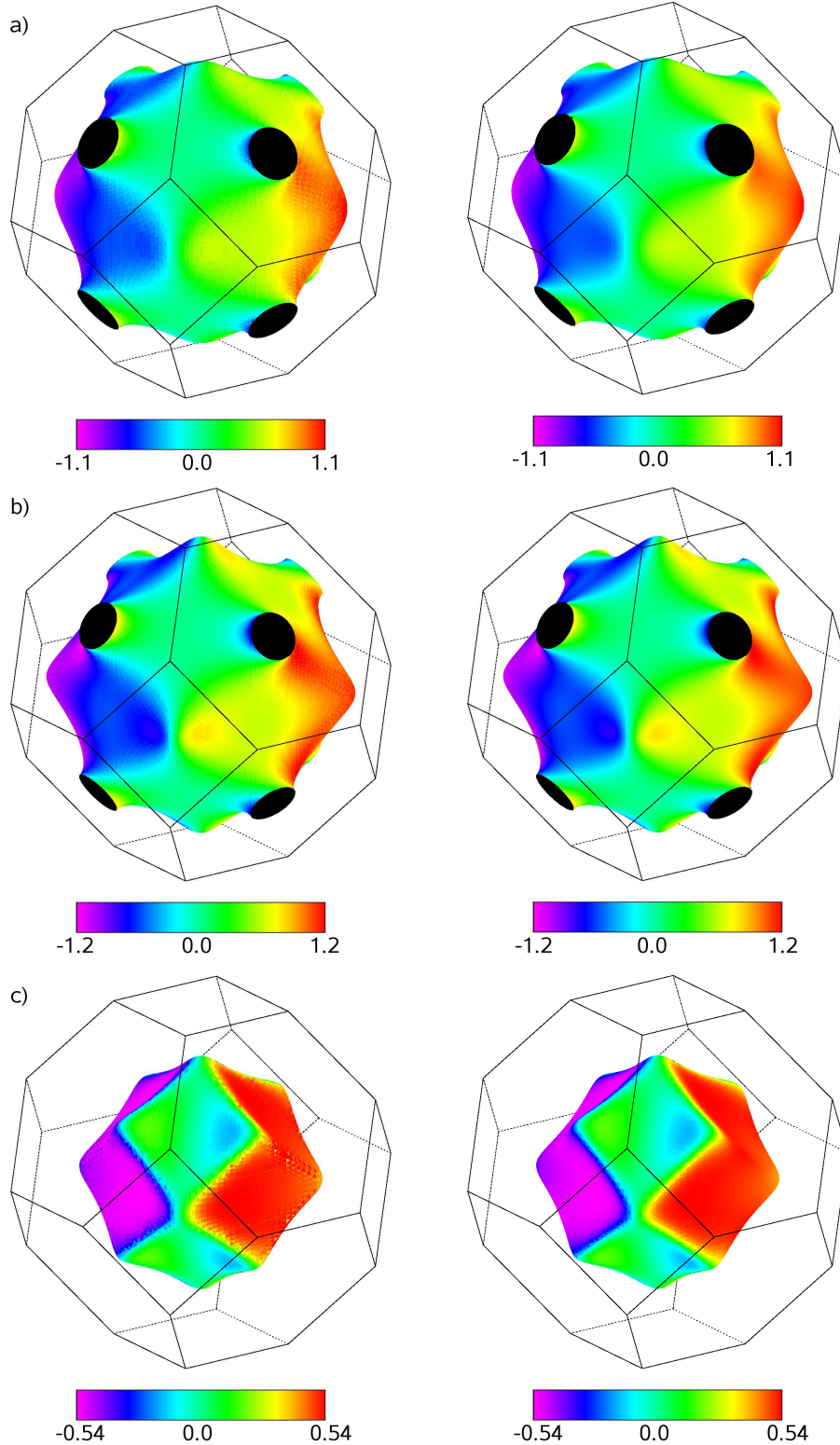


Figure C.1: Comparison of the velocity calculations with the two method introduced in section 2.2.3 (left column: numerical \mathbf{k} derivative, right column: the analytic \mathbf{k} derivative). Shown is the x component of the Fermi velocity \mathbf{v} (arbitrary units) for the non-magnetic materials a) Cu, b) Au and c) Pt (the 11th band). For the numerical \mathbf{k} derivative an influence of the orientation of the tetrahedron can be see, especially for Pt, whereas for the analytical \mathbf{k} derivative the orientation of the tetrahedron has no influence.

Appendix D

Influence of vertex corrections (scattering-in term) on the spin Hall effect

The importance of the scattering-in term for the description of the SHE was discussed in Sec. 3.4 [E7], but should be highlighted ones more. The scattering-in term in the Boltzmann equation is given by $\sum_{\mathbf{k}'\nu'} P_{\mathbf{k}\mathbf{k}'}^{\nu'\nu} \Lambda^{\nu'}(\mathbf{k}')$ and is needed if one goes beyond the anisotropic relaxation time approximation. Butler [87] showed that this term is equivalent to the vertex corrections of the Kubo formula in the dilute limit of the impurity concentration. The interesting point is that the skew scattering part of the spin Hall effect is purely encoded by the scattering-in term. It follows from the absence of the spin Hall effect in the anisotropic relaxation time approximation. This fact was confirmed by our calculations, but one can understand it in a more general way. The spin Hall conductivity σ^s is given in the anisotropic relaxation time approximation by [E7]

$$\sigma_{xy}^s = \frac{e^2}{\hbar} \frac{1}{(2\pi)^3} \iint \frac{dS}{|v_{\mathbf{k}}|} |s_z(\mathbf{k})| (\tau_{\mathbf{k}}^+ - \tau_{\mathbf{k}}^-) v_{\mathbf{k}}^x v_{\mathbf{k}}^y. \quad (\text{D.1})$$

It follows obviously that $\sigma_{xy}^s = \sigma_{yx}^s$. On the other hand, the reduced symmetry of the relativistic description requires, due to the presence of C_4 symmetry operations, an antisymmetric conductivity tensor with $\sigma_{xy}^s = -\sigma_{yx}^s$. Both conditions imply that the Hall conductivity is zero in the anisotropic relaxation time approximation. Neglecting the scattering-in term leads to a zero spin Hall current. It is clear that taking it into account is mandatory for the description of the spin Hall effect. I remind the reader of the fact that the scattering-in term is equivalent to the vertex corrections of the Kubo formalism in the dilute limit of the impurity concentration [87]. Therefore, the vertex corrections are crucial to describe the skew scattering within the Kubo formalism.

Recently, the group of H. Ebert has solved the Kubo-Streda equation [88] for several random alloys including the vertex corrections for the antisymmetric part of the conductivity tensor. A comparison of their [89] and my data showed the importance of the vertex corrections in the dilute limit and identified different extrinsic and intrinsic contributions to the SHE. It turned out that the linearized Boltzmann equation is valid up to 10 at. % of the impurity concentration. The agreement for the calculated skew scattering contribution is very good between the two methods (see Fig. D.1).

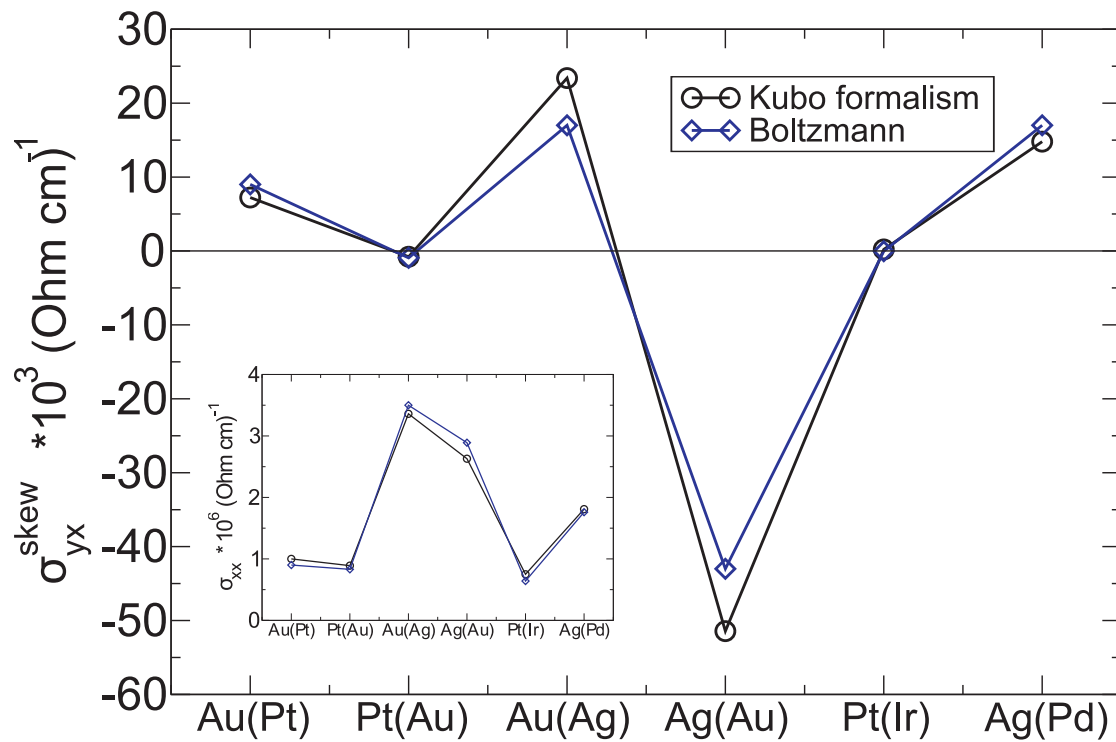


Figure D.1: The spin Hall conductivity caused by the skew scattering contribution for different dilute alloys (1 at. %). The considered contribution in the Kubo formalism is extracted using a linear fit for the dependence of σ_{yx}^s on σ_{xx} in the dilute limit [89]. The inset shows a comparison of the longitudinal charge conductivity σ_{xx} for the same alloys.

Appendix E

Spin diffusion length in a free-electron like model

Here, I want to show the equivalence of the two formulas for the spin diffusion length l_{sf} , Eqs. (2.100) and (2.101) introduced in section 2.3, in a free electron like model. Let us start with the expression (2.101)

$$l_{sf} = \frac{\pi}{2k_F^2} \sqrt{\frac{3}{2}} \frac{\hbar}{e^2} \sqrt{\frac{\tau_{sf}}{\tau}} \sigma_{xx} , \quad (\text{E.1})$$

where the spin diffusion length is expressed by the relaxation times τ and τ_{sf} and the longitudinal conductivity σ_{xx} . The task is to find the conductivity for the free electron like model. In the relaxation time approximation with one band at the Fermi level

$$\sigma_{xx} = 2 \frac{e^2}{\hbar} \frac{\tau}{(2\pi)^3} \iint_{E_{\mathbf{k}}=E_F} \frac{dS}{|\mathbf{v}_{\mathbf{k}}|} (v_{\mathbf{k},x})^2 , \quad (\text{E.2})$$

where the velocity, assuming a free electron dispersion, is given by

$$v_{\mathbf{k},x} = \frac{1}{\hbar} \frac{\partial E_{\mathbf{k}}}{\partial k_x} = \frac{\hbar k_x}{m} . \quad (\text{E.3})$$

The Fermi surface integral for a spherical band (free electrons) simplifies to

$$\sigma_{xx} = \frac{e^2}{m} \frac{\tau}{(2\pi)^3} \frac{2}{3} \iint_{E_{\mathbf{k}}=E_F} \frac{d^2k}{k} k^2 \quad (\text{E.4})$$

with $k = |\mathbf{k}|$. The actual integral is

$$\iint_{E_{\mathbf{k}}=E_F} \frac{d^2k}{k} k^2 = 4\pi k_F^3 , \quad (\text{E.5})$$

which results in a longitudinal conductivity

$$\sigma_{xx} = \frac{e^2}{m} \frac{\tau}{2\pi^2} \frac{2}{3} k_F^3 . \quad (\text{E.6})$$

Inserting this result into Eq. (E.1) yields

$$l_{sf} = \frac{k_F \hbar}{m} \sqrt{\frac{\tau_{sf} \tau}{6}} = \sqrt{\frac{\tau_{sf} \tau}{6}} v_F \quad (\text{E.7})$$

which is equivalent to Eq. (2.100) using the definitions $\lambda = v_F \tau$ and $\lambda_{sf} = v_F \tau_{sf}$.

Appendix F

Relativistic symmetry of a cubic lattice

Throughout all calculations presented in this work the symmetry of the system was used to reduce the computational effort. This is just one of the reasons why the symmetry of a cubic lattice in the presence of spin-orbit coupling is outlined shortly. In addition, the symmetry gives a nice argument why the SHE vanishes in absence of spin-orbit coupling.

The systems under consideration (Cu, Au, and Pt) have the fcc cubic lattice with 48 symmetry operations. Including spin-orbit interaction in the Hamiltonian reduces the symmetry of the system since the Hamiltonian does not commute with all 48 symmetry operations anymore. If the quantization axis is chosen to be along z , only a symmetry operation \hat{A} which fulfill the condition

$$\begin{pmatrix} 0 \\ 0 \\ z' \end{pmatrix} = \frac{1}{\det|\hat{A}|} \hat{A} \begin{pmatrix} 0 \\ 0 \\ z \end{pmatrix} = \begin{pmatrix} 0 \\ 0 \\ z \end{pmatrix} \quad (\text{F.1})$$

is still allowed in the relativistic case. As a consequence only the rotation of 90° , 180° , and 270° around the z axis in combination with the inversion are proper symmetry operations. That reduces the number to 8 symmetry operations. That implies that the irreducible part is $1/8$ of the whole Brillouin zone. This is used for the self-consistent calculation of the host crystal as well as for the evaluation of the cluster Green function and the Fermi surface integrals. The reduced symmetry is nicely visualized comparing the \mathbf{k} -dependent momentum relaxation and spin-flip scattering times in the perturbative approach (see Sec. 3.1 [E4]).

The argument that with full non-relativistic symmetry the SHE would vanish is quite simple and follows from the presence of the additional mirror planes along xz and yz . With all 48 symmetry operations it follows that the conductivity tensor for each spin channel σ_s has to be diagonal. This leads to a zero spin Hall current.

Bibliography

- [1] **N. F. Mott, H. S. W. Massey.** *The theory of atomic collisions.* Clarendon Press, Oxford (1965).
- [2] **L. D. Landau, E. M. Lifshitz.** *Quantum Mechanics.* Pergamon (1965).
- [3] **M. I. Dyakonov, V. I. Perel.** *Current-induced spin orientation of electrons in semiconductors.* Phys. Lett. A **35**, 459 (1971).
- [4] **J. E. Hirsch.** *Spin Hall Effect.* Phys. Rev. Lett. **83**, 1834 (1999).
- [5] **Y. K. Kato, R. C. Myers, A. C. Gossard, D. D. Awschalom.** *Observation of the Spin Hall Effect in Semiconductors.* Science **306**, 1910 (2004).
- [6] **Y. Yao, Z. Fang.** *Sign Changes of Intrinsic Spin Hall Effect in Semiconductors and Simple Metals: First-Principles Calculations.* Phys. Rev. Lett. **95**, 156601 (2005).
- [7] **E. Saitoh, M. Ueda, H. Miyajima.** *Conversion of spin current into charge current at room temperature: Inverse spin-Hall effect.* Applied Physics Letters **88**, 182509 (2006).
- [8] **S. O. Valenzuela, M. Tinkham.** *Electrical detection of spin currents: The spin-current induced Hall effect.* J. Appl. Phys. **101**, 09B103 (2007).
- [9] **T. Kimura, Y. Otani, T. Sato, S. Takahashi, S. Maekawa.** *Room-Temperature Reversible Spin Hall Effect.* Phys. Rev. Lett. **98**, 156601 (2007).
- [10] **K. Ando, S. Takahashi, K. Harii, K. Sasage, J. Ieda, S. Maekawa, E. Saitoh.** *Electric Manipulation of Spin Relaxation Using the Spin Hall Effect.* Phys. Rev. Lett. **101**, 036601 (2008).
- [11] **T. Seki, Y. Hasegawa, S. Mitani, S. Takahashi, H. Imamura, S. Maekawa, J. Nitta, K. Takanashi.** *Giant spin Hall effect in perpendicularly spin-polarized FePt/Au devices.* Nature Materials **7**, 125 (2008).
- [12] **G. Y. Guo, S. Murakami, T. W. Chen, N. Nagaosa.** *Intrinsic Spin Hall Effect in Platinum: First-Principles Calculations.* Phys. Rev. Lett. **100**, 096401 (2008).
- [13] **G.-Y. Guo, S. Maekawa, N. Nagaosa.** *Enhanced Spin Hall Effect by Resonant Skew Scattering in the Orbital-Dependent Kondo Effect.* Phys. Rev. Lett. **102**, 036401 (2009).

-
- [14] **S. A. Wolf, D. D. Awschalom, R. A. Buhrman, J. M. Daughton, S. von Molnár, M. L. Roukes, A. Y. Chtchelkanova, D. M. Treger.** *Spintronics: A Spin-Based Electronics Vision for the Future.* Science **294**, 1488 (2001).
- [15] **E. I. Rashba.** *Spintronics: Sources and Challenge. Personal Perspective.* J. Supercond. Incomp. Novel Magn. **15**, 1317 (2002).
- [16] **I. Zutic, J. Fabian, S. Das Sarma.** *Spintronics: Fundamentals and applications.* Rev. Mod. Phys. **76**, 323 (2004).
- [17] **G. Schmidt, D. Ferrand, L. W. Molenkamp, A. T. Filip, B. J. van Wees.** *Fundamental obstacle for electrical spin injection from a ferromagnetic metal into a diffusive semiconductor.* Phys. Rev. B **62**, R4790 (2000).
- [18] **A. Fert, H. Jaffrès.** *Conditions for efficient spin injection from a ferromagnetic metal into a semiconductor.* Phys. Rev. B **64**, 184420 (2001).
- [19] **T. Yang, T. Kimura, Y. Otani.** *Giant spin-accumulation signal and pure spin-current-induced reversible magnetization switching.* Nature Physics **4**, 851 (2008).
- [20] **V. Sih, R. C. Myers, Y. K. Kato, W. H. Lau, A. C. Gossard, D. D. Awschalom.** *Spatial imaging of the spin Hall effect and current-induced polarization in two-dimensional electron gases.* Nature Letters **1**, 31 (2005).
- [21] **L. Vila, T. Kimura, Y. Otani.** *Evolution of the Spin Hall Effect in Pt Nanowires: Size and Temperature Effects.* Phys. Rev. Lett. **99**, 226604 (2007).
- [22] **G. Mihajlović, J. E. Pearson, M. A. Garcia, S. D. Bader, A. Hoffmann.** *Negative Nonlocal Resistance in Mesoscopic Gold Hall Bars: Absence of the Giant Spin Hall Effect.* Phys. Rev. Lett. **103**, 166601 (2009).
- [23] **O. Mosendz, J. E. Pearson, F. Y. Fradin, G. E. W. Bauer, S. D. Bader, A. Hoffmann.** *Quantifying Spin Hall Angles from Spin Pumping: Experiments and Theory.* Phys. Rev. Lett. **104**, 046601 (2010).
- [24] **T. Valet, A. Fert.** *Theory of the perpendicular magnetoresistance in magnetic multilayers.* Phys. Rev. B **48**, 7099 (1993).
- [25] **M. Johnson, R. H. Silsbee.** *Interfacial charge-spin coupling: Injection and detection of spin magnetization in metals.* Phys. Rev. Lett. **55**, 1790 (1985).
- [26] **M. Johnson, R. H. Silsbee.** *Coupling of electronic charge and spin at a ferromagnetic-paramagnetic metal interface.* Phys. Rev. B **37**, 5312 (1988).
- [27] **F. J. Jedema, A. T. Filip, B. J. van Wees.** *Electrical spin injection and accumulation at room temperature in an all-metal mesoscopic spin valve.* Nature **410**, 345 (2001).
- [28] **F. J. Jedema, M. S. Nijboer, A. T. Filip, B. J. van Wees.** *Spin injection and spin accumulation in all-metal mesoscopic spin valves.* Phys. Rev. B **67**, 085319 (2003).

- [29] **S. O. Valenzuela, M. Tinkham.** *Spin-polarized tunneling in room-temperature mesoscopic spin valves.* Appl. Phys. Lett. **85**, 5914 (2004).
- [30] **F. J. Jedema, H. B. Heersche, A. T. Filip, J. J. A. Baselmans, B. J. van Wees.** *Electrical detection of spin precession in a metallic mesoscopic spin valve.* Nature **416**, 713 (2002).
- [31] **S. O. Valenzuela, M Tinkham.** *Direct electronic measurement of the spin Hall effect.* Nature **442**, 176 (2006).
- [32] **R. Karplus, J. M. Luttinger.** *Hall Effect in Ferromagnetics.* Phys. Rev. **95**, 1154 (1954).
- [33] **J. Smit.** *The spontaneous Hall effect in ferromagnetics - I.* Physica **21**, 877 (1955).
- [34] **J. Smit.** *The spontaneous Hall effect in ferromagnetics - II.* Physica **24**, 39 (1958).
- [35] **J. M. Luttinger, W. Kohn.** *Quantum Theory of Electrical Transport Phenomena. II.* Phys. Rev. **109**, 1892 (1958).
- [36] **J. M. Luttinger.** *Theory of the Hall Effect in Ferromagnetic Substances.* Phys. Rev. **112**, 739 (1958).
- [37] **G. Sundaram, Q. Niu.** *Wave-packet dynamics in slowly perturbed crystals: Gradient corrections and Berry-phase effects.* Phys. Rev. B **59**, 14915 (1999).
- [38] **D. Culcer, Y. Yao, Q. Niu.** *Coherent wave-packet evolution in coupled bands.* Phys. Rev. B **72**, 085 110 (2005).
- [39] **L. Berger.** *Side-jump mechanism for the Hall effect of ferromagnets.* Phys. Rev. B **2**, 4559 (1970).
- [40] **L. Berger.** *Application of the Side-Jump Model to the Hall Effect and Nernst Effect in Ferromagnets.* Phys. Rev. B **5**, 1862 (1972).
- [41] **A. Crèpieux, P. Bruno.** *Theory of the anomalous Hall effect from the Kubo formula and the Dirac equation.* Phys. Rev. B **64**, 014 416 (2001).
- [42] **N. A. Sinitsyn, Q. Niu, A. H. MacDonald.** *Coordinate shift in the semiclassical Boltzmann equation and the anomalous Hall effect.* Phys. Rev. B **73**, 075 318 (2006).
- [43] **N. A. Sinitsyn, A. H. MacDonald, T. Jungwirth, V. K. Dugaev, J. Sinova.** *Anomalous Hall effect in a two-dimensional Dirac band: The link between the Kubo-Streda formula and the semiclassical Boltzmann equation approach.* Phys. Rev. B **75**, 045 315 (2007).
- [44] **N. A. Sinitsyn.** *Semiclassical theories of the anomalous Hall effect.* J. Phys.: Condens. Matter **20**, 023 201 (2008).
- [45] **W. Kohn, J. M. Luttinger.** *Quantum Theory of Electrical Transport Phenomena.* Phys. Rev. **108**, 590 (1957).

- [46] **M. V. Berry.** *Quantal phase factors accompanying adiabatic changes.* Proc. R. Soc. Lond. A. **392**, 45 (1984).
- [47] **R. Shindou, K. I. Imura.** *Noncommutative geometry and non-Abelian Berry phase in the wave-packet dynamics of Bloch electrons.* Nuclear Phys. B **720**, 399 (2005).
- [48] **M. Born, R. Oppenheimer.** *Zur Quantentheorie der Moleküle.* Annalen der Physik **84**, 457 (1927).
- [49] **P. Hohenberg, W. Kohn.** *Inhomogeneous Electron Gas.* Phys. Rev. **136**, B864 (1964).
- [50] **W. Kohn, L. J. Sham.** *Self-Consistent Equations Including Exchange and Correlation Effects.* Phys. Rev. **140**, A1133 (1965).
- [51] **J. Zabloudil, R. Hammerling, L. Szunyogh, P. Weinberger.** *Electron Scattering in Solid Matter.* Springer Verlag Berlin (2005).
- [52] **B. A. Lippmann, J. Schwinger.** *Variational Principles for Scattering Processes. I.* Phys. Rev. **79**, 469 (1950).
- [53] **H. Triebel.** *Höhere Analysis.* Berlin, Deutscher Verlag der Wissenschaften (1972).
- [54] **J. Korringa.** *On the calculation of the energy of a Bloch wave in a metal.* Physica **13**, 392 (1947).
- [55] **W. Kohn, N. Rostoker.** *Solution of the Schrödinger Equation in Periodic Lattices with an Application to Metallic Lithium.* Phys. Rev. **94**, 1111 (1954).
- [56] **L. Szunyogh, B. Újfalussy, P. Weinberger.** *Magnetic anisotropy of iron multilayers on Au(001): First-principles calculations in terms of the fully relativistic spin-polarized screened KKR method.* Phys. Rev. B **51**, 9552 (1995).
- [57] **R. Zeller, P. Dederichs, B. Ujfalussy, L. Szunyogh, P. Weinberger.** *Theory and convergence properties of the screened Korringa-Kohn-Rostoker method.* Phys. Rev. B **52**, 8807 (1995).
- [58] **N. Papanikolaou, R. Zeller, P. H. Dederichs.** *Conceptual improvements of the KKR method.* J. Phys.: Condens. Matter **14**, 2799 (2002).
- [59] **S. Takada.** *Relativistic Formulation of the Green's Function Method in Periodic Lattices.* Prog. Theor. Phys. **36**, 224 (1966).
- [60] **Y. Onodera, M. Okazaki.** *Relativistic Theory for Energy-Band Calculation.* J. Phys. Soc. Jpn. **21**, 1273 (1966).
- [61] **R. Feder, F. Rosicky, B. Ackermann.** *Relativistic multiple scattering theory of electrons by ferromagnets.* Z. Phys. B: Condens. Matter **52**, 31 (1983).
- [62] **P. Strange, J. B. Staunton, B. L. Gyorffy.** *Relativistic spin-polarised scattering theory-solution of the single-site problem.* J. Phys. C **17**, 3355 (1984).

- [63] **G. Schadler, P. Weinberger, A. M. Boring, R. C. Albers.** *Relativistic spin-polarized electronic structure of Ce and Pu.* Phys. Rev. B **34**, 713 (1986).
- [64] **P. Strange, H. Ebert, J. B. Staunton, B. L. Gyorffy.** *A relativistic spin-polarised multiple-scattering theory, with applications to the calculation of the electronic structure of condensed matter.* J. Phys.: Condens. Matter **1**, 2959 (1989).
- [65] **S. A. Ostanin, V. P. Shirokovskii.** *A simplified method of ab initio calculation of electron states in relativistic magnetics. I. Ferromagnets.* J. Phys.: Condens. Matter **2**, 7585 (1990).
- [66] **P. Strange.** *Relativistic Quantum Mechanics.* Cambridge University Press, Cambridge, England (1998).
- [67] **H. Ebert.** *Electronic Structure and Physical Properties of Solids, Lecture Notes in Physics, "Fully relativistic band structure calculations for magnetic solids - Formalism and Application".* Springer, Berlin, vol. 535, p. 191 (2000).
- [68] **P. Zahn.** *Screened Korringa-Kohn-Rostoker-Methode für Vielfachschichten.* Doktorarbeit Technische Universität Dresden (1998).
- [69] **J. Binder.** *Giant Magnetoresistance - eine ab-initio Beschreibung.* Doktorarbeit Technische Universität Dresden (2000).
- [70] **M. Czerner.** *Beiträge zur Theorie des Elektronentransports in Systemen mit nichtkollinearer magnetischer Ordnung.* Doktorarbeit Martin-Luther-Universität Halle-Wittenberg (2009).
- [71] **I. Mertig, E. Mrosan, P. Ziesche.** *Multiple Scattering Theory of Point Defects in Metals: Electronic Properties.* Teubner-Verlag, Leipzig (1987).
- [72] **G. Lehmann, M. Taut.** Phys. Stat. Sol. (b) **54**, 469 (1972).
- [73] **P. Zahn.** Diplomarbeit TU Dresden (1994).
- [74] **V. P. Shirokovskii, N. A. Shilkova, N. A. Trubitsina.** *Calculation of electron velocity in crystal ab-initio, Results of computation by Green's function method for Vanadium.* Phys. Stat. Sol. (b) **133**, 593 (1986).
- [75] **N. A. Shilkova, V. P. Shirokovskii.** *Calculation of electron velocity in crystal ab initio, Role of relativistic effects.* Phys. Stat. Sol. (b) **149**, 571 (1988).
- [76] **H. A. Kramer.** Proc. Acad. Sci. Amsterdam **33**, 959 (1930).
- [77] **J. Fabian, S. Das Sarma.** J. Vac. Sci. Technol. B **17**, 1708 (1999).
- [78] **J. Fabian, A. Matos-Abiague, C. Ertler, P. Stano, I. Zutic.** *Semiconductor Spintronics.* Acta Phys. Slov. **57**, 565 (2007).
- [79] **R. J. Elliott.** *Theory of the Effect of Spin-Orbit Coupling on Magnetic Resonance in Some Semiconductors.* Phys. Rev. **96**, 266 (1954).
- [80] **Y. Yafet.** *Solid State Physics.* Academic Press, New York (1963).

- [81] **G. L. Bir, A. G. Aronov, G. E. Pikus.** *Spin relaxation of electrons scattered by holes.* Zh. Eksp. Teor. Fiz. **69**, 1382 (1975).
- [82] **A. Messiah.** *Quantenmechanik* Band 2. Berlin; New York: de Gruyter (1991).
- [83] **E. Merzbacher.** *Quantum Mechanics.* John Wiley & Sons Inc., New York (1998).
- [84] **S. Takahashi, S. Maekawa.** *Spin injection and transport in magnetic nanostructures.* Physica C **437-438**, 309 – (2006).
- [85] **I. Mertig, R. Zeller, P. H. Dederichs.** *Ab initio calculations of residual resistivities for dilute Ni alloys.* Phys. Rev. B **47**, 16 178 (1993).
- [86] **I. Mertig.** *Transport properties of dilute alloys.* Rep. Prog. Phys. **62**, 237 (1999).
- [87] **W. H. Butler.** *Theory of electronic transport in random alloys: Korringa-Kohn-Rostoker coherent-potential approximation.* Phys. Rev. B **31**, 3260 (1985).
- [88] **P. Streda.** *Theory of quantised Hall conductivity in two dimensions.* J. Phys. C **15**, L717 (1982).
- [89] **S. Lowitzer.** *private communication.*
- [90] **P. T. Coleridge.** *Impurity scattering in copper.* J. Phys. F **2**, 1016 (1972).
- [91] **J. C. Swihart, W. H. Butler, G. M. Stocks, D. M. Nicholson, R. C. Ward.** *First-Principles Calculation of the Residual Electrical Resistivity of Random Alloys.* Phys. Rev. Lett. **57**, 1181 (1986).
- [92] **P. Zahn, J. Binder, I. Mertig.** *Impurity scattering and quantum confinement in giant magnetoresistive systems.* Phys. Rev. B **68**, 100 403 (2003).
- [93] **J Bass.** *Table 1: host metal Ag - Fe.* SpringerMaterials - The Landolt-Börnstein Database (<http://www.springermaterials.com>).
- [94] **P. Zahn.** online. URL <http://www.phy.tu-dresden.de/~fermisur/>.
- [95] **P. Zahn, J. Binder, I. Mertig, R. Zeller, P. H. Dederichs.** Phys. Rev. Lett. **80**, 4309 (1998).

Publications

- [E1] **M. Gradhand, O. Breitenstein.** *Preparation of nonconducting infrared-absorbing thin films.* Rev. Sci. Instrum. **76** (5), 053 702 (2005).
- [E2] **C. Heiliger, M. Gradhand, P. Zahn, I. Mertig.** *Tunneling magnetoresistance on the sub-nanometer scale.* Phys. Rev. Lett. **99**, 066 804 (2007).
- [E3] **M. Gradhand, C. Heiliger, P. Zahn, I. Mertig.** *Tunneling magnetoresistance with amorphous electrodes.* Phys. Rev. B **77** (13), 134 403 (2008).
- [E4] **D. V. Fedorov, P. Zahn, M. Gradhand, I. Mertig.** *First-principles calculations of spin relaxation times of conduction electrons in Cu with nonmagnetic impurities.* Phys. Rev. B **77**, 092 406 (2008). *Erratum:* Phys. Rev. B **79** 059901(E) (2009).
- [E5] **M. Gradhand, M. Czerner, D. V. Fedorov, P. Zahn, B. Yu. Yavorsky, L. Szunyogh, I. Mertig.** *Spin polarization on Fermi surfaces of metals by the KKR method.* Phys. Rev. B **80**, 224 413 (2009).
- [E6] **M. Gradhand, D. V. Fedorov, P. Zahn, I. Mertig.** *Fully relativistic ab initio treatment of spin-flip scattering caused by impurities.* Phys. Rev. B **81**, 020 403(R) (2010).
- [E7] **M. Gradhand, D. V. Fedorov, P. Zahn, I. Mertig.** *Extrinsic Spin Hall Effect from First Principles.* Phys. Rev. Lett. **104**, 186 403 (2010).
- [E8] **M. Gradhand, D. V. Fedorov, P. Zahn, I. Mertig.** *Spin Hall angle versus spin diffusion length: Tailored by impurities.* Phys. Rev. B **81**, 245 109 (2010).

Acknowledgment

At that point I want to thank all persons who supported me to finish this thesis.

First of all, I thank my supervisor Prof. I. Mertig who provided me the topic and supported me during my studies. She always believed in me and gave me all opportunities to become a scientist. Especially the attendance of conferences and workshops broadened my knowledge of the scientific world.

The next is Dr. D.V. Fedorov who had always time for me and answered many difficult and also stupid questions. He always stopped me to be inaccurate and asked nasty questions to improve what I did. From my point of view our cooperation was perfect.

The other persons who were always willingly to answer questions concerning the KKR code were Dr. habil. P. Zahn, Dr. M. Czerner, and Dr. B.Yu.Yavorsky. Without their help and detail knowledge of the KKR code I would never be able to understand what the code was doing under certain conditions.

Special thanks I give to our computer support group (S. Achilles, C. Matyssek, M. Czerner, and M. Däne), who solved all problems immediately and allowed me to perform all calculations which were needed.

My officemates M. Fechner and Ch. Langheinrich had not an easy live with me but at least they survived. Our room was small, very hot during the summer and we learned to live without oxygen. I am thankful that they never tried to clean up my desk so I could always find important notes under the mountains of paper.

At the end, I thank my family who supported me during the full time of my PhD and accepted that it was sometimes difficult to stop thinking at home.

Eidesstattliche Erklärung

Hiermit erkläre ich gemäß §5 Abs. 2b der Promotionsordnung der Naturwissenschaftlich Fakultät II-Chemie und Physik der Martin-Luther-Universität Halle-Wittenberg vom 3.2.2004, daß ich die vorliegende Arbeit

The Extrinsic Spin Hall Effect

selbständig und ohne fremde Hilfe verfaßt, andere als die von mir angegebenen Quellen und Hilfsmittel nicht benutzt und die den benutzten Werken wörtlich oder inhaltlich entnommenen Stellen als solche kenntlich gemacht habe. Ich erkläre, die Angaben wahrheitsgemäß gemacht und keine wissenschaftliche Arbeit an einer anderen wissenschaftlichen Einrichtung zur Erlangung eines akademischen Grades eingereicht zu haben.

Halle, den 25. Juni 2010

Martin Gradhand

Curriculum vitae

Personal data:

name Martin Gradhand
 address Triftstraße 3, 06114 Halle (Saale)
 date of birth and place 14. April 1982, Schiepzig (Germany)

Education:

1988 - 1992 Primary school: Grundschule Ernst-Thälmann Salzmünde
 1992 - 2000 Grammar school: Latina August Herrmann Francke
 2000 - 2001 civilian service in a hospital
 2001 - 2006 Studies of physics at Martin Luther University Halle-Wittenberg
 completed as graduate physicist (degree: Diplom-Physiker)
 Diploma title:
 "Tunnelmagnetwiderstand (TMR) mit amorphen Elektroden"
 ("Tunneling magnetoresistance with amorphous electrodes")

Jan. 2007 -
 June 2010 PhD studentship at the Max Planck Institute
 of Microstructure Physics

Jan. 2007 -
 June 2010 Member of the International Max Planck Research School
 for Science and Technology of Nanostructures

Jan. 2008 -
 June 2008 childcare leave

Martin Gradhand